Experiments and First-Principle Investigation of Typical Three Cathode Active Materials for Na-ion Batteries

伊舎堂，雄二

Experiments and First-Principle Investigation of Typical Three Cathode Active Materials for Na-ion Batteries

Yuji Ishado

Interdisciplinary Graduate School of Engineering Sciences

Kyushu University

August 2020

Contents

Chapter 2

An Experimental and First-principle Investigation of the Ca-substitution Effect on P3-type Layered Na$_x$CoO$_2$ **42**

Chapter 3

Chapter 4

Chapter 5

Chapter 1

Introduction

1.1. Research Background

In recent years, climate change and the depletion of fossil fuels have become increasingly serious issues. The use of renewable energies, such as wind and solar power, is crucial for the realization of a sustainable society. However, the electricity generated by renewable energies tends to fluctuate, making it difficult to balance the energy supplies and demands. Large-scale energy storage systems that function as a buffer between the energy-supply side and energy-consumption side are essential technologies to address this issue. Such energy storage systems must possess high energy efficiency, high power density, long cycle life, easy maintenance, and excellent cost-effectiveness. Secondary (or rechargeable) batteries are a promising energy storage system because they potentially satisfy these requirements. Moreover, the battery modules can be flexibly located at different sites, which is also advantageous for a small-scale energy grid system.

Electric vehicles (EVs) are another critical technology to reduce fossil-fuel consumption and greenhouse gas emission. Although Li-ion batteries (LIBs) have generally been used as power sources of EVs, the high cost, inadequate energy density, and other factors

related to the battery properties have prevented the widespread adoption of EVs. Therefore, the development of secondary batteries with lower cost, higher energy density, safety, longer cycle life, and shorter charging time is indispensable to make EVs more competitive with conventional gasoline-fueled vehicles.

In addition to the applications above, secondary batteries are the key component for other emerging technologies such as smartphones and drones. Thus, the demand for secondary batteries will continue to grow, along with the importance of battery research.

1.2. Li-ion Batteries

1.2.1. Overview of Li-ion batteries

Various types of batteries, such as lead-acid, nickel-cadmium (Ni-Cd), nickel-metal-hydride (Ni-MH), and LIBs, have been developed and widely used. Figure 1-1 shows volumetric and gravimetric energy densities of different secondary batteries [1]. Note that PLiON denotes plastic LIBs. Li-metal batteries have not been commercialized yet due to safety issues while the other batteries in Fig. 1-1 have been put to practical use. The LIBs offer higher volumetric and gravimetric energy density than the other commercialized batteries. Additionally, the LIBs have good cycle performance without memory effects, unlike Ni-Cd and Ni-MH batteries. Due to these excellent features, the LIBs have been widely used for various applications.

Historically, many researchers have contributed to the development of LIBs. In 1976, Whittingham discovered the electrochemical lithium intercalation into TiS_2 and proposed a battery composed of a Li metal anode and TiS_2 cathode [2]. While this battery was not commercialized because the Li metal posed a safety hazard, the discovery led to research on the so-called "rocking chair"-type batteries [3, 4]. In 1980, Mizushima and Goodenough

2

demonstrated the electrochemical Li^+ extraction/insertion reaction in $LiCoO_2$ [5]. For the anode material, Yazami reported on the reversible electrochemical intercalation of Li^+ ions in graphite by using a solid electrolyte in 1983 [6]. In 1985, Yoshino proposed a battery consisting of a carbonaceous anode and $LiCoO_2$ cathode [7], and in 1991 Sony commercialized an LIB for the first time. In 2019, the Nobel Prize in Chemistry was given to Yoshino, Goodenough, and Whittingham for their development of the LIBs.
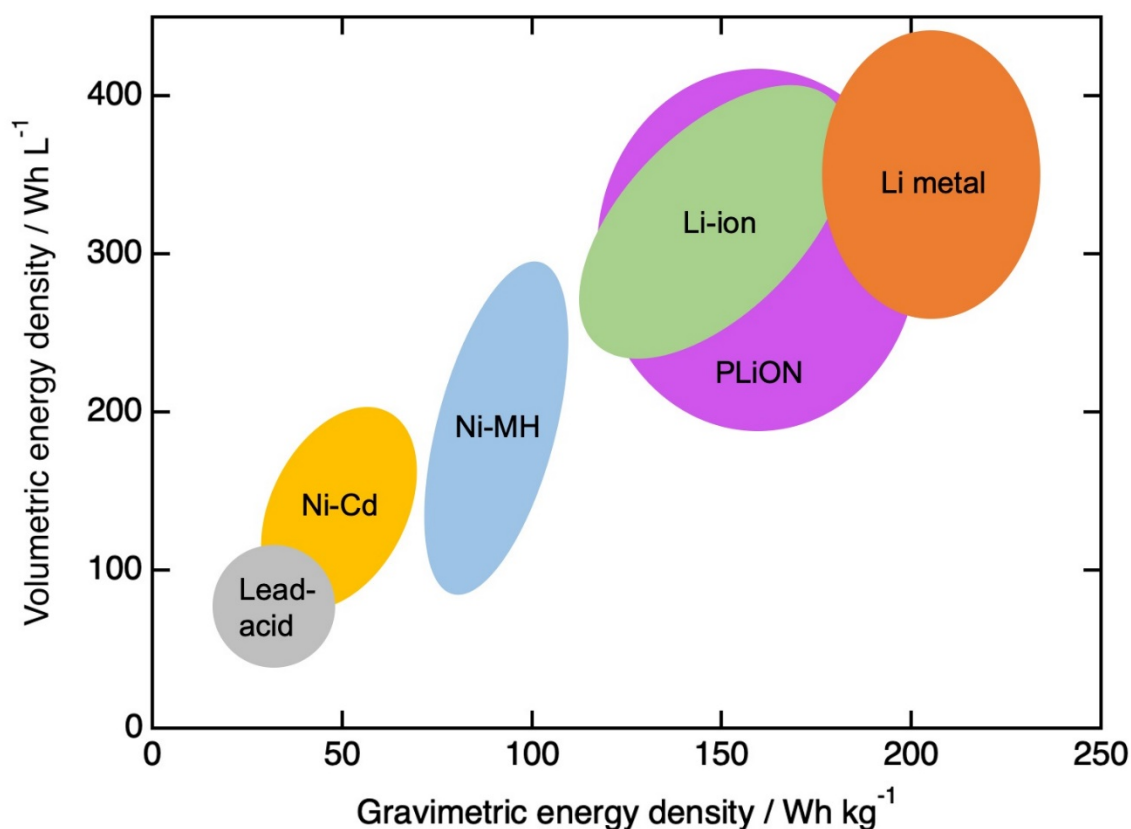
Figure 1-1 Volumetric and gravimetric energy densities of different secondary batteries. With the exception of the Li metal batteries, all these batteries have been commercialized. PLiON denotes plastic LIBs [1].
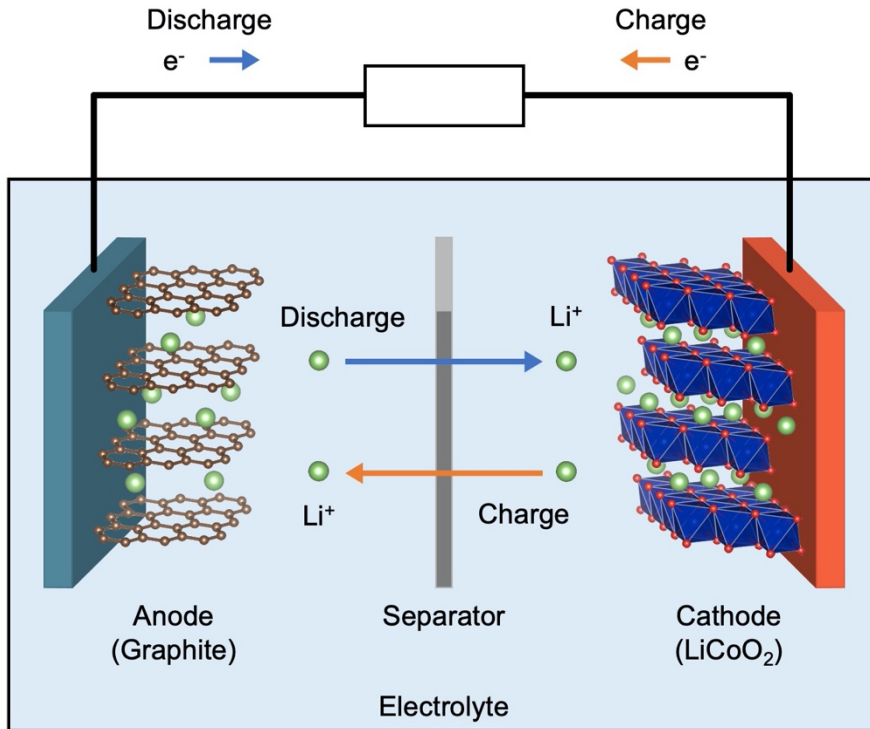
Figure 1-2 Schematic illustration of a typical LIB.

Figure 1-2 shows a schematic illustration of a typical LIB. It consists of three essential components: cathode, anode, and electrolyte. A separator is also used in order to prevent an internal short circuit.

During the charge and discharge reaction, Li$^+$ ions are extracted from one electrode, passed through an electrolyte and separator, and inserted into the other electrode. At the same time, the electrons flow in the external circuit and move between the two electrodes. The redox reactions in the typical LIBs are shown below:

Cathode: $LiCo^{3+}O_2 \rightleftarrows Li_{1-x}Co^{(3+x)+}O_2 + x\ Li^+ + x\ e^-$ (1-1)

Anode: $C_6 + x\ Li^+ + x\ e^- \rightleftarrows Li_xC_6$ (1-2)

Total: $LiCo^{3+}O_2 + C_6 \rightleftarrows Li_{1-x}Co^{(3+x)+}O_2 + Li_xC_6$ (1-3)
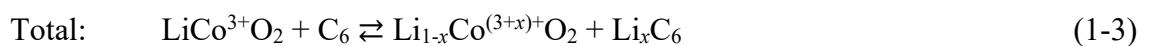
In the above case, the active materials retain their original host structures during the insertion/extraction of Li$^+$. Such reactions are referred to as "insertion" reactions. On the other hand, some active materials exhibit drastic structural transformation during the charge/discharge reaction. These reactions are called "conversion" reactions [8-10]. Another well-known reaction type is the "alloying" reaction, in which Li forms an alloy with the active material. Active materials that undergo an alloying reaction are generally used for the anode, since the redox voltage is low. Although the conversion and alloying reactions offer large capacities, their reversibility and cycle performance are worse than the insertion reaction due to the drastic structural change. Thus, the insertion-type materials are used for most of the commercialized LIBs. The theoretical capacity of active material is given as:

$$Capacity = \frac{n \times F}{3600 \times M} \tag{1-4}$$

where n is the reaction electron number, F is the Faraday constant, and M is the molecular weight of the active material. The voltage of a battery is determined by the following equation:

$$V = -\frac{\mu_c - \mu_a}{nF} \tag{1-5}$$

where μ_c and μ_a represent the chemical potentials of Li$^+$ in the cathode and anode, respectively.

1.2.2. Components of Li-ion batteries

The LIBs are composed of various components, as shown in Table 1-1. In this section, typical materials for each component are briefly presented.

Table 1-1 Components of LIBs

Components	Typical materials
Cathode	$LiMO_2$, $LiMn_2O_4$, $LiFePO_4$
Anode	Graphite, hard carbon, $Li_4Ti_5O_{12}$, Sn
Electrolyte solvent	EC, DMC, DEC, PC
Electrolyte salt	$LiPF_6$, $LiBF_4$, $LiClO_4$
Separator	Microporous polyolefin membrane
Binder	PVDF, PTFE
Cathode current collector	Al foil
Anode current collector	Cu foil

1.2.2.1. Cathode active materials for Li-ion batteries

For the cathode active materials in LIBs, several features, such as high energy density, high electronic and ionic conductivity, excellent cycle performance, and acceptable cost, are required. Layered oxides such as $LiCoO_2$, spinel-type $LiMn_2O_4$, and olivine-type $LiFePO_4$ meet these requirements and have been widely used as cathode active materials for LIBs [5, 11, 12].

6

Layered oxides, $LiMO_2$ (M = Co, Mn, Ni, Al, and so on), are the most common cathode materials. $LiMO_2$ consists of sheets of edge-shared MO_6 octahedra, as shown in Fig. 1-3a. Li^+ ions diffuse two-dimensionally between the MO_2 layers. Although $LiCoO_2$ has been widely used, other layered oxides with lower Co content have been developed since Co is expensive. For example, the ternary systems such as $LiNi_{1-x-y}Mn_xCo_yO_2$ (NMC) and $LiNi_{1-x-y}Co_xAl_yO_2$ (NCA) have been commercialized [13, 14]. The layered oxides offer a voltage of 3.7–4.1 V vs. Li^+/Li^0 and capacity of $\sim$ 150 mAh g^{-1}.

Spinel-type $LiMn_2O_4$ is another type of oxide (Fig. 1-3b). Li^+ ions occupy the tetrahedral sites in $LiMn_2O_4$, while they occupy the octahedral sites in the layered $LiMO_2$. $LiMn_2O_4$ is less expensive than $LiCoO_2$ since $LiMn_2O_4$ does not contain Co. The average voltage and capacity of $LiMn_2O_4$ are approximately 4.0 V and 120 mAh g^{-1}, respectively [15].

Olivine-type $LiFePO_4$ is also a cheaper cathode material than $LiCoO_2$. Li^+ ions diffuse in the one-dimensional path along the *b*-axis in Fig. 1-3c. $LiFePO_4$ has a flat plateau at 3.4 V with a capacity of $\sim$ 160 mAh g^{-1}. Since $LiFePO_4$ has a low electronic conductivity, nano-particle synthesis and carbon coating are employed to improve the cathode property [16].

Other cathode materials such as $Fe_2(SO_4)_3$, $Li_3V_2(PO_4)_3$, $LiVPO_4F$, and perovskite-type FeF_3 have been studied [17-20], but have not yet been put to practical use.
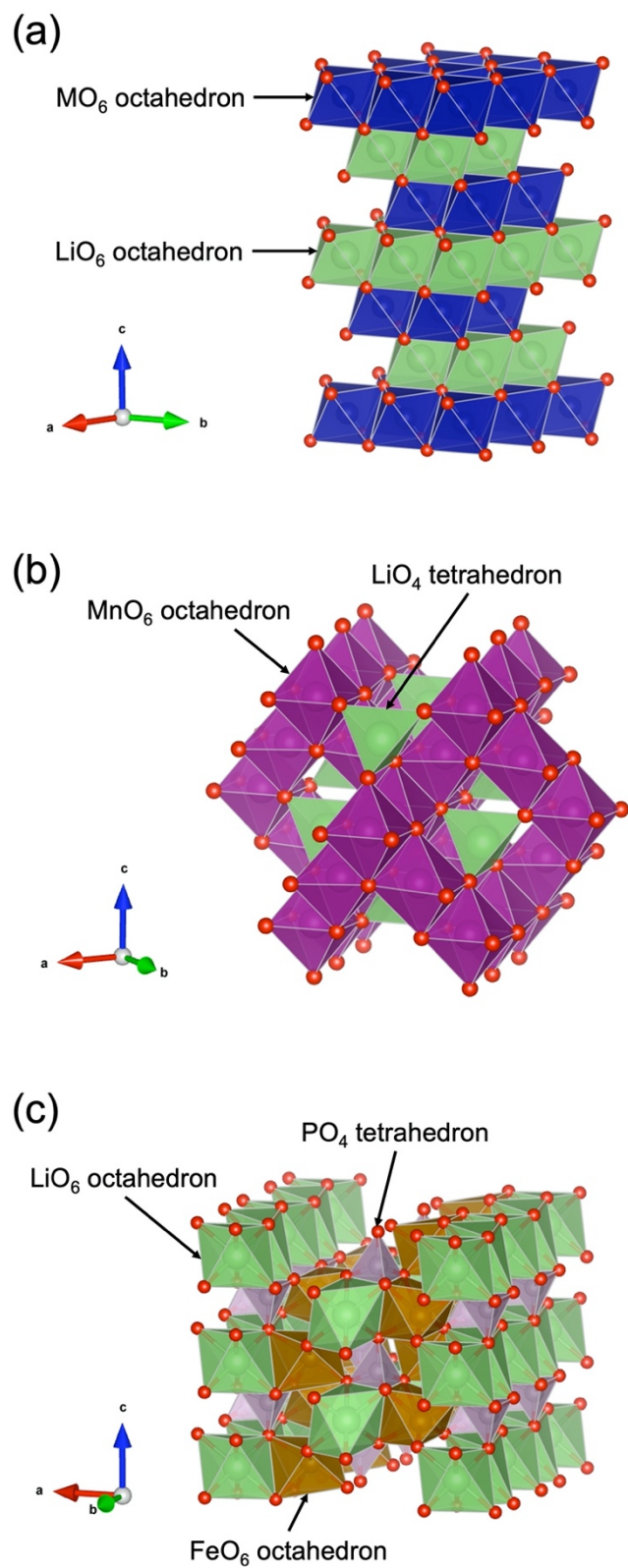
Figure 1-3 Crystal structures of **(a)** $LiMO_2$, **(b)** $LiMn_2O_4$, and **(c)** $LiFePO_4$. The structures are visualized by using VESTA [21].

1.2.2.2. Anode active materials for Li-ion batteries

Li metal cannot be used as an anode due to the dendrite formation during the charge/discharge process. The most widely used anode material is graphite, since Li^+ ions can be intercalated to the graphite without Li metal deposition [6, 22]. In addition, the graphite anodes offer a high energy density, since the redox potential is close to that of the Li metal (~ 0.1 V vs. Li^+/Li^0). While the low redox voltage is advantageous in terms of the energy density, it poses a risk of accidental Li-metal deposition caused by a high current or other factors. Hard carbon is also used as an anode material [23, 24], but it is not as common as graphite.

In addition to the carbonaceous anode, $Li_4Ti_5O_{12}$ has been commercialized as a safe anode material [25]. This material exhibits a voltage of 1.5 V vs. Li^+/Li^0. Although such a high voltage is unfavorable in terms of energy density, it can reduce the risk of accidental Li-metal deposition. Moreover, $Li_4Ti_5O_{12}$ has an excellent cycle performance due to the negligible volume change during the charge/discharge reaction [26].

Alloys such as Li-Sn and Li-Si systems have been extensively studied [27, 28], and Sony commercialized the Sn-based anode in 2005 [29].

1.2.2.3. Electrolytes

In conventional LIBs, organic electrolytes are generally used. The typical solvents for the electrolytes are ethylene carbonate (EC), dimethyl carbonate (DMC), diethyl carbonate (DEC), and propylene carbonate (PC). The binary combinations of these solvents are frequently used. Moreover, additives such as fluoroethylene carbonate (FEC) and vinylene carbonate (VC) are occasionally used to improve battery performance. $LiPF_6$ has been extensively adopted as the salt of the electrolyte, and $LiBF_4$ and $LiClO_4$ are occasionally used as additives. Electrolytes at

a concentration of 1 M (= mol L^{-1}) are widely used, since this concentration generally yields the highest conductivity.

Electrolytes have a so-called "potential window," which is bounded by the upper and lower limits of the applied potentials. Figure 1-4 shows a schematic energy diagram of an electrolyte [30]. If the cathodic potential is above the potential window, the electrolyte is oxidized. Similarly, if the anodic potential is below the potential window, the electrolyte is reduced. Therefore, the redox potential of the cathode and anode should be within the potential window, and the obtainable voltage is limited up to the range of the potential window. However, some active materials that have redox potentials outside the potential window can be utilized in the electrolytes. This is due to the formation of a solid electrolyte interphase (or interface), which is usually abbreviated as SEI [22, 31]. The SEI is a thin passivation layer formed on the surface of the active materials and provides kinetic stability to the electrolytes.
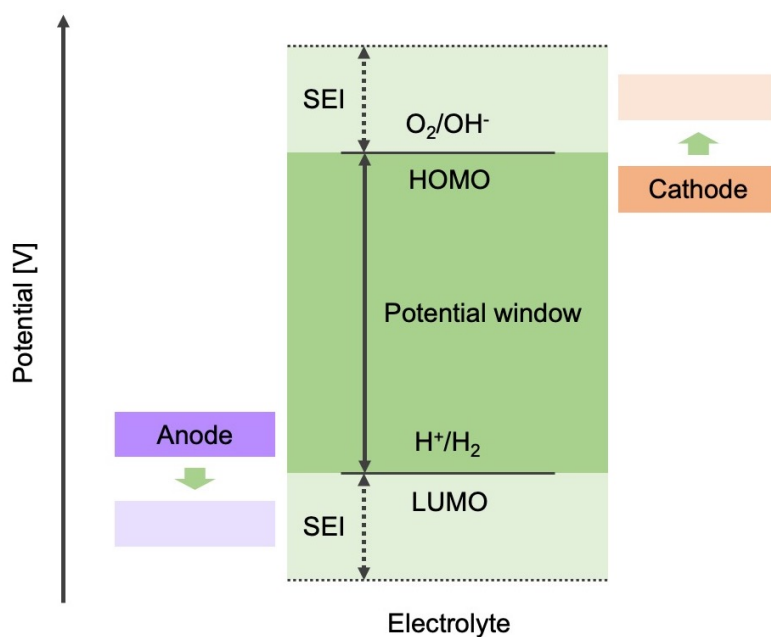
Figure 1-4 Schematic open-circuit energy diagram of the electrolyte [30].

1.2.2.4. Other components

In addition to the essential components discussed above, other components are also necessary for practical use. Separators are a critical component to prevent an internal short circuit. Practically, the separators are impregnated with the electrolyte and inserted between the cathode and anode. For safety reasons, it is desirable for the separators to have a shutdown function: when the temperature inside the battery becomes too high for any reason, the shutdown function blocks the movement of lithium ions and stops the operation of the battery by closing the micropores in the separator.

Since the active materials are in powder form, they are mixed with binders such as polyvinylidene fluoride (PVDF) and polytetrafluoroethylene (PTFE). Moreover, conductive carbon is frequently mixed with the active materials in order to form electron conductive paths throughout the electrodes. Commercially, the slurry is prepared by mixing the active materials, the conductive carbon, and the binder in a solvent, and then the slurry is cast on the current collector. Al foil is used for the cathode current collector. For the anode current collector, Cu foil is used, since Al forms an alloy with Li at the low potential.

1.2.3. Challenges for Li-ion batteries

Although the LIBs offer excellent features for various applications, such as portable electronic devices, there are still many challenges which should be addressed for applications such as large-scale energy storage systems and EVs:

(1) High cost and limited supply of Li

Before they can be widely applied to large-scale energy storage systems and EVs, the price of the LIBs must be reduced. Since Co is also expensive, the development of Co-free materials is indispensable. Recycling of the LIBs is also an important technology. Ultimately, a shift from LIBs to other, cheaper energy storage systems, such as Na- and K-ion batteries, is desired.

(2) Insufficient energy density

Larger energy densities are required for many applications. Therefore, the further development of cathode and anode materials is necessary. In order to utilize high voltage cathode materials and Li metal anodes, chemically stable and mechanically robust electrolytes such as solid-state electrolytes must be used.

(3) Safety

Since battery fires and explosion incidents are occasionally reported, the development of safer batteries such as all-solid-state batteries or aqueous batteries is needed.

(4) Rate capability

Fast charging is a desirable feature for EVs. Thus, cathode/anode active materials and electrolytes with superior ionic conductivities are needed. It is also important that the cathode and anode materials have good electronic conductivity.

(5) Cycle life

Long-term cycle life is vital for many applications, since the replacement of the batteries can be expensive and time-consuming, especially in large-scale energy storage systems and EVs.

1.3. Na-ion Batteries

1.3.1. Overview of Na-ion batteries

The growing demand for LIBs poses a risk of future depletion of the natural resources of lithium. The exhaustion of lithium resources could lead to limited availability and a severe increase in the price of the LIBs. As one of the promising alternatives to LIBs, Na-ion batteries (NIBs) have attracted research interest due to the abundance and low cost of sodium resources, as shown in Table 1-2. Moreover, a large number of sodium compounds are also one of the attractions of NIBs. However, Na has a higher standard electrode potential by 0.3 V than Li. Thus, the obtainable voltage of NIBs is generally lower than that of LIBs. Moreover, the ionic volume and the atomic mass of Na ions are 2.4 times and 3 times greater than those of Li ions. For these reasons, the NIBs generally exhibit lower energy densities than LIBs.

Despite these drawbacks, the NIBs are still an attractive option for stationary large-scale energy storage, because the energy-density requirement is less strict, and the cost-

effectiveness is a priority. Although NIBs are becoming commercially available [32], further improvements will be needed before they can be widely used as a substitute for conventional LIBs. The components of the NIBs are fundamentally the same as those of LIBs except that the working ion is not the Li ion but the Na ion.

Table 1-2 Comparison of the properties of Li and Na.

	Li	Na
Elemental abundance in the Earth's crust / ppm [33]	20	23,550
Price / $ kg^{-1}	17.0	0.15
Standard electric potential / V vs. SHE	-3.045	-2.714
Ionic volume / Å^3	1.84	4.45
Atomic mass / g mol^{-1}	6.9	23

1.3.2. Cathode materials for Na-ion batteries

In order to achieve practical NIBs, the development of cathode materials is crucial, and thus various compounds have been extensively studied as cathode materials for NIBs. In this section, some cathode materials are introduced with a focus on the materials studied in this thesis.

1.3.2.1. Layered transition metal oxides

The sodium layered transition metal oxides, Na_xMO_2 (M = Ti, V, Cr, Mn, Fe, Co, and Ni), have attracted research interest due to their relatively high energy densities, facile synthesis, and ease-of-handling [34-41]. Na_xMO_2 can be categorized into several groups depending on

the manner of oxygen atom stacking. Figure 1-5 illustrates the major structural groups of the layered oxide. A, B, and C in the figure denote the relative positions of the oxygen atoms. The nomenclature proposed by Delmas *et al.* [42] has been widely used to represent the structural types. In this nomenclature, the shape of the Na site and the periodicity of the stacking sequence are represented. For example, O3 means the Na ions occupy "octahedral" (O) sites, and the layered oxide consists of "three" MO_2 layers (AB CA BC). In the P2-type structure, the Na ions are located in "prismatic" (P) sites, and the layered oxides are composed of "two" MO_2 layers (AB BA). Note that the layered $LiCoO_2$ and other Li-based analogs generally have the O3-type structure.

As shown in Fig. 1-5, the O1, O3, and P3 can transform from one to another by the MO_2 slab gliding. This phase transition is observed during the charge/discharge reaction [34, 35]. Similarly, the O2 and P2 can transform into each other by the slab gliding. However, the phase transition between the O2-P2 group and O1-O3-P3 group requires breaking of the M-O bonds, since the orientations of the MO_6 octahedra are alternating in the O2-P2 group, while those in the O1-O3-P3 group are the same. Consequently, the phase transitions, such as the P3-P2 transition, are not observed during the electrochemical reaction but rather occur at high temperature [43].

Na_xMO_2 can accommodate a variety of elements in the transition metal site. Due to the flexibility, the binary, ternary, and quaternary systems such as P2-$Na_xFe_{1/2}Mn_{1/2}O_2$, O3-$NaNi_{1/3}Mn_{1/3}Co_{1/3}O_2$, and O3-$NaMn_{1/4}Fe_{1/4}Co_{1/4}Ni_{1/4}O_2$ have been extensively investigated [44-50]. Although the layered oxides offer acceptable energy densities, the severe capacity fading during the cycles prevents the practical use of the materials [51]. The capacity fading mainly originates from the phase transition during the charge/discharge reaction [34, 35, 52, 53]. Thus, it is imperative that the phase transition be suppressed in order to put the layered oxides to practical use.
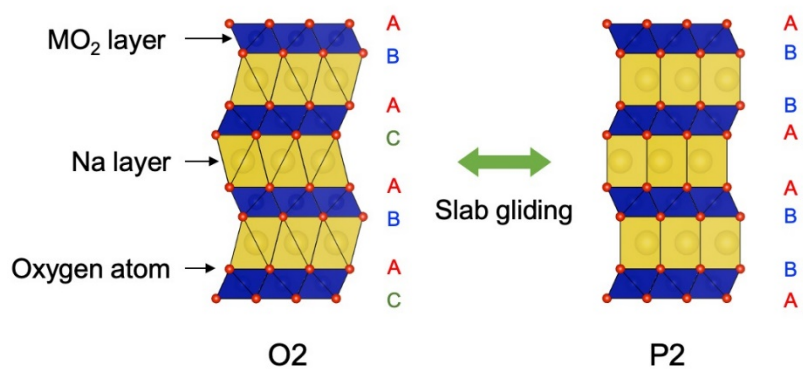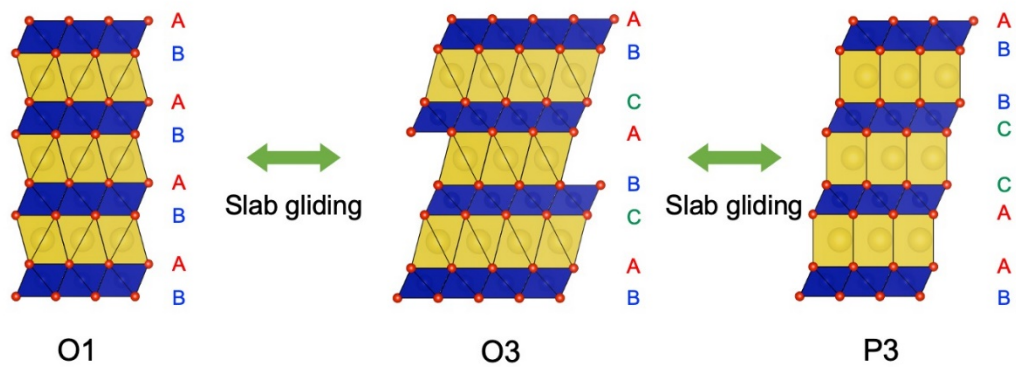
Figure 1-5 Schematic illustrations of O1-, O3-, P3-, O2- and P2-type structures. A, B, and C denote the relative oxygen positions.

1.3.2.2. NASICON-type structure

NASICON-type compounds are another promising cathode material for the NIBs. NASICON is an acronym for "NA-Super-Ionic-CONductor" and refers to a family of solid electrolytes with a composition of $Na_{1+x}Zr_2Si_xP_{3-x}O_{12}$ [54]. The NASICON-type compounds have a formula of $A_xM_2(XO_4)_3$. In the NASICON structure, MO_6 octahedra and XO_4 tetrahedra alternatively share all corners, constituting a stable framework. The NASICON-type compounds generally exhibit excellent Na^+ ion diffusivities because of the large void in the framework.

There is a similar structural type called "anti-NASICON," which also has the formula of $A_xM_2(XO_4)_3$ [17]. The anti-NASICON structure has features similar to those of the NASICON structure: the stable framework, the large interstitial space, and the excellent ionic diffusivity. Although these two structures are difficult to distinguish at a glance, they can be characterized by the orientations of lantern units, which consist of two MO_6 octahedra and three XO_4 tetrahedra, as shown in Fig. 1-6a. In the NASICON structure, the lantern units are arranged in the same orientation, while they are arranged in a zigzag pattern in the anti-NASICON structure. These two structures are often broadly referred to as "NASICON structures."

Among the various NASICON-type compounds, $Na_3V_2(PO_4)_3$ has been extensively studied because of its relatively high energy density, small overpotential, excellent rate capability, and good cycle performance [55-59]. Interestingly, its counterpart, $Li_3V_2(PO_4)_3$, has the anti-NASICON structure [18]. The structures of $Na_3V_2(PO_4)_3$ and $Li_3V_2(PO_4)_3$ are shown in Fig. 1-6bc.
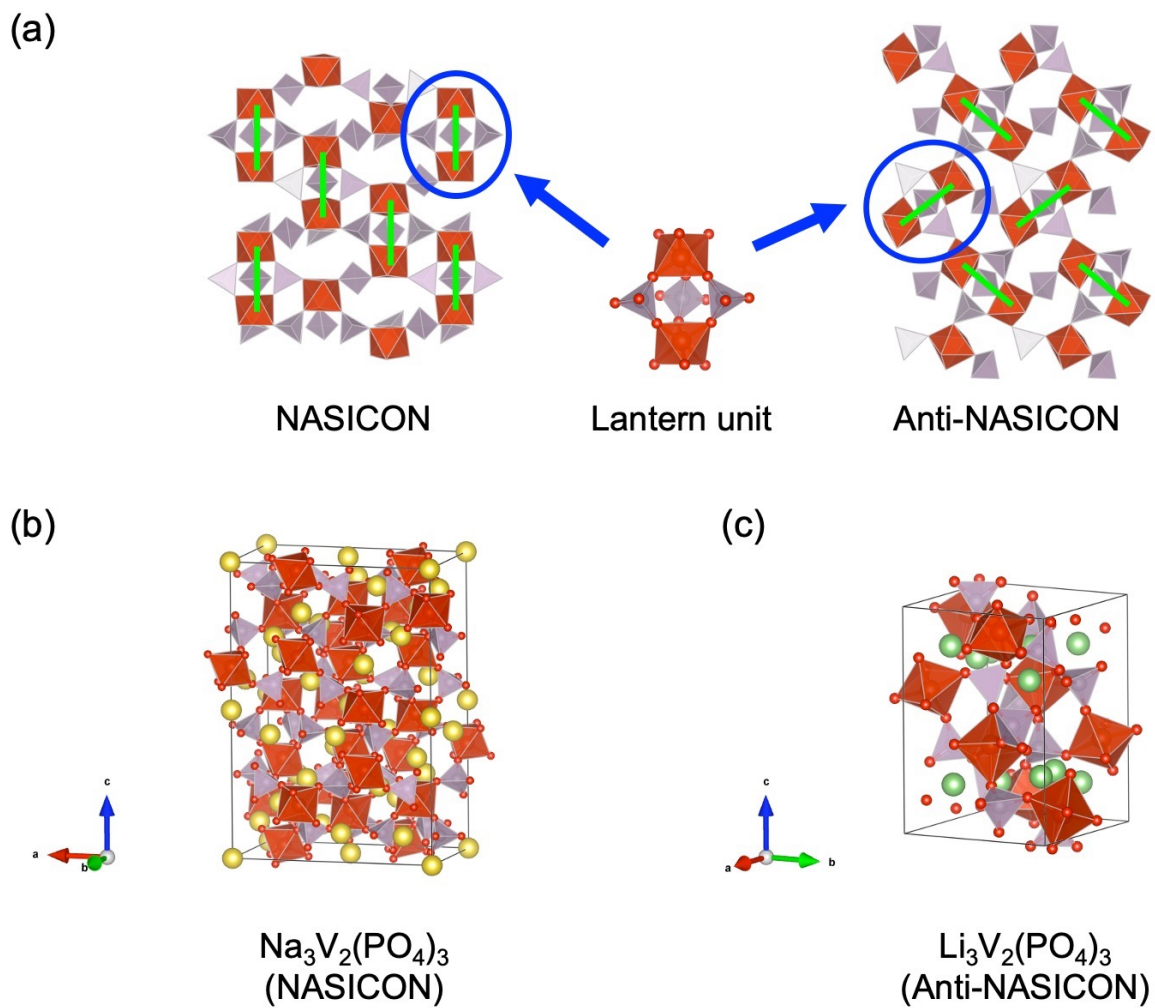
Figure 1-6 (a) NASICON and anti-NASICON frameworks. Green lines represent the orientations of the lantern units. Crystal structures of **(b)** NASICON-type $Na_3V_2(PO_4)_3$ and **(c)** anti-NASICON-type $Li_3V_2(PO_4)_3$ are also shown.

During the charge/discharge reaction, $Na_3V_2(PO_4)_3$ exhibits a plateau at 3.4 V vs. Na^+/Na^0, which corresponds to the V^{3+}/V^{4+} redox reaction. While $Na_3V_2(PO_4)_3$ offers acceptable performance as a cathode material, it is vital to increase the energy in order to develop competitive NIBs. The most common strategy to increase the energy density is the utilization of multi-redox reactions of vanadium ($V^{3+}/V^{4+}/V^{5+}$) by substituting vanadium with other electrochemically inactive elements [60-63]. Moreover, the substitution of divalent ions for vanadium can increase the initial amount of the Na^+, and thereby the capacity can be increased [64-66]. Multi-redox reactions of $Mn^{2+}/Mn^{3+}/Mn^{4+}$ can also be utilized in NASICON structures [67-69]. Figure 1-7 shows the relationship between the redox couples and the Na content per formula unit (x). The gray shaded region to the right of the pink line cannot be used as a cathode because the redox voltage is too low. The range of $0 \leq x \leq 1$ is also unusable, but the reason for this has not been elucidated, to the best of our knowledge.

Recently, Kawai et al. reported the electrochemical properties of $Na_3Cr_2(PO_4)_3$ [70]. Although a high voltage of Cr^{3+}/Cr^{4+} redox reaction (~ 4.5 V) was obtained, severe capacity fading was observed due to the instability of the material in the charged state. Although the Ti-substitution improved the stability of the material, a smaller capacity was obtained because of the decreased amount of Cr in the formula unit [71].
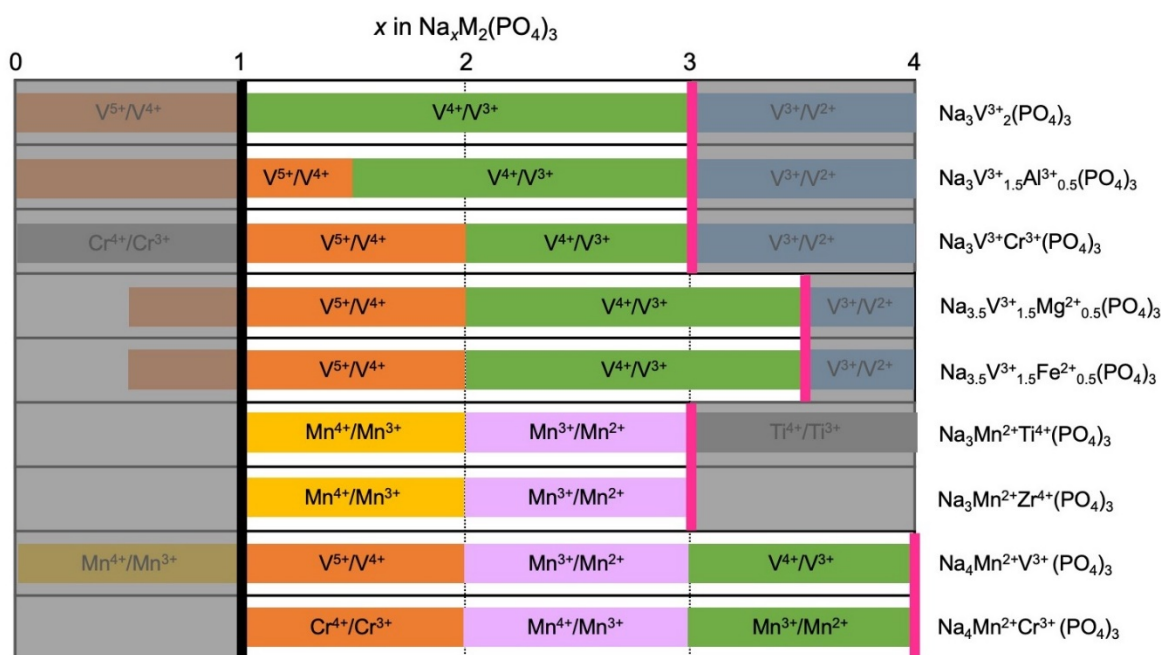
Figure 1-7 Schematic diagram of redox couples in NASICON-type cathode materials. Pink and black vertical lines represent Na compositions at the initial and charged state, respectively. The gray shaded region cannot be utilized as a cathode. All the materials were reported elsewhere: $Na_3V_2(PO_4)_3$ [55], $Na_3V_{2-x}Al_x(PO_4)_3$ [60, 61], $Na_3V_{2-x}Cr_x(PO_4)_3$ [62, 63], $Na_{3+x}V_{2-x}Mg_x(PO_4)_3$ [64], $Na_{3+x}V_{2-x}Fe_x(PO_4)_3$ [65], $Na_3MnTi(PO_4)_3$ [67], $Na_3MnZr(PO_4)_3$ [68], $Na_4VMn(PO_4)_3$ [66], $Na_4CrMn(PO_4)_3$ [69].

1.3.2.3. Perovskite-type Fluorides

Perovskite-type fluorides, Na_xMF_3 (M: transition metal), have drawn attention as cathode materials for NIBs since they have high voltage due to the high electronegativity of the fluorine [72-79]. Moreover, the perovskite-type fluorides have a large theoretical capacity, and the absence of the oxygen in their chemical formula can reduce the ignition risk of the battery. Iron- or manganese-based perovskite-type fluorides are especially suitable candidates because

of the abundance and low cost of their chemical elements. However, fluorides are generally

low electronic conductors. Thus, nano-particle preparation, well-dispersed carbon mixing, and

other techniques are needed to improve their cathode properties.
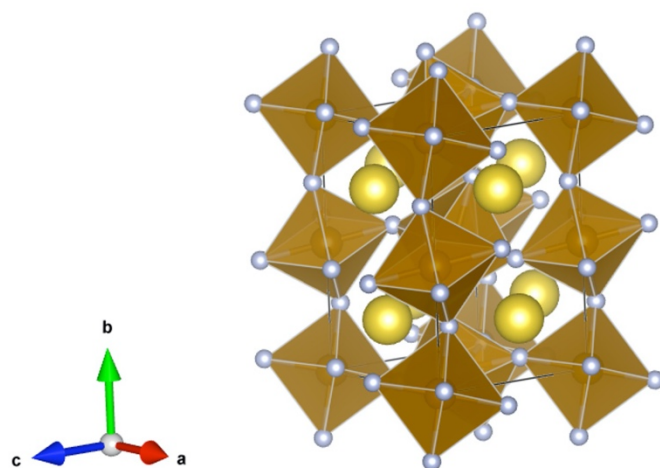
Figure 1-8 Crystal structure of perovskite-type $NaMF_3$

1.3.2.4. Other cathode materials

In addition to the cathode materials above, other materials have also been investigated. For

example, fluorophosphates such as $Na_3V_2(PO_4)_2F_3$ and $NaVPO_4F$ show attractive

electrochemical performance [80-82]. Barpanda *et al*. reported that alluaudite-type

$Na_2Fe_2(SO_4)_3$ had the highest Fe^{2+}/Fe^{3+} redox potential (~ 3.8 V) [83]. Pyrite-type FeS_2 and

organic compounds have also been studied [84, 85].

1.3.3. Anode materials for Na-ion batteries

Although graphite is the most common anode active material for LIBs, Na^+ ions are hardly intercalated in the graphite [86]. Co-intercalation of Na^+ ions and diglyme into the graphite has been observed, but the capacity was only ~ 100 mAh g^{-1} [87]. Thus, in addition to the development of cathode materials, the development of anode materials for NIBs is also crucial. Hard carbon has been extensively studied as an anode material [88, 89]. $NaTi_2(PO_4)_3$ can also be used as an anode [90, 91]. Some elements, such as Sn, Sb, and P, are used since they form binary alloys or compounds with Na [92-94]. While the Sn, Sb, and P anodes exhibit a large capacity, their cycle performances are generally poor due to the significant volume expansion and particle fragmentation. Organic active materials are also promising anode materials due to their variety of structures [95].

1.3.4. Other components

The typical salts of the electrolyte for the NIBs are $NaPF_6$ and $NaClO_4$. As in the case of LIBs, PC, EC, DMC, and DEC are widely used as solvents. As separators in NIB experiments, glass fiber filters are frequently used in addition to microporous polyolefin membranes. While the Cu foil is used as an anode current collector for the LIBs, the Al foil can be used in the NIBs, since Na does not form alloys with Al metal. The use of Al foil can further reduce the battery cost.

1.4. Density Functional Theory for Battery Research

Over the past decades, computer simulations have become an increasingly important tool in materials science, both as an aid to interpret experimental data and as a means of refining and understanding the materials at atomic-level models. Consequently, the presence of computational approaches in battery research is increasing as well [96-98]. Theoretical simulations are powerful tools to elucidate microscopic phenomena, which are often impossible to measure experimentally. Primarily, density functional theory (DFT) has been widely employed in battery research due to the relatively high accuracy and acceptable computational cost. From the DFT calculations, many important material properties, such as intercalation voltages, migration barriers, and phase stabilities, can be predicted. In this section, the basic ideas of the DFT and its application to battery research are briefly introduced.

1.4.1. Basics of DFT

1.4.1.1. Schrödinger equation for a hydrogen atom

In quantum mechanics, which underlies the DFT, the dynamics of a wavefunction is described by the Schrödinger equation:

$$\left(-\frac{\hbar^2}{2m} \nabla^2 + v(\mathbf{r}) \right) \psi(\mathbf{r}) = E\psi(\mathbf{r}) \tag{1-6}$$

Note that the equation above is nonrelativistic and time-independent. The Schrödinger equation can be analytically solved only for a single-particle (electron) system.

1.4.1.2. Schrödinger equation in a many-body system

A quantum system generally consists of many nuclei and electrons. Unfortunately, the multiple orbitals of even the simplest molecule cannot be solved and expressed analytically. Therefore, many approximations must be implemented to render computational problems tractable. The first approximation takes into account the different nature of the nuclei and the electrons. Since a nucleus has more than 1800 times the mass of an electron, the motions of the nuclei and the electrons can be split into two different physical problems. In other words, the nuclei can be regarded as immobile during the calculations of the electronic states. This approximation is called Born-Oppenheimer approximation. In an N-electron system, the Hamiltonian can be written as follows:

$$H = T + U + V \tag{1-7}$$

$$T = -\frac{\hbar^2}{2m} \sum_i \nabla_i^2 \tag{1-8}$$

$$U = \frac{1}{2} \sum_{i \neq j} \frac{e^2}{|\mathbf{r}_i - \mathbf{r}_j|} \tag{1-9}$$

$$V = \sum_i v_{ext}(\mathbf{r}_i) \tag{1-10}$$

where e is the elementary electric charge. $\mathbf{r}$ and $\mathbf{R}$ are the positions of an electron and a nucleus, respectively. The T, U, and V terms represent the kinetic energies of the electrons, the interaction between the different electrons, and the external potential. The Schrödinger equation corresponding to the Hamiltonian is expressed as:

$$H\psi(\mathbf{r}_1, ..., \mathbf{r}_N) = E\psi(\mathbf{r}_1, ..., \mathbf{r}_N) \tag{1-11}$$

Here, the wave function is a function of $3N$ coordinates. Equation (1-11) is intractable because of the large number of variables ($3N$) and the electron-electron interactions. In other words, the Schrödinger equation in Eq. (1-11) is a many-body problem. Although many-body problems appear to be impossible to solve, the DFT offers an alternative route to a solution.

1.4.1.3. Hohenberg-Kohn theorem

The DFT is based on Hohenberg-Kohn theorems, which are an effective approach to solve the many-body problem [99]. The first Hohenberg-Kohn theorem states, "The external potential ($v_{ext}(\mathbf{r})$) is a unique functional of the electron density $n(\mathbf{r})$." The first theorem also means the electron density $n(\mathbf{r})$ uniquely determines all ground-state properties, since $v_{ext}(\mathbf{r})$ fixes the Hamiltonian H, and H determines a ground-state wave function. That is, the wavefunction $\psi(\mathbf{r}_1, \ldots, \mathbf{r}_N)$, the energy E and other properties of the ground-state are unique functionals of $n(\mathbf{r})$. This result is significant because the electron density $n(\mathbf{r})$, which is a function of only three variables, can be used to solve the Schrödinger equation, instead of $\psi(\mathbf{r}_1, \ldots, \mathbf{r}_N)$, which is a function of $3N$ variables.

The second Hohenberg-Kohn theorem is that "The energy $E[n(\mathbf{r})]$ is minimized for the correct $n(\mathbf{r})$." This statement means that the variational principle is applicable for the electron density:

$$E\left[n_0(\mathbf{r})\right] \leq E\left[n'(\mathbf{r})\right] \tag{1-12}$$

where $n_0(\mathbf{r})$ is the correct electron density, and $n'(\mathbf{r})$ is another density. Thus, in order to solve the Schrodinger equation, one needs to vary the electron density to minimize the energy.

Although the Hohenberg-Kohn theorems state the existence of the functionals, they do not state anything about the actual form of the functionals. Therefore, some approximations to the functionals are required in order to determine the ground state. The most widely used method is the Kohn-Sham approach [100]. In this approach, Kohn and Sham introduced an approximation called "local-density approximation," and they constructed a fictitious system of non-interacting electrons. By solving new Schrödinger equations for the fictitious system, the ground state of the original system can be determined. Here, the Kohn-Sham approach is briefly explained.

In general, the energy functional is expressed as:

$$E[n] = T[n] + U[n] + V[n] \tag{1-13}$$

where $T[n]$, $U[n]$, and $V[n]$ are the kinetic energy, the electron-electron interaction energy, and the external potential energy, respectively. The forms of $T[n]$ and $U[n]$ are not known, whereas $V[n]$ is known. In order to rewrite the energy functional in Eq. (1-13), a non-interacting and single-particle kinetic energy $T_s[n]$ is introduced:

$$T_s[n] = -\frac{\hbar^2}{2m} \sum_i^N \int \phi_i^*(\mathbf{r}) \nabla^2 \phi_i(\mathbf{r}) d^3 r \tag{1-14}$$

Note that $T_s[n]$ is different from the true kinetic energy $T[n]$. Here, a set of wave function $\phi_i(\mathbf{r})$, which is called the Kohn-Sham wave function (orbital), is introduced.
Then, Eq. (1-13) can be rewritten as:

$$E[n] = T_s[n] + U_H[n] + E_{xc}[n] + V[n] \tag{1-15}$$

where $U_H[n]$ is the Hartree energy, which is given as:

$$U_H[n] = \frac{e^2}{2} \iint \frac{n(\mathbf{r})n(\mathbf{r'})}{|\mathbf{r} - \mathbf{r'}|} d^3r d^3r' \tag{1-16}$$

As can be seen from the above equation, the Hartree energy includes a so-called self-interaction. The correction for this artificial self-interaction is lumped together with the correction for the kinetic energy (= $T[n] - T_s[n]$) into a term called the exchange-correlation energy $E_{xc}[n]$. The minimization of the energy functional $E[n]$ requires that:

$$\begin{aligned}
\frac{\delta E[n(\mathbf{r})]}{\delta n(\mathbf{r})} &= \frac{\delta}{\delta n(\mathbf{r})} \left(T_s[n] + V[n] + U_H[n] + E_{xc}[n] \right) \\
&= \frac{\delta T_s[n]}{\delta n(\mathbf{r})} + v_{ext}(\mathbf{r}) + v_H(\mathbf{r}) + v_{xc}(\mathbf{r}) \\
&= 0
\end{aligned} \tag{1-17}$$

From these results, the following Kohn-Sham equation can be derived:

$$\left(-\frac{\hbar^2}{2m} \nabla^2 + v_{eff}(\mathbf{r}) \right) \phi_i(\mathbf{r}) = \epsilon_i \phi_i(\mathbf{r}) \tag{1-18}$$

where

$$v_{eff}(\mathbf{r}) = v_{ext}(\mathbf{r}) + v_H(\mathbf{r}) + v_{xc}(\mathbf{r}) \tag{1-19}$$

The Kohn-Sham equation yields the electron density:

$$n(\mathbf{r}) = \sum_{i=1}^{N} |\phi_i(\mathbf{r})|^2 \tag{1-20}$$

Equation (1-18) is a non-interacting and single-electron Schrödinger equation. Therefore, the many-body problem is successfully replaced with a set of single-electron equations. This fictitious system is denoted as the Kohn-Sham auxiliary system. Note that the electron density in Eq. (1-20) is the same as that in the original system.

In order to solve the Kohn-Sham equation, $v_H(\mathbf{r})$ and $v_{xc}(\mathbf{r})$ must be defined, but they depend on $n(\mathbf{r})$. Since $n(\mathbf{r})$ depends on $\phi_i(\mathbf{r})$, it is necessary to know $\phi_i(\mathbf{r})$. However, in order to know $\phi_i(\mathbf{r})$, it is required to solve the Kohn-Sham equation, which depends on $v_H(\mathbf{r})$ and $v_{xc}(\mathbf{r})$. To break this cycle, a method called self-consistent field (SCF) calculation is employed, as shown in Fig. 1-9. In the SCF calculation, the initial trial electron density is estimated, and the potentials are calculated from the estimated electron density. Then, the Kohn-Sham equations are solved, resulting in a new electron density. These calculations are iteratively performed until the difference between the old and new electron density converges within the given criteria. From this DFT calculation, total energy and other values of the system can be obtained.

1.4.1.5. Exchange correlation functionals

In order to solve the Kohn-Sham equations, the exchange-correlation functional $E_{xc}[n]$ must be specified. Since the exact form of $E_{xc}[n]$ is not known, some functionals have been used to approximate $E_{xc}[n]$. One of the most important types of approximations is the local-density approximation (LDA), which was proposed by Kohn and Sham [100]. The LDA is based on the results for a uniform electron gas and solely relies on the value of the electron density at each position. Despite the simple approximation, LDA achieves excellent results in many cases. Another standard approximation is the generalized gradient approximation (GGA). GGA takes into account the gradient of the electron density as well as the electron density. So far, many types of GGA functionals have been developed, including the Perdew-Burke-Ernzerhof (PBE) functional [101].

Estimate input electron density $n_{in}(\mathbf{r})$

Calculate effective potential

$$v_{eff}[n_{in}] = v_{ext} + v_H[n_{in}] + v_{xc}[n_{in}]$$

Solve Kohn-Sham equation

$$\left(-\frac{\hbar^2}{2m}\nabla^2 + v_{eff}[n_{in}]\right)\phi_i = \epsilon_i\phi_i$$

Replace the old density with the new one

$$n_{in} \longleftarrow n_{out}$$

Calculate a new electron density

$$n_{out}(\mathbf{r}) = \sum_{i=1}^{N}|\phi_i(\mathbf{r})|^2$$

$n_{out} = n_{in}$?

Done
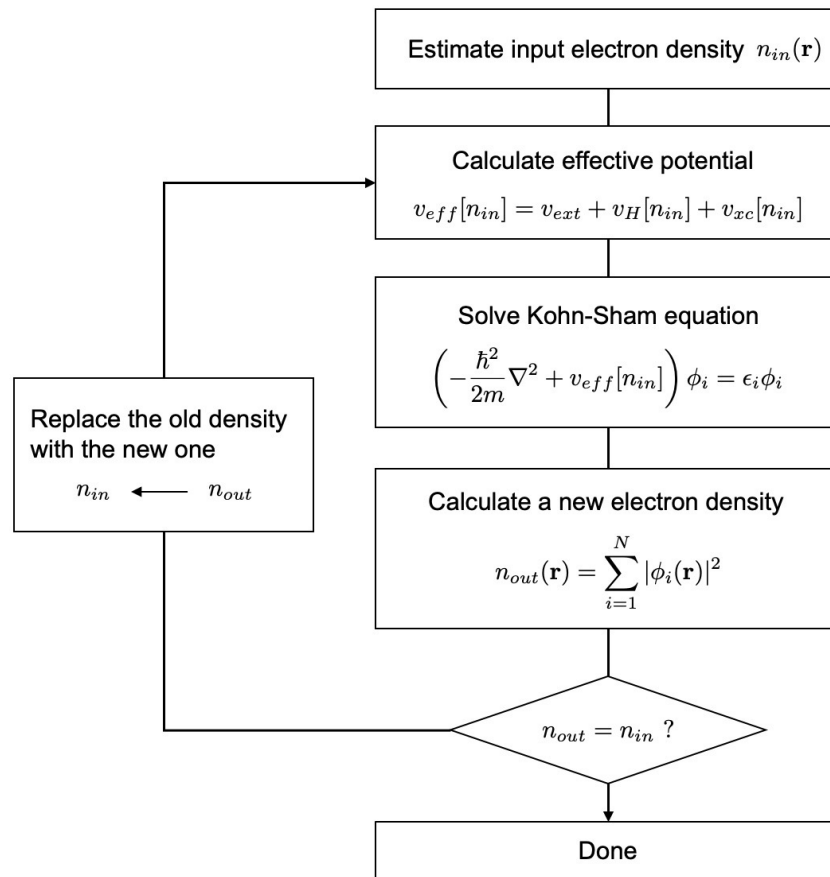
Figure 1-9 Schematic flow of SCF calculation of the electronic state for the Kohn-Sham equation.

1.4.1.6. Structural optimization

The crystal structures can be optimized in the DFT calculations. In this case, the force to the ions is calculated after each electronic calculation loop in Fig. 1-9, and then the ions are moved by a given step width according to the force. Various algorithms, such as the conjugate-gradient algorithm, are used to determine the direction of the ionic steps [102]. The ionic steps are repeated until the force or the energy is converged within the given criteria.

1.4.2. Phase stabilities and voltage profiles

1.4.2.1. Formation energy and convex hull

The DFT calculations yield total energies of crystal structures, and these energies can be approximated to Gibbs energies. Thus, the formation energies can be derived from the total energies. For example, the formation energy of a reaction $(1\text{-}x)\text{A} + x\text{B} \rightarrow \text{A}_{1\text{-}x}\text{B}_x$ is given as:

$$E_f(\text{A}_{1-x}\text{B}_x) = E(\text{A}_{1-x}\text{B}_x) - (1-x)E(\text{A}) - xE(\text{B}) \tag{1-21}$$

where E_f denotes the formation energy, and E represents the total energy of each compound.

Phase stabilities of materials are an important property because they are deeply related to materials synthesis and structural evolution during charge/discharge reactions. The "convex hull" concept is useful for grasping the phase stabilities. Figure 1-10 shows the convex hull concept as applied to the $\text{A}_{1\text{-}x}\text{B}_x$ system. The vertical axis denotes the formation energies of each state. In Fig. 1-10a, the formation energy of phase C is located above the horizontal line between A and B. In this case, a mixture of A and B is energetically more favorable than C, and thereby C decomposes to A and B. On the other hand, the formation energy of phase D is located below the horizontal line between A and B. Thus, D is energetically stable. In this way, the phase stability can be determined by the relative position to the line between two points. The line connecting stable points is called a convex hull. As shown in Fig. 1-10b, points above the convex hull are unstable, while those on the convex hull are stable.
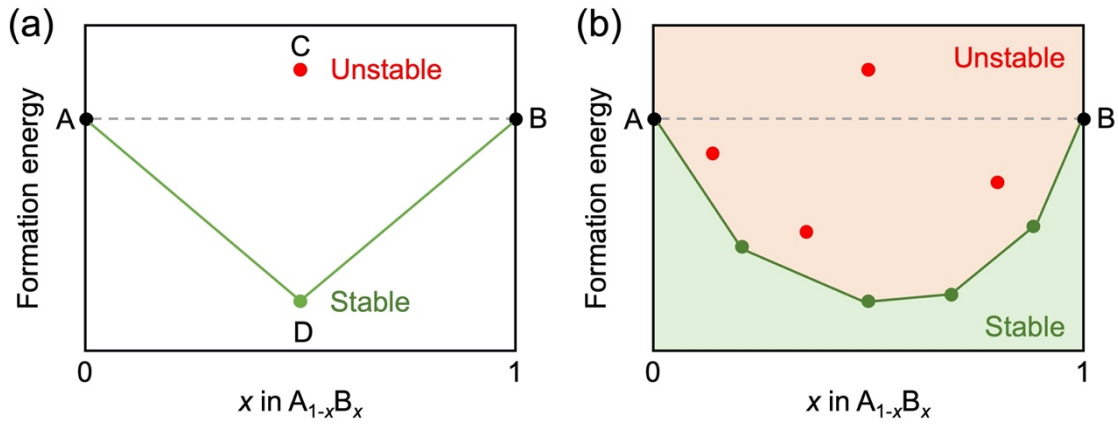
Figure 1-10 (a) Schematic formation energy diagram and **(b)** example of a convex hull.

1.4.2.2. Voltage profile

The average voltage between two phases can also be derived from the DFT energies. For example, the average voltage of A_xMO_2 (A = Li or Na) is given as [103]:

$$V = -\frac{E(A_{x_1}MO_2) - E(A_{x_2}MO_2) - (x_1 - x_2)E(A)}{(x_1 - x_2)F} \tag{1-22}$$

where E represents the total energy obtained from the DFT calculation. Since only stable phases emerge during the charge/discharge reaction, unstable phases above a convex hull are omitted from the voltage calculation.

1.4.3. Nudged elastic band method

The nudged elastic band (NEB) method is a method for finding a minimum energy path (MEP) of a transition between the given initial and final states [104, 105]. In the NEB method, a set of intermediate states (images) between the initial and final states is constructed. MEP is found by optimizing the intermediate images. A spring interaction between adjacent images is added in order to maintain equal spacing to the neighboring images. The NEB method is widely used to evaluate the migration barriers of ions.

1.4.4. *Ab initio* molecular dynamics

Ab initio molecular dynamics (AIMD) simulations are widely used to gain insight into ion diffusions. In the AIMD, the atomic forces are determined from first-principle calculations such as DFT calculations, but the dynamics of atoms are described by classical mechanics. That is, Newton's equations of motion are used to compute the positions and velocities of atoms. Since the equations cannot be solved (integrated) analytically for a system with multiple particles, numerical integration algorithms are used, such as the leapfrog algorithm and the velocity Verlet algorithm, which is a variant of the Verlet algorithm [106, 107]. The AIMD simulations can be run in various ensembles, such as the microcanonical (NVE) ensemble, the canonical (NVT) ensemble, and the isothermal-isobaric (NpT) ensemble. From the AIMD simulation, various types of information, such as the diffusion coefficient, ionic conductivity, activation energy, and diffusion paths, can be obtained.

1.5. Research Objective and Thesis Overview

Although the NIBs are a promising alternative to the LIBs, there is room for improvement. Notably, the development of new cathode materials is vital. Therefore, this thesis aims to elucidate the electrochemical properties of three types of promising cathode materials and provide new material design guidelines by experiments and DFT calculations. The thesis also demonstrates that the combination of experimental and computational methods is a powerful tool for battery materials research. The structure of the thesis is as follows:

Chapter 1 introduces the basic principles of LIBs and NIBs. The fundamentals of DFT are also explained.

Chapter 2 discusses the Ca-substitution effect on P3-type layered Na_xCoO_2. While Na_xCoO_2 is not a practical material due to the high cost of Co, this material is selected as a model of a typical layered oxide. It was found that Ca-substitution kinetically hindered the irreversible phase transition during the charge/discharge reaction and improved the cycle performance of the layered oxide.

Chapter 3 explores the factors limiting the three-Na^+ extraction from $Na_3V_2(PO_4)_3$. It was elucidated that the third-Na^+ extraction was prohibited due to the high voltage and large activation energy.

Chapter 4 investigates the electrochemical property of $NaMF_3$ (M = Fe, Mn, Co) prepared by mechanochemical ball milling. $NaFeF_3$ and $NaMnF_3$ exhibited better electrochemical performance than previous reports due to the two-step carbon mixing. $NaCoF_3$ did not show the electrochemical activity because of the high redox voltage.

Chapter 5 summarizes the thesis.

References

[1]   J.-M. Tarascon and M. Armand, *Nature*, **414** (2001) 359–367.

[2]   M. S. Whittingham, *Science*, **192** (1976) 1126–1127.

[3]   D. W. Murphy, F. J. Di Salvo, J. N. Carides, and J. V. Waszczak, *Mater. Res. Bull.*, **13** (1978) 1395–1402.

[4]   M. Lazzari and B. Scrosati, *J. Electrochem. Soc.*, **127** (1980) 773–774.

[5]   K. Mizushima, P. C. Jones, P. J. Wiseman, and J. B. Goodenough, *Mater. Res. Bull.*, **15** (1980) 783–789.

[6]   R. Yazami and P. Touzain, *J. Power Sources*, **9** (1983) 365–371.

[7]   A. Yoshino, K. Sanechika, and T. Nakajima, Japanese Patent No. 1989293

[8]   P. Poizot, S. Laruelle, S. Grugeon, L. Dupont, and J.-M. Tarascon, *Nature*, **407** (2000) 496–499.

[9]   F. Badway, N. Pereira, F. Cosandey, and G. G. Amatucci, *J. Electrochem. Soc.*, **150** (2003) A1209–A1218.

[10]   F. Badway, F. Cosandey, N. Pereira, and G. G. Amatucci, *J. Electrochem. Soc.*, **150** (2003) A1318–A1327.

[11]   M. M. Thackeray, P. J. Johnson, L. A. de Picciotto, P. G. Bruce, and J. B. Goodenough, *Mater. Res. Bull.*, **19** (1984) 179–187.

[12]   A. K. Padhi, K. S. Nanjundaswamy, and J. B. Goodenough, *J. Electrochem. Soc.*, **144** (1997) 1188–1194.

[13]   S. Albrecht, J. Kümpers, M. Kruft, S. Malcus, C. Vogler, M. Wahl, and M. Wohlfahrt-Mehrens, *J. Power Sources*, **119–121** (2003) 178–183.

[14]   N. Yabuuchi and T. Ohzuku, *J. Power Sources*, **119–121** (2003) 171–174.

[15]   J.-M. Tarascon, E. Wang, F. K. Shokoohi, W. R. McKinnon, and S. Colson, *J. Electrochem. Soc.*, **138** (1991) 2859–2864.

[16]   M. Konarova and I. Taniguchi, *J. Power Sources*, **195** (2010) 3661–3667.

[17]   K. S. Nanjundaswamy, A. K. Padhi, J. B. Goodenough, S. Okada, H. Ohtsuka, H. Arai, and J. Yamaki, *Solid State Ionics*, **92** (1996) 1–10.

[18]   H. Huang, S.-C. Yin, T. Kerr, N. Taylor, and L. F. Nazar, *Adv. Mater.*, **14** (2002) 1525–1528.

[19]   J. Barker, M. Y. Saidi, and J. L. Swoyer, *J. Electrochem. Soc.*, **150** (2003) A1394–A1398.

[20]   H. Arai, S. Okada, Y. Sakurai, and J. Yamaki, *J. Power Sources*, **68** (1997) 716–719.

[21]   K. Momma and F. Izumi, *J. Appl. Crystallogr.*, **44** (2011) 1272–1276.

[22]   R. Fong, U. von Sacken, and J. R. Dahn, *J. Electrochem. Soc.*, **137** (1990) 2009–2013.

[23]   J. R. Dahn, A. K. Sleigh, H. Shi, J. N. Reimers, Q. Zhong, and B. M. Way, *Electrochim. Acta*, **38** (1993) 1179–1191.

[24]   W. Xing, J. S. Xue, T. Zheng, A. Gibaud, and J. R. Dahn, *J. Electrochem. Soc.*, **143** (1996) 3482–3491.

[25]   E. Ferg, R. J. Gummow, A. de Kock, and M. M. Thackeray, *J. Electrochem. Soc.*, **141** (1994) L147–L150.

[26]   T. Ohzuku, A. Ueda, and N. Yamamoto, *J. Electrochem. Soc.*, **142** (1995) 1431–1435.

[27]   J. Wang, I. D. Raistrick, and R. A. Huggins, *J. Electrochem. Soc.*, **133** (1986) 457–460.

[28]   C. J. Wen and R. A. Huggins, *J. Solid State Chem.*, **37** (1981) 271–278.

[29]   *Sony's New Nexelion Hybrid Lithium Ion Batteries To Have Thirty-Percent More Capacity Than Conventional Offering*, Sony Corporation, https://www.sony.net/SonyInfo/News/Press/200502/05-006E/, (2005).

[30] J. B. Goodenough and Y. Kim, *Chem. Mater.*, **22** (2010) 587–603.

[31] E. Peled, *J. Electrochem. Soc.*, **126** (1979) 2047–2051.

[32] *Press release: Faradion receives first order of Sodium-ion Batteries for Australian Market*, Faradion, https://www.faradion.co.uk/faradion-receives-first-order-of-sodium-ion-batteries-for-australian-market/, (2020).

[33] K. F. Clark, *Mineral Composition of Rocks*, in: R. S. Carmichael (Ed.) *CRC Practical Handbook of Physical Properties of Rocks and Minerals*, CRC Press, Boca Raton, 1989, pp. 1–137.

[34] J.-J. Braconnier, C. Delmas, C. Fouassier, and P. Hagenmuller, *Mater. Res. Bull.*, **15** (1980) 1797–1804.

[35] C. Delmas, J.-J. Braconnier, C. Fouassier, and P. Hagenmuller, *Solid State Ionics*, **3–4** (1981) 165–169.

[36] J.-J. Braconnier, C. Delmas, and P. Hagenmuller, *Mater. Res. Bull.*, **17** (1982) 993–1000.

[37] A. Maazaz, C. Delmas, and P. Hagenmuller, *J. Inclusion Phenom.*, **1** (1983) 45–51.

[38] A. Mendiboure, C. Delmas, and P. Hagenmuller, *J. Solid State Chem.*, **57** (1985) 323–331.

[39] D. Hamani, M. Ati, J.-M. Tarascon, and P. Rozier, *Electrochem. Commun.*, **13** (2011) 938–941.

[40] X. Xia and J. R. Dahn, *Electrochem. Solid-State Lett.*, **15** (2012) A1–A4.

[41] N. Yabuuchi, H. Yoshida, and S. Komaba, *Electrochemistry*, **80** (2012) 716–719.

[42] C. Delmas, C. Fouassier, and P. Hagenmuller, *Physica B+C*, **99** (1980) 81–85.

[43] Y. Lei, X. Li, L. Liu, and G. Ceder, *Chem. Mater.*, **26** (2014) 5288–5296.

[44] N. Yabuuchi, M. Kajiyama, J. Iwatate, H. Nishikawa, S. Hitomi, R. Okuyama, R. Usui, Y. Yamada, and S. Komaba, *Nature Mater.*, **11** (2012) 512–517.

[45] S. Komaba, N. Yabuuchi, T. Nakayama, A. Ogata, T. Ishikawa, and I. Nakai, *lnorg. Chem.*, **51** (2012) 6211–6220.

[46] H. Yoshida, N. Yabuuchi, and S. Komaba, *Electrochem. Commun.*, **34** (2013) 60–63.

[47] M. Sathiya, K. Hemalatha, K. Ramesha, J.-M. Tarascon, and A. S. Prakash, *Chem. Mater.*, **24** (2012) 1846–1853.

[48] D. Kim, E. Lee, M. Slater, W. Lu, S. Rood, and C. S. Johnson, *Electrochem. Commun.*, **18** (2012) 66–69.

[49] X. Li, D. Wu, Y.-N. Zhou, L. Liu, X.-Q. Yang, and G. Ceder, *Electrochem. Commun.*, **49** (2014) 51–54.

[50] P. Vassilaras, S. T. Dacek, H. Kim, T. T. Fister, S. Kim, G. Ceder, and J. C. Kim, *J. Electrochem. Soc.*, **164** (2017) A3484–A3486.

[51] X. Ma, H. Chen, and G. Ceder, *J. Electrochem. Soc.*, **158** (2011) A1307–A1312.

[52] R. Berthelot, D. Carlier, and C. Delmas, *Nature Mater.*, **10** (2011) 74–80.

[53] M. D. Radin, J. Alvarado, Y. S. Meng, and A. Van der Ven, *Nano Lett.*, **17** (2017) 7789–7795.

[54] J. B. Goodenough, H. Y.-P. Hong, and J. A. Kafalas, *Mater. Res. Bull.*, **11** (1976) 203–220.

[55] Y. Uebou, T. Kiyabu, S. Okada, and J. Yamaki, *The Reports of lnstitute of Advanced Material Study, Kyushu University*, **16** (2002) 1–5.

[56] L. S. Plashnitsa, E. Kobayashi, Y. Noguchi, S. Okada, and J. Yamaki, *J. Electrochem. Soc.*, **157** (2010) A536–A543.

[57] S. Y. Lim, H. Kim, R. A. Shakoor, Y. Jung, and J. W. Choi, *J. Electrochem. Soc.*, **159** (2012) A1393–A1397.

[58] Z. Jian, W. Han, X. Lu, H. Yang, Y.-S. Hu, J. Zhou, Z. Zhou, J. Li, W. Chen, D. Chen, and L. Chen, *Adv. Energy Mater.*, **3** (2013) 156–160.

[59] K. Saravanan, C. W. Mason, A. Rudola, K. H. Wong, and P. Balaya, *Adv. Energy Mater.*, **3** (2013) 444–450.

[60] F. Lalère, V. Seznec, M. Courty, R. David, J.-N. Chotard, and C. Masquelier, *J. Mater. Chem. A*, **3** (2015) 16198–16205.

[61] M. J. Aragón, P. Lavela, R. Alcántara, and J. L. Tirado, *Electrochim. Acta*, **180** (2015) 824–830.

[62] M. J. Aragón, P. Lavela, G. F. Ortiz, and J. L. Tirado, *ChemElectroChem*, **2** (2015) 995–1002.

[63] R. Liu, G. Xu, Q. Li, S. Zheng, G. Zheng, Z. Gong, Y. Li, E. Kruskop, R. Fu, Z. Chen, K. Amine, and Y. Yang, *ACS. Appl. Mater. Interfaces*, **9** (2017) 43632–43639.

[64] A. Inoishi, Y. Yoshioka, L. Zhao, A. Kitajou, and S. Okada, *ChemElectroChem*, **4** (2017) 2755–2759.

[65] B. M. de Boisse, J. Ming, S. Nishimura, and A. Yamada, *J. Electrochem. Soc.*, **163** (2016) A1469–A1473.

[66] F. Chen, V. M. Kovrugin, R. David, O. Mentré, F. Fauth, J.-N. Chotard, and C. Masquelier, *Small Methods*, **3** (2018) 1800218.

[67] H. Gao, Y. Li, K. Park, and J. B. Goodenough, *Chem. Mater.*, **28** (2016) 6553–6559.

[68] H. Gao, I. D. Seymour, S. Xin, L. Xue, G. Henkelman, and J. B. Goodenough, *J. Am. Chem. Soc.*, **140** (2018) 18192–18199.

[69] J. Wang, Y. Wang, D. H. Seo, T. Shi, S. Chen, Y. Tian, H. Kim, and G. Ceder, *Adv. Energy Mater.*, **10** (2020) 1903968.

[70] K. Kawai, W. Zhao, S. Nishimura, and A. Yamada, *ACS. Appl. Energy Mater.*, **1** (2018) 928–931.

[71] K. Kawai, D. Asakura, S. Nishimura, and A. Yamada, *Chem. Commun.*, **55** (2019) 13717–13720.

[72] I. D. Gocheva, M. Nishijima, T. Doi, S. Okada, J. Yamaki, and T. Nishida, *J. Power Sources*, **187** (2009) 247–252.

[73] M. Nishijima, I. D. Gocheva, S. Okada, T. Doi, J. Yamaki, and T. Nishida, *J. Power Sources*, **190** (2009) 558–562.

[74] K. V. Kravchyk, T. Zünd, M. Wörle, M. V. Kovalenko, and M. I. Bodnarchuk, *Chem. Mater.*, **30** (2018) 1825–1829.

[75] A. Martin, M.-L. Doublet, E. Kemnitz, and N. Pinna, *Adv. Funct. Mater.*, **28** (2018) 1802057.

[76] A. Kitajou, H. Komatsu, K. Chihara, I. D. Gocheva, S. Okada, and J. Yamaki, *J. Power Sources*, **198** (2012) 389–392.

[77] Y. Yamada, T. Doi, I. Tanaka, S. Okada, and J. Yamaki, *J. Power Sources*, **196** (2011) 4837–4841.

[78] N. Dimov, A. Nishimura, K. Chihara, A. Kitajou, I. D. Gocheva, and S. Okada, *Electrochim. Acta*, **110** (2013) 214–220.

[79] J. Nava-Avendaño, M. E. Arroyo-de Dompablo, C. Frontera, J. A. Ayllón, and M. R. Palacín, *Solid State Ionics*, **278** (2015) 106–113.

[80] K. Chihara, A. Kitajou, I. D. Gocheva, S. Okada, and J. Yamaki, *J. Power Sources*, **227** (2013) 80–85.

[81] R. A. Shakoor, D.-H. Seo, H. Kim, Y.-U. Park, J. Kim, S.-W. Kim, H. Gwon, S. Lee, and K. Kang, *J. Mater. Chem.*, **22** (2012) 20535–20541.

[82] J. Barker, M. Y. Saidi, and J. L. Swoyer, *Electrochem. Solid-State Lett.*, **6** (2003) A1–A4.

[83] P. Barpanda, G. Oyama, S. Nishimura, S.-C. Chung, and A. Yamada, *Nat. Commun.*, **5** (2014) 4358.

[84] A. Kitajou, J. Yamaguchi, S. Hara, and S. Okada, *J. Power Sources*, **247** (2014) 391–395.

[85] K. Chihara, N. Chujo, A. Kitajou, and S. Okada, *Electrochim. Acta*, **110** (2013) 240–246.

[86] P. Ge and M. Fouletier, *Solid State Ionics*, **28-30** (1988) 1172–1175.

[87] B. Jache and P. Adelhelm, *Angew. Chem. Int. Ed.*, **53** (2014) 10169–10173.

[88] D. A. Stevens and J. R. Dahn, *J. Electrochem. Soc.*, **147** (2000) 1271–1273.

[89] M. Dahbi, N. Yabuuchi, K. Kubota, K. Tokiwa, and S. Komaba, *Phys. Chem. Chem. Phys.*, **16** (2014) 15007–15028.

[90] C. Delmas, F. Cherkaoui, A. Nadiri, and P. Hagenmuller, *Mater. Res. Bull.*, **22** (1987) 631–639.

[91] C. Delmas, A. Nadiri, and J. L. Soubeyroux, *Solid State Ionics*, **28-30** (1988) 419–423.

[92] S. Komaba, Y. Matsuura, T. Ishikawa, N. Yabuuchi, W. Murata, and S. Kuze, *Electrochem. Commun.*, **21** (2012) 65–68.

[93] J. Qian, Y. Chen, L. Wu, Y. Cao, X. Ai, and H. Yang, *Chem. Commun.*, **48** (2012) 7070–7072.

[94] Y. Kim, Y. Park, A. Choi, N.-S. Choi, J. Kim, J. Lee, J. H. Ryu, S. M. Oh, and K. T. Lee, *Adv. Mater.*, **25** (2013) 3045–3049.

[95] Y. Park, D. S. Shin, S. H. Woo, N. S. Choi, K. H. Shin, S. M. Oh, K. T. Lee, and S. Y. Hong, *Adv. Mater.*, **24** (2012) 3562–3567.

[96] S. P. Ong, V. L. Chevrier, G. Hautier, A. Jain, C. Moore, S. Kim, X. Ma, and G. Ceder, *Energy Environ. Sci.*, **4** (2011) 3680–3688.

[97] M. S. Islam and C. A. J. Fisher, *Chem. Soc. Rev.*, **43** (2014) 185–204.

[98] A. Van Der Ven, Z. Deng, S. Banerjee, and S. P. Ong, *Chem. Rev.*, (2020) in press.

[99] P. Hohenberg and W. Kohn, *Phys. Rev.*, **136** (1964) B864–B871.

[100] W. Kohn and L. J. Sham, *Phys. Rev.*, **140** (1965) A1133–A1138.

[101] J. P. Perdew, K. Burke, and M. Ernzerhof, *Phys. Rev. Lett.*, **77** (1996) 3865–3868.

[102] W. H. Press, S. A. Teukolsky, W. T. Vetterling, and B. P. Flannery, *Solution of Linear Algebraic Equations*, in: *Numerical Recipes. The Art of Scientific Computing*, Cambridge University Press, New York, 2007, pp. 37–109.

[103] M. K. Aydinol, A. F. Kohan, G. Ceder, K. Cho, and J. Joannopoulos, *Phys. Rev. B*, **56** (1997) 1354–1365.

[104] G. Mills, H. Jónsson, and G. K. Schenter, *Surface Science*, **324** (1995) 305–337.

[105] H. Jónsson, G. Mills, and K. W. Jacobsen, *Nudged elastic band method for finding minimum energy paths of transitions*, in: B. J. Berne, G. Ciccotti, D. F. Coker (Eds.) *Classical and Quantum Dynamics in Condensed Phase Simulations*, World Scientific, Farrer Road, 1998, pp. 385–404.

[106] L. Verlet, *Phys. Rev.*, **159** (1967) 98–103.

[107] W. C. Swope, H. C. Andersen, P. H. Berens, and K. R. Wilson, *J. Chem. Phys.*, **76** (1982) 637–649.

Chapter 2

An Experimental and First-principle Investigation of the Ca-substitution Effect on P3-type Layered Na$_x$CoO$_2$

2.1. Introduction

Layered sodium transition metal oxides, Na$_x$MO$_2$, have been extensively studied as promising cathode active materials for NIBs because of their facile synthesis and handling, as well as their relatively high energy densities [1–9]. Na$_x$MO$_2$ can have multiple structural types depending on the manner of oxygen atom stacking [10]. Figure 2-1 shows the representative structural types of Na$_x$MO$_2$: O1, P3, and O3. Here, "O" represents an "octahedral" Na site, and "P" represents a "prismatic" Na site. The number following "O" or "P" denotes the number of periodicities of the oxygen stacking. During the charge/discharge process of the layered oxides, they exhibit phase transitions from one structural type to another, accompanied by MO$_2$ slab gliding [11, 12]. Since the phase transition leads to capacity fading, various elemental substitutions of transition metals have been investigated to suppress the irreversible phase transitions during the charge/discharge process [13–18]. The phase transition can also be

suppressed by replacing Na$^+$ ions (1.02 Å; coordination number = 6) with Ca^{2+} ions (1.0 Å; coordination number = 6) that have a similar ionic radius [19–21]. Matsui *et al.* previously reported that the cycling performance of the P2-type Na$_{2/3}$CoO$_2$ is improved by Ca substitution [22]. Despite the improved cycling performance, the overpotential of the cathode was increased, because the doped Ca^{2+} ions hindered the Na$^+$ ion diffusion in the layered structure. The shrinkage of the lattice constant by the Ca substitution also interferes with the kinetics of Na$^+$ ions.

In this chapter, the Ca-substituted P3-type Na$_x$CoO$_2$ was synthesized and its electrochemical properties were investigated. The Ca substitution improved the cycling performance of P3-type Na$_x$CoO$_2$ without an increase in overpotential. *Ab initio* calculations were also conducted to understand the effect of Ca-substitution on the suppression of the phase transitions and the overpotential in the P3-type layered structure.
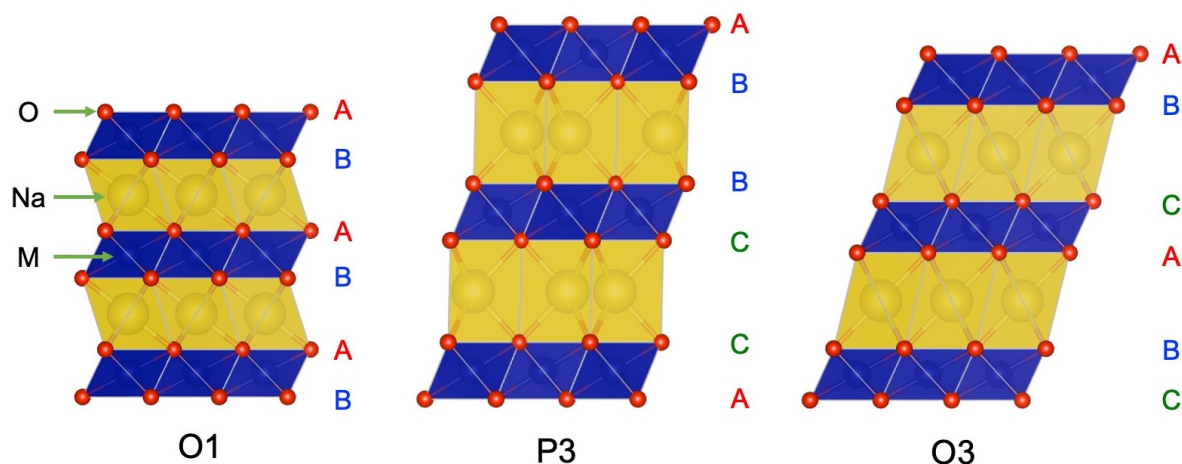

Figure 2-1 Oxygen stackings of the O1-, P3-, and O3-type layered structures. A, B, and C represent the relative positions of the oxygen atoms. The crystal structures were visualized by using VESTA [23].

2.2. Experimental

2.2.1. Materials synthesis and characterization

Na$_x$CoO$_2$ (NCO) and Ca-substituted Na$_x$CoO$_2$ (NCCO) were synthesized by a solid-state method. NaOH, Ca(OH)$_2$ and Co(OH)$_2$ were mixed in an agate mortar in an Ar-filled glove box. 15 wt.% of excess NaOH was used to compensate the evaporation of Na species during calcination. The mixed samples were pelletized and heated at 500 ºC under an oxygen flow for 36 hours.

The X-ray diffraction (XRD) experiments were performed using an X-ray diffractometer (Bruker D8 Advance) with Co Kα radiation. The Rietveld refinement was performed with RIETAN-FP [24]. Elemental analyses of the NCO and NCCO were performed using an ICP-AES (Horiba Jobin Yvon ULTIMA 2000).

2.2.2. Electrochemical tests

NCO and NCCO electrodes were prepared by mixing 80 wt.% of the active material, 10 wt.% of acetylene black (AB) and 10 wt.% of PVDF in n-methyl-2-pyrrolidone (NMP). The obtained electrode slurry was coated on Al foil and dried in a vacuum at 80 ºC.

The electrochemical tests were performed using two electrode cells (TJ-ACC; Tomcell Japan) with the prepared electrode as a working electrode, Na metal as a counter electrode and 1 M NaPF$_6$ in EC:DEC (1:1 in vol.%) 97 wt.% + FEC 3 wt.% as an electrolyte. Galvanostatic measurements were carried out using a BTS2004H battery testing system (NAGANO).

2.2.3. Computational methods

DFT calculations were performed with the projector augmented wave (PAW) approach [25, 26], which is implemented in the Vienna Ab initio Simulation Package (VASP) [27, 28]. The optB86b-vdW exchange-correlation functional [29, 30] was used to account for the Van der Waals interaction between CoO_2 layers [31, 32]. Hubbard U correction was not applied, since +U correction can lead to incorrect results for Na_xCoO_2 [31, 33]. The cutoff energy was set to 520 eV. A gamma-centered k-point for which the density is more than 500 / (number of atoms) was adopted.

   Structure generation and analysis were performed with the Pymatgen package [34]. For O1 structures, a $3 \times 3 \times 2$ supercell was generated from a CoO_2 (ICSD No. 88722) unit cell. For P3 structures, a $3 \times 3 \times 1$ supercell was generated from a $Na_{0.672}CoO_2$ (ICSD No. 59606) unit cell. For O3 structures, a $NaCoO_2$ (ICSD No. 6152) cell was manually transformed to a triclinic primitive cell, and then a $6 \times 3 \times 1$ supercell was generated from the triclinic cell. The compositions of the supercells of NCO and NCCO were represented as $Na_x \cdot Co_{18}O_{36}$ and $Na_x \cdot CaCo_{18}O_{36}$, respectively. In the NCO and NCCO supercells, there are various possible Na-(Ca)-vacancy orderings. All possible orderings within the supercells were enumerated with the Supercell program [35], and 30 structures with the lowest electrostatic energies were chosen. The most stable configurations at each composition were selected from the DFT calculations. The formation energies of NCO were calculated by using Eq. (2-1). O3-type $NaCoO_2$ and O1-type CoO_2 were used as references.

$$E_f\left(Na_x CoO_2\right) = E\left(Na_x CoO_2\right) - x E\left(NaCoO_2\right) - (1-x) E\left(CoO_2\right) \tag{2-1}$$

Here, E is the energy for each compound obtained from the DFT calculation.

The formation energies of NCCO were calculated by using Eq. (2-2). O3-$Na_{0.89}Ca_{0.056}CoO_2$ and O1-$Ca_{0.056}CoO_2$ were used as references.

$$
\begin{aligned}
E_f\left(Na_{0.89x'}Ca_{0.056}CoO_2\right) = {}& E\left(Na_{0.89x'}Ca_{0.056}CoO_2\right) \\
& - x'E\left(Na_{0.89}Ca_{0.056}CoO_2\right) \\
& - (1-x')E\left(Ca_{0.056}CoO_2\right)
\end{aligned}
\tag{2-2}
$$

The migration barriers for Na ions in P3-NCO and P3-NCCO were calculated by the Climbing Image Nudged Elastic Band (CI-NEB) method, which is implemented in VASP Transition State Theory (VTST) tools as an extension of VASP code [36–38]. In the NEB calculations, a $3 \times 6 \times 1$ supercell was used for the P3-type structure so that the hopping Na ions achieved a sufficient distance between their periodic images. The force is converged within 0.02 eV Å^{-1}.

2.3. Results and Discussion

2.3.1. Materials characterization

The XRD patterns of the as-prepared NCO and NCCO are shown in Fig. 2-2. For NCO, all the diffraction peaks are indexed as a P3-type layered oxide. The NCCO is also characterized as a P3 phase without any impurity phase. The small peaks at around 17º arise from the diffraction of Co Kβ radiation. In order to confirm that Ca^{2+} ions partially occupy the Na sites in the layered oxide, the Rietveld refinement of NCCO was carried out. Figure 2-3 shows the result of the Rietveld refinement. Note that the diffraction peak (16.5–17.6º) of Co Kβ radiation was

excluded from the refinement. The refined crystallographic data are shown in Table 2-1. NCCO has the P3-type structure although the lattice is monoclinic ($C2/m$). The small R_{wp} value (2.85%) and the large R_e value (29.71%) were obtained because of the large background and the small peak intensities in the XRD pattern. The Rietveld refinement with the Ca^{2+} ions in the Co sites was also performed, but the fitting was worse than that of the refinement with the Ca^{2+} ions in the Na sites. Therefore, it can be concluded that the substituted Ca^{2+} ions preferably occupy the Na sites, as illustrated in Fig. 2-4. This result is reasonable because the ionic radius of Ca^{2+} (1.0 Å) is similar to that of Na^+ (1.02 Å), whereas the Co ion has the smaller ionic radii (0.53–0.61 Å).

Figure 2-5 shows the scanning electron microscopy with energy dispersive X-ray spectroscopy (SEM-EDX) mapping. The distribution of Ca in the particles was uniform, which also suggests that the Ca^{2+} ions are incorporated with Na^+ ions in the van der Waals gap between the CoO_2 layers. The actual Na contents in the Ca-free and Ca-substituted materials determined by the inductively coupled plasma atomic emission spectroscopy (ICP-AES) measurements were $Na_{0.81}CoO_2$ and $Na_{0.69}Ca_{0.04}CoO_2$, respectively.
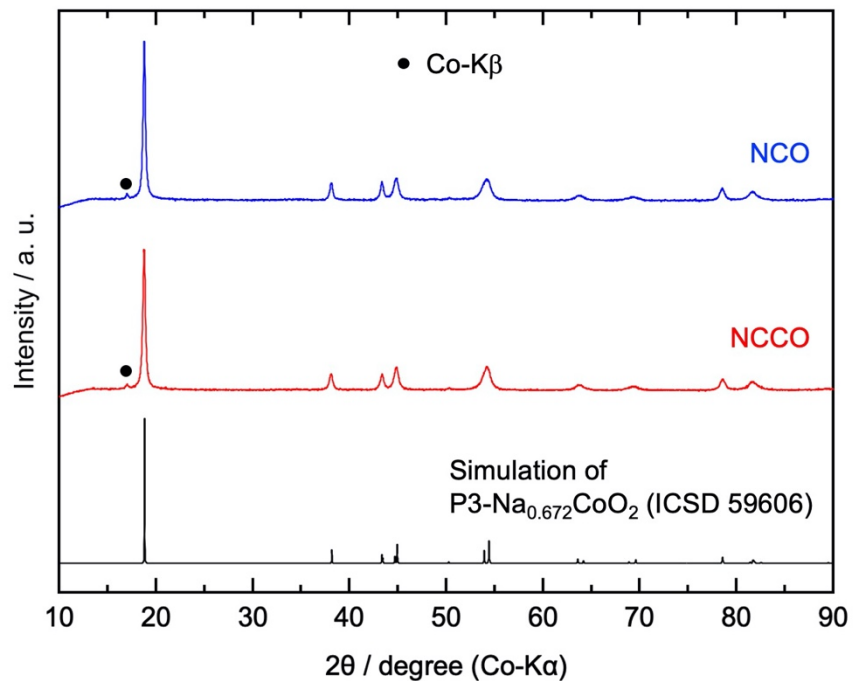
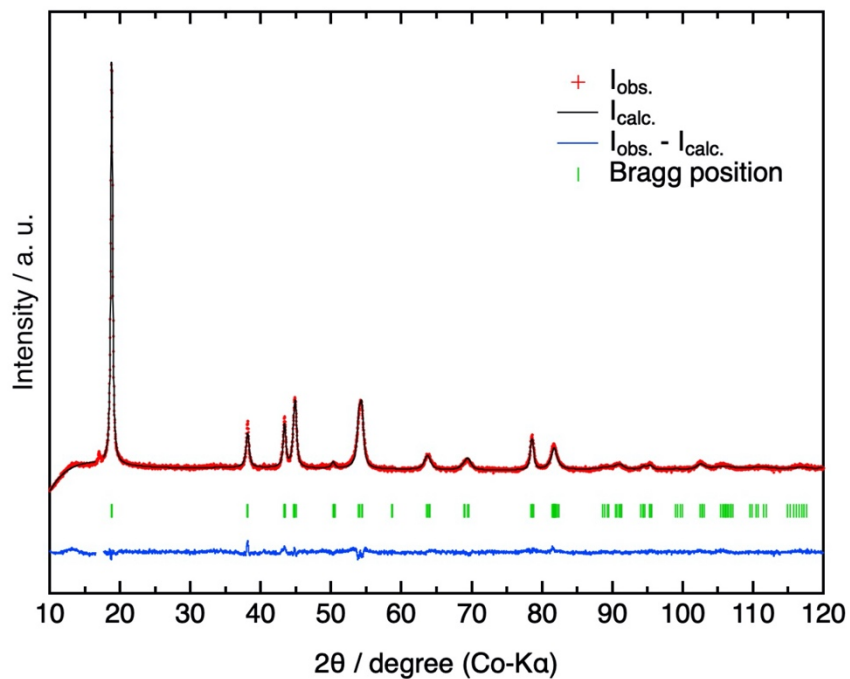**Figure 2-2** Powder XRD patterns of as-prepared NCO and NCCO.

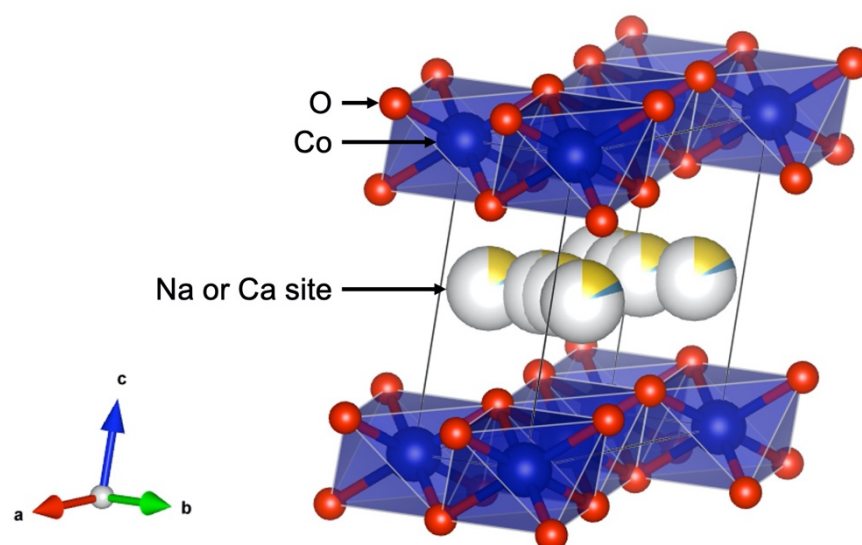**Figure 2-3** Rietveld refinement of the XRD pattern of as-prepared NCCO.

Figure 2-4 Refined crystal structure of NCCO.

Table 2-1 Refined crystallographic data for NCCO.

Space group	a / Å	b / Å	c / Å	α / °	β / °	γ / °
$C2/m$	4.9020(6)	2.8241(3)	5.7059(11)	90	106.189(11)	90

R_{wp} / %	R_e / %	R_{wp}/R_e / %	R_B / %	R_F /%
2.85	29.71	0.0960	1.02	0.69

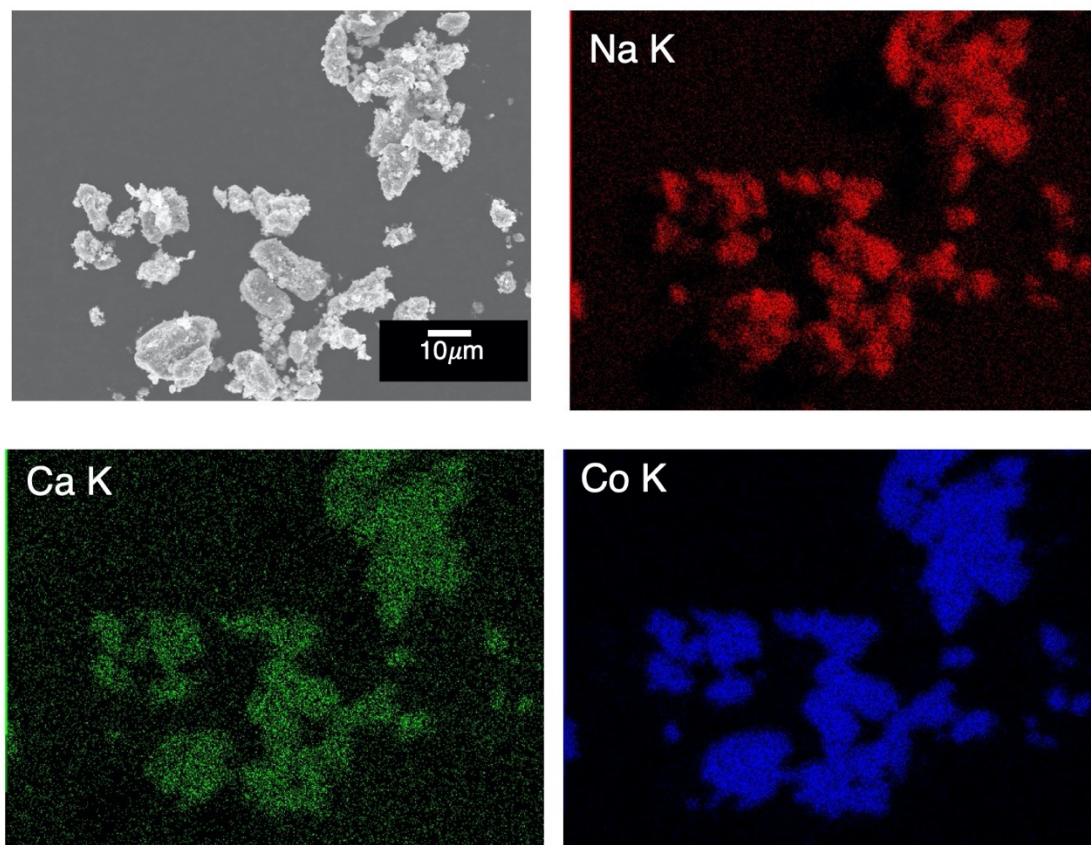| Atom	Site	g	x	y	Z	$U_{iso.}$ / Å^2
Na	8j	0.1822	0.7891(36)	0.0766(71)	0.5026(12)	0.02570
Ca	8j	0.0100	0.7891(36)	0.0766(71)	0.5026(12)	0.02570
Co	2a	1.0	0	0	0	0.00240
O	4i	1.0	0.3972(18)	0.0	0.1692(4)	0.00656

Figure 2-5 SEM-EDX mapping of NCCO.

2.3.2. Electrochemical properties and phase transitions of Na$_x$CoO$_2$ and Ca-substituted Na$_x$CoO$_2$

The electrochemical properties of the NCO and NCCO were measured using a half-cell against Na metal counter electrodes. Figure 2-6 shows the charge/discharge profiles of NCO and NCCO at the 3rd cycle at a current rate of C/20. Overall, the charge/discharge profiles are in good agreement with the O3-type NaCoO$_2$ or P3-type Na$_x$CoO$_2$ reported in the literature [1, 17]. The reversible capacity of NCCO (131 mAh g^{-1}) was slightly smaller than that of NCO (138 mAh g^{-1}), but its lower capacity corresponded to the substituted Ca^{2+} ion content. The first

discharge capacities of NCO and NCCO were 148 mAh g^{-1} and 133 mAh g^{-1}, respectively. The difference of the capacities was 15 mAh g^{-1}, which is roughly consistent with the capacity difference calculated from the amount of Na deficient induced by the Ca substitution. Even though the substituted Ca^{2+} ions would be expected to hinder the migration of the Na$^+$ ions, the NCCO showed even smaller hysteresis in the charge/discharge profile. The Ca substitution also improved the reversibility during the charge/discharge process. The Coulombic efficiency of the NCCO was 98.3%, while NCO showed a Coulombic efficiency of 95.5%. The improved Coulombic efficiency indicates that the irreversible phase transition at high voltage is suppressed by the Ca substitution. Moreover, the suppressed irreversibility led to a significant improvement in cycling performances, as shown in Fig. 2-7. The NCCO showed a capacity retention of 80.8% after 100 cycles, while the NCO showed severe capacity decay (capacity retention: 25.6%).

Next, to elucidate the origin of the capacity decay, *ex situ* XRD measurements were performed for both materials. Figure 2-8 shows the *ex situ* XRD patterns of the NCO and the NCCO during the charging process. The structural evolution of the NCO in Fig. 2-8a is in good agreement with the past reports [1, 39]. As shown in Fig. 2-8ab, the NCO and NCCO show monoclinic O'3 phases at 2.6 V and transform to P'3 phases upon Na extraction. At 2.7 V, the O'3 phase and P'3 phase coexisted in the NCO, whereas only the P'3 phase was observed in the NCCO. For both the NCO and the NCCO, another phase transition from P'3 to the hexagonal O3 phase was observed around 3.9 V. Except for the XRD patterns at 2.7 V, the NCO and the NCCO exhibited similar trends in the phase transitions during the charging up to 4.0 V.

In order to detect a trace of the irreversible phase transition, *ex situ* XRD measurements for overcharged NCO and NCCO cathodes were carried out. Figure 2-9ab respectively show the XRD patterns of the NCO and NCCO electrodes charged at 4.5 V. Since the Na

compositions of the as-prepared NCO and NCCO are different from each other, the direct comparison of the NCO and NCCO at the first cycle. Thus, the ex situ XRD was performed at the second cycle. Note that the electrolyte is likely to be partially decomposed as well as the sodium extraction during charging to 4.5 V. In order to determine the exact amount of sodium desorption, it is necessary to perform the ICP measurement. In Fig. 2-9ab, both materials charged at 4.5 V were characterized as O3-type structures. The peak intensity of the NCO was decreased after charging while that of the NCCO did not decrease significantly. Therefore, the crystallinity of the NCO was deteriorated after charging, whereas the NCCO retained the relatively good crystallinity. Based on the previous report, the NCO is expected to exhibit a phase transition from O3 phase to O1 phase at high voltage [32]. Therefore, the poor crystallinity of the charged NCO suggests that the irreversible O3-O1 phase transition partially occurred, and this phase transition led to the severe capacity decay of the NCO. On the other hand, the NCCO exhibited the superior capacity retention, since the Ca-substitution inhibited the irreversible phase transition during charging.

Even for the NCCO, the capacity continued decreasing during the cycles, as shown in Fig 2-7. This is due to the inevitable phase transitions (O'3-P'3-O3) in the Ca-substituted layered oxide. According to the report by Radin *et al.*, the phase transitions accompanied with the slab griding could lead to lattice-invariant shear of the active material particles [11]. The lattice-invariant shear induces microcracks in the particles, and the microcracks expose fresh surface of the active material to the electrolyte. As a result, a new SEI forms on the fresh surface of the active material, which leads to the capacity fading.
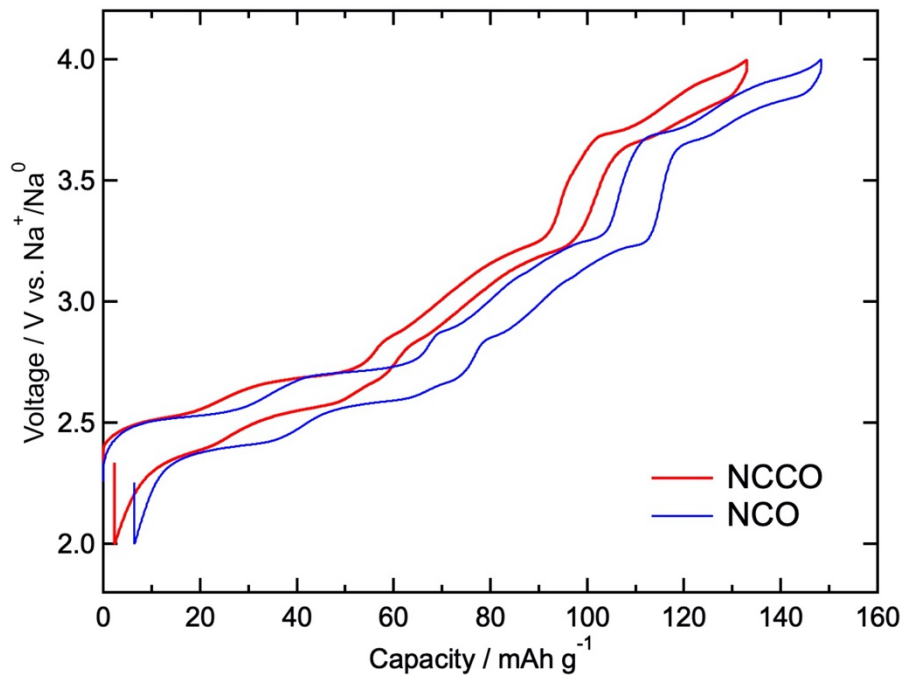
Figure 2-6 Charge/discharge profiles of NCO and NCCO at the 3rd cycle at a current rate of C/20.
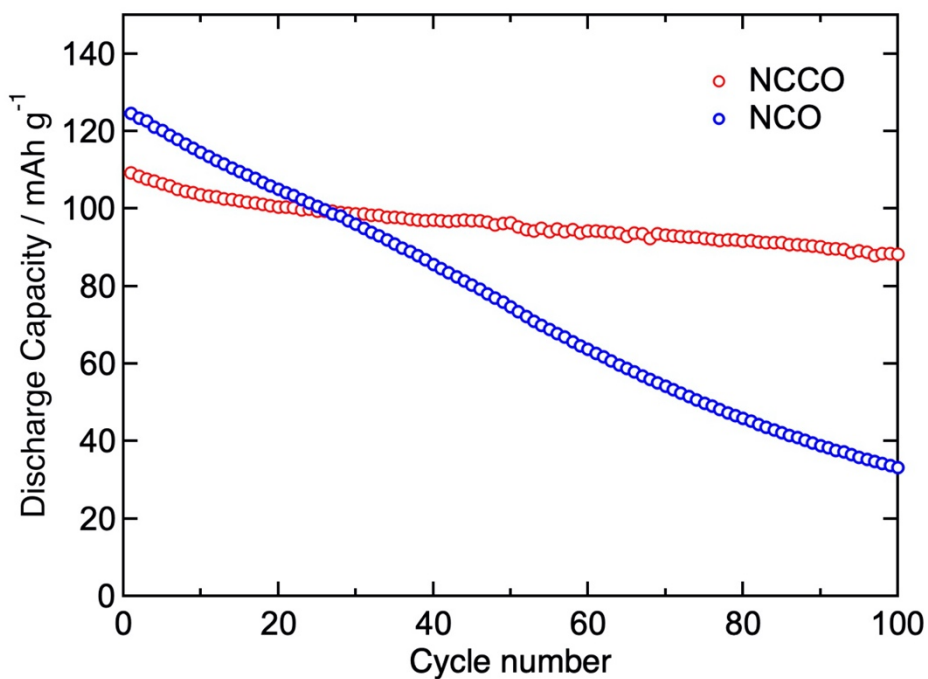

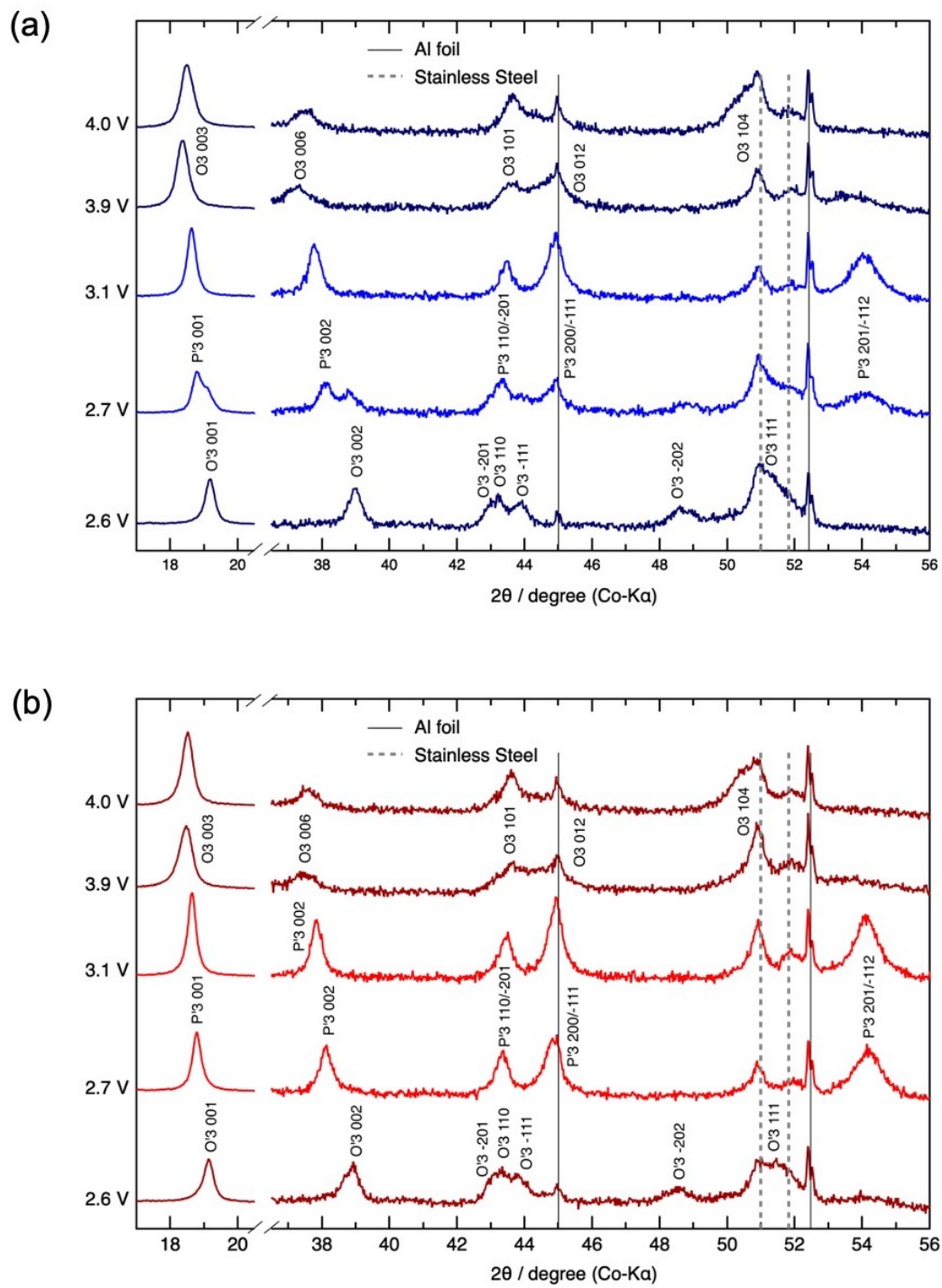**Figure 2-7** Cycle performance of NCO and NCCO at a current rate of 1C.

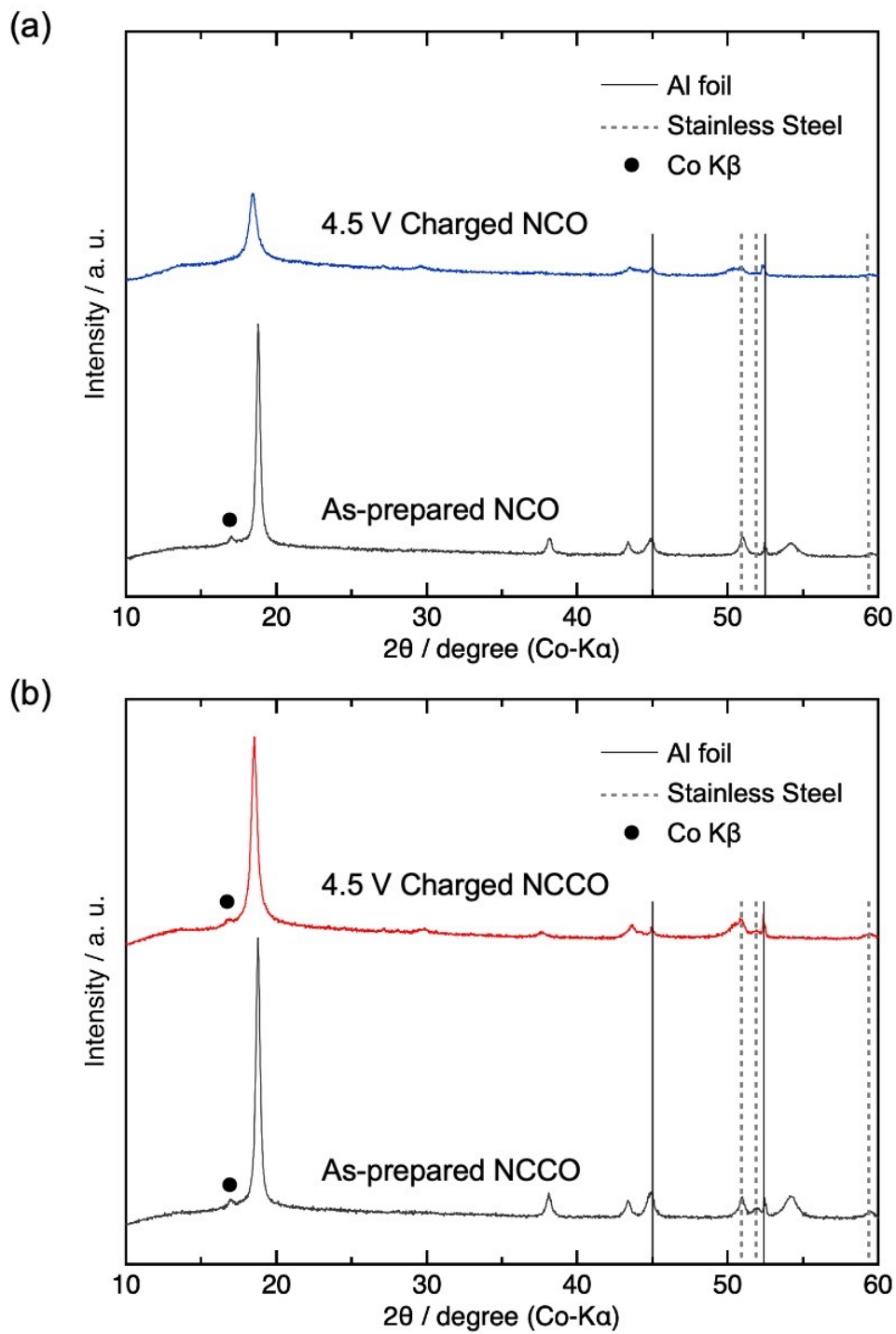**Figure 2-8** *Ex situ* XRD patterns of **(a)** NCO and **(b)** NCCO during the charging process at the second cycle.

Figure 2-9 *Ex situ* XRD patterns of **(a)** NCO and **(b)** NCCO charged at 4.5 V.

2.3.3. Phase stabilities of Na_xCoO_2 and Ca-substituted Na_xCoO_2

DFT calculations were performed with the VASP [27, 28] to investigate the Ca-substitution effect on the phase stability of Na_xCoO_2. In the calculations, supercells of $Na_x \cdot Co_{18}O_{36}$ and $Na_x \cdot CaCo_{18}O_{36}$ were used for the NCO and NCCO, respectively. The Ca content of $Na_x \cdot CaCo_{18}O_{36}$, which is also represented as $Na_xCa_{0.056}CoO_2$, is slightly higher than that of the experimentally synthesized NCCO due to the limitation of the available Ca sites in the supercells. Since the difference in the Ca content between the computational and experimental studies was small, the influence of compositional differences on the calculated properties such as phase stability was negligible.

Figure 2-10 shows the calculated formation energies and the convex hulls of the NCO and NCCO, respectively. Note that the Co oxidation state was used as a horizontal axis at the bottom of the figure, permitting a comparison of phase stabilities at the same Co oxidation state. O1-type CoO_2 and O3-type $NaCoO_2$ are used as reference states for NCO, and O1-type $Ca_{0.056}O_2$ and O3-type $Na_{0.89}Ca_{0.056}CoO_2$ are used as references for NCCO. The globally stable convex hulls are described with a solid black line. The areas shaded in red, green, and blue represent the ranges where the O1, O3, and P3 phases are the most stable, respectively. The other areas are expected to be two-phase regions. As shown in Fig. 2-10a, the O3 phase is the most stable among the three structural types in the range of $1.0 \geq x \geq 0.83$ in the case of the NCO. Upon Na extraction from $NaCoO_2$, the P3 becomes the most stable phase in $0.67 \geq x \geq 0.44$. This result is consistent with both the experimental results above and the past computational results [32]. The formation of the second O3 phase ($x = 0.33$) is also in good agreement with the experimental results discussed above. In addition, the O1 phase becomes thermodynamically favorable at the fully desodiated composition ($x = 0$), where the oxidation state of Co is 4.0. The region of $0.33 > x > 0$ is expected to be a two-phase region of the O3

and O1 phase. Therefore, the origin of the peak broadening of the charged Na_xCoO_2 observed in Fig. 2-9a is attributable to the O3-O1 phase transition.

The convex hull of the NCCO is shown in Fig. 2-10b. Since the mobility of the Ca^{2+} ions is presumably negligible compared with that of the Na^+ ions, the Ca^{2+} ions remain in the matrix even after the full extraction of Na^+ ions. Thus, the estimated composition of the fully desodiated phase becomes $Ca_{0.056}CoO_2$. As a result, the highest oxidation state of Co in $Na_xCa_{0.056}CoO_2$ does not exceed 3.89. Moreover, the oxidation state of the Co is not expected to be < 3.0 in the voltage range in the electrochemical tests above. Hence, the maximum Na content is limited to 0.89, where the composition is $Na_{0.89}Ca_{0.056}CoO_2$.

In the convex hull of NCCO, the structural evolution from O3, via P3 and O3 to O1, is consistent with NCO. Despite these general similarities, there are some minor variations. The stable region of the O3 phase at high Na content (x > 0.78) becomes narrow, while the P3- and O1-stable regions expand, compared with NCO. The expanded P3-stable region by the Ca substitution is consistent with the *ex situ* XRD results shown in Fig. 2-8b. The expanded O1-stable region indicates that the phase transition from O3 phase to O1 phase at high voltage is more favorable in NCCO than that in NCO. This contradicts the experimental results, which showed that the crystallinity of NCO deteriorated while NCCO retained good crystallinity at high voltage, as shown in Fig. 2-9. Therefore, the Ca substitution does not thermodynamically suppress the irreversible phase transition.
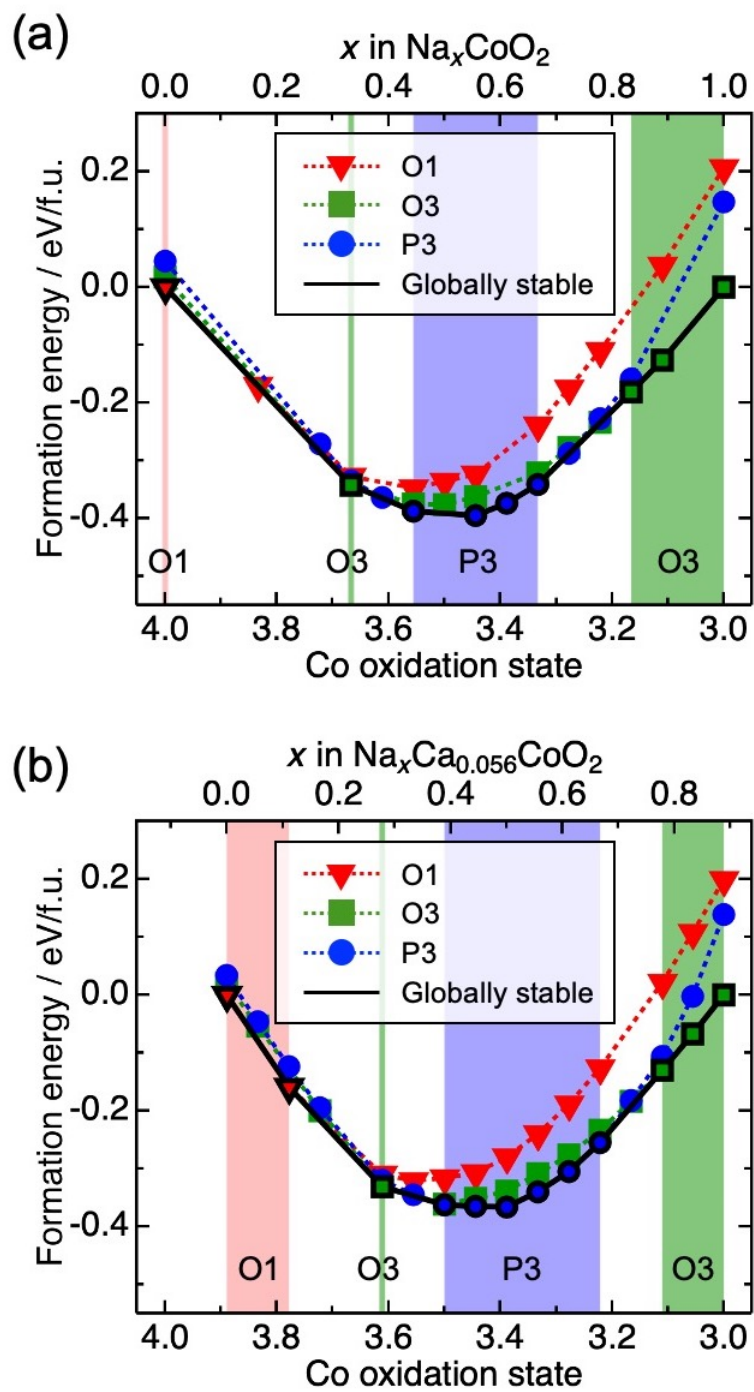
Figure 2-10 Convex hulls of **(a)** Na_xCoO_2 and **(b)** $Na_xCa_{0.056}CoO_2$.

In addition to studying the thermodynamic effect of the Ca substitution, the kinetics of the phase transition were also investigated by DFT calculation. Since the phase transition of the layered oxide is accompanied with the CoO_2 slab gliding, the activation energy of the gliding might be another important factor determining the phase stabilities. Figure 2-11 shows the estimated activation energies of the phase transition from O3 to O1 at the compositions of $Na_{0.333-y}Ca_yCoO_2$ ($y = 0$ or 0.056), which are the borders between the single O3 phase and O3-O1 two-phase region. The intermediate states were constructed by interpolating the structures between the O1- and O3-type structures. Note that only two endpoints (O3 and O1) were fully relaxed, while the intermediate states were calculated without any structural relaxation. Therefore, this calculation overestimates the actual activation energies; however, it enables a qualitative elucidation of the Ca-substitution effect. The activation energy of the O3-O1 phase transition for $Na_{0.278}Ca_{0.056}CoO_2$ is higher than that for $Na_{0.333}CoO_2$. This result suggests that the divalent Ca^{2+} ions in the Na layer hinder the gliding of CoO_2 slabs. Therefore, the improvement in the cycling performance of the Ca-substituted Na_xCoO_2 stems from the kinetically suppressed phase transition.

The rate constant of the phase transition can be derived from the activation energy using the following Arrhenius equation.

$$k = k_0 * exp\left(\frac{-E_a}{k_B T}\right) \tag{2-3}$$

where k_0 is the pre-exponential factor. E_a, k_B, and T represent the activation energy, the Boltzmann constant, and the temperature, respectively. Although k cannot be calculated since k_0 is unknown, the ratio of k for the NCO and NCCO can be derived, and k_{NCCO}/k_{NCO} at room temperature was calculated to be approximately 0.5. This result indicates that the Ca substitution doubles the time required for the phase transition. From this calculation, one can

conclude that the Ca substitution hardly has the kinetic effect of the phase transition since this difference is too small for the timescale of the charge/discharge process. However, E_a for the NCO and NCCO are not accurate since these values were calculated without the structural relaxation. Therefore, the calculated value of k_{NCCO}/k_{NCO} (≈ 0.5) is not accurate, and the correct k_{NCCO}/k_{NCO} might be much lower.

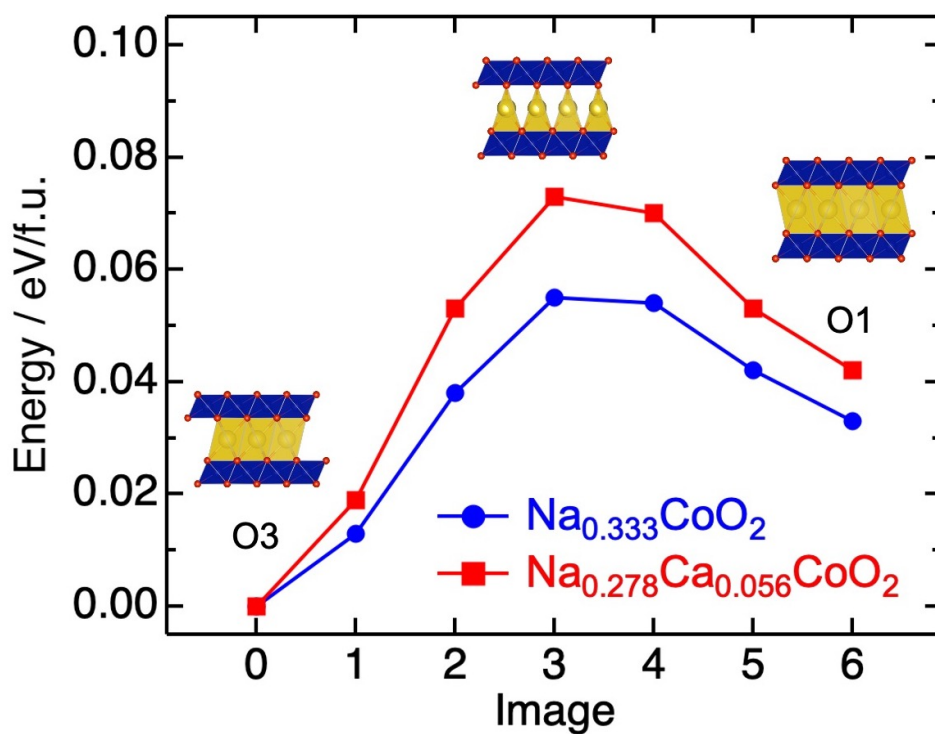**Figure 2-11** Estimated activation energies of the phase transition from O3 to O1. The compositions of the structures are $Na_{0.333-y}Ca_yCoO_2$ (y = 0 or 0.056). The X-axis represents each image (structure) during the phase transition.

2.3.4. Na-ion diffusivities in the layered oxides

In order to investigate the effect of Ca-substitution on the Na ion diffusivity, the migration energies of Na ions were calculated by the CI-NEB method [36-38]. Figure 2-12ab illustrate migration paths of the Na ions in P3-$Na_{0.333}CoO_2$ and P3-$Na_{0.278}Ca_{0.056}CoO_2$, respectively. The numbers adjacent to the paths correspond to path1, path2, and path3, respectively. Note that path1 and path2 are identical. Path3 is also fundamentally identical to path1 and path2, except that the Ca site is adjacent to the path instead of the Na ion. Figure 2-12c–e also show the migration paths from a different perspective.

Figure 2-13 displays the migration energy of each path, as well as that of a Ca^{2+}-ion hopping. The migration energies of the path1, path2, and path3 are 319, 253, and 500 meV, respectively. The migration energy of path1 in P3-$Na_{0.333}CoO_2$ (319 meV) is higher than that for O3-$NaCoO_2$ (190 meV) and P3-$NaTiO_2$ (220-250 meV) [40, 41]. This discrepancy is attributed to the different types of the structures (P3 and O3), the transition metals (Co and Ti) and the Na content ($x \approx 0.33$ and $x \approx 1$). The bottlenecks of these paths are located at around 60% of the path distance, where the hopping Na^+ ion passes by the adjacent alkali ion (Na^+ or Ca^{2+}).

The diffusion coefficients D were calculated from the migration energy E_a by using the Arrhenius equation below [42]:

$$D = a^2 \nu * exp\left(\frac{-E_a}{k_B T}\right) \tag{2-4}$$

where a is the hopping length, and ν is the attempt frequency. The diffusion coefficients D, calculated with $a = 1.5$ Å, $\nu = 10^{12}$ Hz, and $T = 298$ K, are shown in Table 2-2.

The path2 has the lowest migration barrier among the three paths. The low migration barrier is attributable to the expansion of the Na layer along the c-axis. The calculated O-O

bond lengths of the Na layer in $Na_{0.333}CoO_2$ and $Na_{0.278}Ca_{0.056}CoO_2$ are 3.580 Å and 3.597 Å, respectively, as shown in Table 2-3. Figure 2-14 illustrates the coordination environments of a Na^+ ion in the P3- and P2-type structure. The NaO_6 prism in the P3 structure has a face-sharing CoO_6 octahedron on one side and three edge-sharing CoO_6 octahedra on the other side, as shown in Fig. 2-14a. Once the Ca^{2+} ion occupies the Na site, the Na layer is expanded by the electrostatic repulsion between the divalent Ca^{2+} ion and the Co^{3+} ion at the face-sharing octahedron. Therefore, the Ca substitution decreases the migration barrier of the Na^+ ions by expanding the bottleneck of the migration.

A comparison with the Ca substitution in the P2-type layered structure is also helpful to understand the decreased migration energy of the path2 in the P3 phase. The P2-type structure has two distinct sites for the Na^+ ion: the $2b$ and $2d$ sites (Fig. 2-14b). The $2b$ site has two face-sharing CoO_6 octahedra, while the $2d$ site has six edge-sharing CoO_6 octahedra. Since the Ca^{2+} ion preferably occupies the $2d$ site, the lattice constant along the c-axis shrinks by the Ca substitution. Therefore, the Ca substitution in the P2 phase significantly increases the overpotential, as previously reported [22]. Moreover, the overpotential of the P3-type $Na_xCa_{0.04}CoO_2$ does not become higher than that of P3-Na_xCoO_2. This result suggests the Ca substitution in the P3 phase partially promotes the Na^+ diffusion rather than limiting the Na^+ diffusion paths.

For the P3 structure, the migration barrier of the path3 (500 meV) is much larger than that of path1 (319 meV) and path2 (253 meV), because the Ca^{2+} ion electrostatically repels the Na^+ ion hopping at the neighboring prismatic site. The diffusion coefficient for path3 is about 10^{-5} times smaller than that for path2 (Table 2-2). Therefore, most of the Na^+ ions preferably take the path2 to avoid the adjacent prismatic Ca^{2+} site.

As shown in Fig. 2-13, the migration barrier of the Ca^{2+} hopping is 509 meV. Since this value is too high for the Ca^{2+} ions to migrate, and the diffusion coefficient is estimated to be

5.5 × 10^{-13} cm^2 s^{-1}, as shown in Table 2-2. Thus, the Ca^{2+} ions are regarded as immobile. Interestingly, the barrier of the Ca^{2+} hopping is similar to that of path3. In both cases, the energies become the highest where the Na$^+$ ion and the Ca^{2+} ion get close to each other. Thus, the influence of the Na-Ca distance is dominant in the migration energies in the P3-type structures.
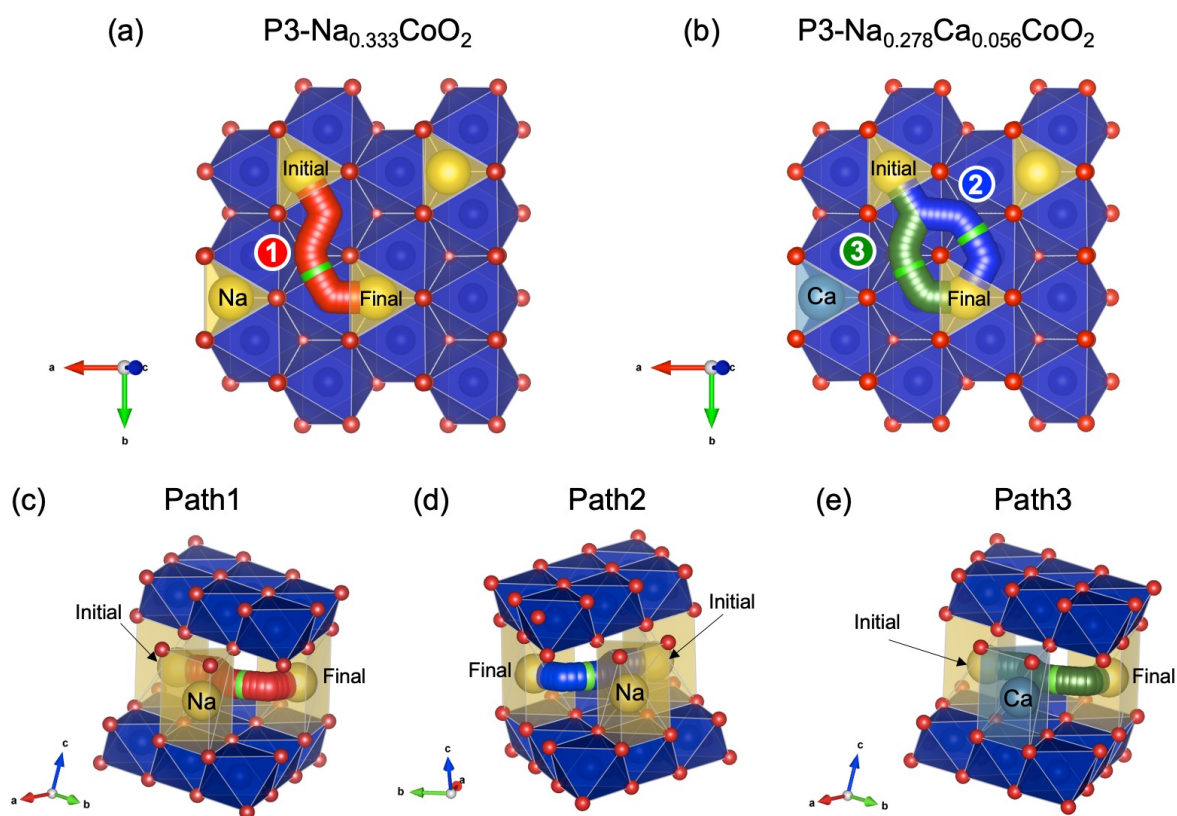

Figure 2-12 Migration paths of Na ions in **(a)** P3-Na$_{0.333}$CoO$_2$ and **(b)** P3-Na$_{0.278}$Ca$_{0.056}$CoO$_2$. The numbers adjacent to the paths represent path1, path2, and path3, respectively. Migration paths from the different perspectives of **(c)** path1, **(d)** path2, and **(e)** path3. Yellow prisms and a light blue prism represent the Na sites and the Ca site, respectively. The light green spheres represent the Na ions at the bottlenecks. Note that the monoclinic lattices are used here.
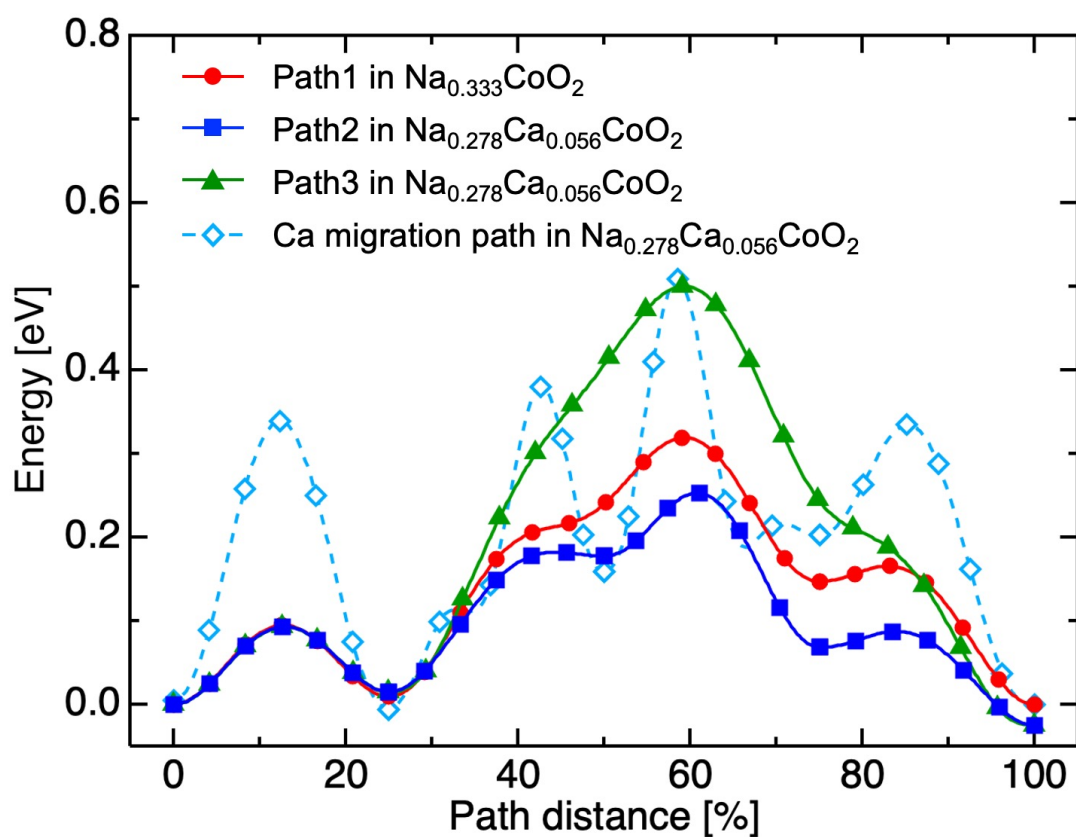
Figure 2-13 Migration barriers for Na ions along path1, path2, and path3. The migration barrier

for Ca ions is also shown.

Table 2-2 Diffusion coefficients of the Na and Ca ions.

Hopping ion	E_a / meV	D / cm^2 s^{-1}
Na in path1	319	9.1×10^{-10}
Na in path2	253	1.2×10^{-8}
Na in path3	500	7.9×10^{-13}
Ca	509	5.5×10^{-13}

Table 2-3 Average O-O bond length in the P3 and P2 structures.

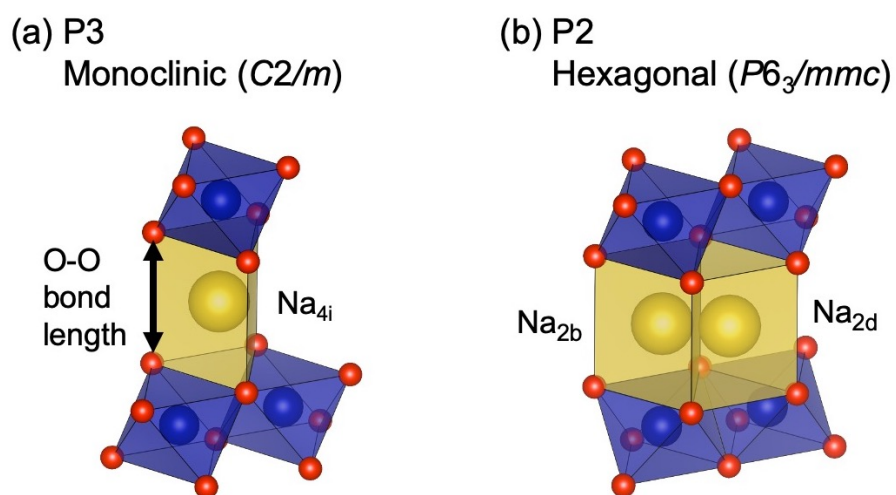|	Average O-O bond length of the Na layer / Å	
	$Na_{0.33}CoO_2$	$Na_{0.28}Ca_{0.056}CoO_2$
P3	3.580	3.597
P2	3.629	3.529

Figure 2-14 O-O bond length of the Na layer in the P3 and P2 structures. P3 and P2 structures are shown as a monoclinic ($C2/m$) and a hexagonal ($P6_3/mmc$) lattice, respectively.

2.4. Conclusion

In this chapter, the Ca-substitution effect on P3-type Na_xCoO_2 was investigated. The Ca-substituted Na_xCoO_2 was successfully synthesized by the solid-state method. From the electrochemical tests and the *ex situ* XRD measurements, it is found that the Ca substitution suppresses the irreversible phase transition at high voltage during the charging/discharging process, resulting in a significant improvement in the cycling performance compared with the Ca-free P3-Na_xCoO_2. The DFT calculations suggest that the Ca substitution in P3-Na_xCoO_2 expands the stable region of the Na^+-diffusive P3 phase, although the general trends in the phase stabilities are similar between the Ca-free Na_xCoO_2 and the Ca-substituted Na_xCoO_2. Also, the presence of Ca^{2+} ions in the Na layer kinetically hinders the phase transition from O3 to O1, accompanied by the gliding of CoO_2 slabs. The suppressed phase transition leads to the better crystallinity during the charge/discharge cycles. The NEB calculations further proved that the Ca substitution decreases the migration barrier of the Na^+ ions because the Ca^{2+} ions expand the bottleneck of the Na layers. It is also found that the Na^+ ions detour around the Ca^{2+} to avoid the strong electrostatic repulsion. The migration energy for the Ca^{2+} ions is large (509 meV), and thus the Ca^{2+} mobility in the Na^+ layer is negligible. In summary, the Ca substitution could be a practical materials design strategy for improving the structural stability and rate capability of Na-based cathode active materials.

References

[1]   C. Delmas, J. Braconnier, C. Fouassier, and P. Hagenmuller, *Solid State Ionics*, **3–4** (1981) 165–169.

[2]   M. H. Han, E. Gonzalo, G. Singh, and T. Rojo, *Energy Environ. Sci.*, **8** (2015) 81–102.

[3]   J.-J. Braconnier, C. Delmas, C. Fouassier, and P. Hagenmuller, *Mater. Res. Bull.*, **15** (1980) 1797–1804.

[4]   A. Maazaz, C. Delmas, and P. Hagenmuller, *J. Inclusion Phenom.*, **1** (1983) 45–51.

[5]   X. Xia and J. R. Dahn, *Electrochem. Solid-State Lett.*, **15** (2012) A1–A4.

[6]   X. Xia and J. R. Dahn, *J. Electrochem. Soc.*, **159** (2012) A647–A650.

[7]   D. Hamani, M. Ati, J.-M. Tarascon, and P. Rozier, *Electrochem. Commun.*, **13** (2011) 938–941.

[8]   N. Yabuuchi, H. Yoshida, and S. Komaba, *Electrochemistry*, **80** (2012) 716–719.

[9]   A. Mendiboure, C. Delmas, and P. Hagenmuller, *J. Solid State Chem.*, **57** (1985) 323–331.

[10]   C. Delmas, C. Fouassier, and P. Hagenmuller, *Physica B+C*, **99** (1980) 81–85.

[11]   M. D. Radin, J. Alvarado, Y. S. Meng, and A. Van der Ven, *Nano Lett.*, **17** (2017) 7789–7795.

[12]   X. Ma, H. Chen, and G. Ceder, *J. Electrochem. Soc.*, **158** (2011) A1307–A1312.

[13]   I. Saadoune, A. Maazaz, M. Ménétrier, and C. Delmas, *J. Solid State Chem.*, **122** (1996) 111–117.

[14]   Z. Lu, R. A. Donaberger, and J. R. Dahn, *Chem. Mater.*, **12** (2000) 3583–3590.

[15]   S. Komaba, N. Yabuuchi, T. Nakayama, A. Ogata, T. Ishikawa, and I. Nakai, *lnorg. Chem.*, **51** (2012) 6211–6220.

[16] X. Li, D. Wu, Y.-N. Zhou, L. Liu, X.-Q. Yang, and G. Ceder, *Electrochem. Commun.*, **49** (2014) 51–54.

[17] K. Kubota, T. Asari, H. Yoshida, N. Yabuuchi, H. Shiiba, M. Nakayama, and S. Komaba, *Adv. Funct. Mater.*, **26** (2016) 6047–6059.

[18] P.-F. Wang, Y. You, Y.-X. Yin, Y.-S. Wang, L.-J. Wan, L. Gu, and Y.-G. Guo, *Angew. Chem. Int. Ed.*, **55** (2016) 7445–7449.

[19] S. C. Han, H. Lim, J. Jeong, D. Ahn, W. B. Park, K.-S. Sohn, and M. Pyo, *J. Power Sources*, **277** (2015) 9–16.

[20] L. Sun, Y. Xie, X.-Z. Liao, H. Wang, G. Tan, Z. Chen, Y. Ren, J. Gim, W. Tang, Y.-S. He, K. Amine, and Z.-F. Ma, *Small*, **14** (2018) 1704523.

[21] L. Zheng, J. C. Bennett, and M. N. Obrovac, *J. Electrochem. Soc.*, **166** (2019) A2058–A2064.

[22] M. Matsui, F. Mizukoshi, and N. Imanishi, *J. Power Sources*, **280** (2015) 205–209.

[23] K. Momma and F. Izumi, *J. Appl. Crystallogr.*, **44** (2011) 1272–1276.

[24] F. Izumi and K. Momma, *Solid State Phenom.*, **130** (2007) 15–20.

[25] P. E. Blöchl, *Phys. Rev. B*, **50** (1994) 17953–17979.

[26] G. Kresse and D. Joubert, *Phys. Rev. B*, **59** (1999) 1758–1775.

[27] G. Kresse and J. Furthmüller, *Comput. Mater. Sci.*, **6** (1996) 15–50.

[28] G. Kresse and J. Furthmüller, *Phys. Rev. B*, **54** (1996) 11169–11186.

[29] J. Klimeš, D. R. Bowler, and A. Michaelides, *Phys. Rev. B*, **83** (2011) 195131.

[30] J. Klimeš, D. R. Bowler, and A. Michaelides, *J. Phys.: Condens. Matter*, **22** (2010) 022201.

[31] M. Aykol, S. Kim, and C. Wolverton, *J. Phys. Chem. C*, **119** (2015) 19053–19058.

[32] J. L. Kaufman and A. Van der Ven, *Phys. Rev. Mater.*, **3** (2019) 015402.

[33] Y. Hinuma, Y. S. Meng, and G. Ceder, *Phys. Rev. B*, **77** (2008) 224111.

[34]   S. P. Ong, W. D. Richards, A. Jain, G. Hautier, M. Kocher, S. Cholia, D. Gunter, V. L. Chevrier, K. A. Persson, and G. Ceder, *Comput. Mater. Sci.*, **68** (2013) 314–319.

[35]   K. Okhotnikov, T. Charpentier, and S. Cadars, *J. Cheminform.*, **8** (2016) 17.

[36]   G. Henkelman and H. Jónsson, *J. Chem. Phys.*, **113** (2000) 9978–9985.

[37]   G. Henkelman, B. P. Uberuaga, and H. Jónsson, *J. Chem. Phys.*, **113** (2000) 9901–9904.

[38]   D. Sheppard, P. Xiao, W. Chemelewski, D. D. Johnson, and G. Henkelman, *J. Chem. Phys.*, **136** (2012) 074103.

[39]   Y. Lei, X. Li, L. Liu, and G. Ceder, *Chem. Mater.*, **26** (2014) 5288–5296.

[40]   S. P. Ong, V. L. Chevrier, G. Hautier, A. Jain, C. Moore, S. Kim, X. Ma, and G. Ceder, *Energy Environ. Sci.*, **4** (2011) 3680–3688.

[41]   S. Guo, Y. Sun, J. Yi, K. Zhu, P. Liu, Y. Zhu, G.-Z. Zhu, M. Chen, M. Ishida, and H. Zhou, *NPG Asia Mater.*, **8** (2016) e266.

[42]   D. Morgan, A. Van der Ven, and G. Ceder, *Electrochem. Solid-State Lett.*, **7** (2004) A30–A32.

Chapter 3

Exploring Factors Limiting Three-Na$^+$ Extraction from Na$_3$V$_2$(PO$_4$)$_3$

3.1. Introduction

Various compounds, such as layered transition-metal oxides [1], pyrite-type transition-metal sulfides [2], alluaudite-type sulphates [3], NASICON-type sulphates [4], NASICON-type phosphates [5], pyrophosphates [6], fluorophosphates [7, 8], perovskite-type fluorides [9], and organic compounds [10], have been extensively studied as possible cathode materials for NIBs. Among them, Na$_3$V$_2$(PO$_4$)$_3$ is one of the promising cathode materials due to its high energy density ($\sim$ 400 Wh g^{-1}), low overpotential, rate capability, and good cyclability [5, 11]. This material has a NASICON (NA-Super-Ionic-CONductor) structure [12], as shown in Fig. 3-1a. In the NASICON structure, there are two Na sites, namely, Na1 and Na2. The Na1 site is located in a distorted octahedron, and the Na2 site is located in an eight-fold coordinated polyhedron (Fig. 3-1bc). Na$_3$V$_2$(PO$_4$)$_3$ exhibits a voltage plateau of V^{3+}/V^{4+} redox at 3.4 V vs. Na$^+$/Na^0 with a capacity of 118 mAh g^{-1}, which corresponds to the theoretical capacity of two-Na$^+$ extraction/insertion per formula unit [5, 11]. Na$_3$V$_2$(PO$_4$)$_3$ also exhibits additional two-Na$^+$ insertion with a V^{2+}/V^{3+} redox reaction, resulting in Na$_5$V$_2$(PO$_4$)$_3$ [13]. Since the voltage of

V^{2+}/V^{3+} redox is too low (≤ 1.6 V), only the two-Na$^+$ extraction/insertion reaction between Na$_3$V$_2$(PO$_4$)$_3$ and NaV$_2$(PO$_4$)$_3$ can be utilized as a cathode.

In order to increase the energy density, it is desirable to extract more Na ions from Na$_3$V$_2$(PO$_4$)$_3$. Previously, Gopalakrishnan *et al*. reported a full Na$^+$ extraction from Na$_3$V$_2$(PO$_4$)$_3$ by chemical oxidation [14]. Moreover, Yan *et al*. recently demonstrated an electrochemical full Na$^+$ extraction from Na$_3$V$_2$(PO$_4$)$_2$F$_3$ [15]. To the best of our knowledge, however, electrochemical three-Na$^+$ extraction from Na$_3$V$_2$(PO$_4$)$_3$ has not been achieved, even though three-Li$^+$ extraction has been achieved from Li$_3$V$_2$(PO$_4$)$_3$ [16], which is a counterpart of Na$_3$V$_2$(PO$_4$)$_3$. Because of the difficulty of the three-Na$^+$ extraction, alternative strategies have been employed to increase the energy density. One approach is to utilize V^{3+}/V^{4+} redox and V^{4+}/V^{5+} redox by substituting other trivalent elements for vanadium. For example, multi-redox reactions of V^{3+}/V^{4+}/V^{5+} were reported in previous studies of Na$_3$V$_{2-x}$Al$_x$(PO$_4$)$_3$ [17, 18] and Na$_3$V$_{2-x}$Cr$_x$(PO$_4$)$_3$ [19, 20]. In addition to the activation of V^{4+}/V^{5+} redox, another strategy is to increase the initial Na$^+$ amount by substituting divalent elements for vanadium (e.g., Na$_{3+x}$V$_{2-x}$Mg$_x$(PO$_4$)$_3$ [21], Na$_{3+x}$V$_{2-x}$Fe$_x$(PO$_4$)$_3$ [22], and Na$_4$VMn(PO$_4$)$_3$ [23]). While the energy densities were improved in those materials, the last Na$^+$ in the formula units still remained in the NASICON structures at the charged states.

In Na$_3$V$_2$(PO$_4$)$_3$, two Na$^+$ were extracted from the Na2 site during the charge reaction at 3.4 V, and the third Na$^+$ remaining in NaV$_2$(PO$_4$)$_3$ occupied the Na1 site, as reported by Jian *et al*. and Lim *et al*. [24, 25]. The voltage of the third-Na$^+$ extraction was predicted to be 4.64 V from the DFT calculations [25]. This voltage step from 3.4 V to 4.64 V originates from two factors. The first factor is the shift of the redox couples from V^{3+}/V^{4+} to V^{4+}/V^{5+}, and the second is the Na$^+$ extraction from the Na1 site. Due to the overlap of the two contributions, it is difficult to point out the source of the limitation of the three-Na$^+$ extraction. Partial substitution of

electrochemically inactive elements for vanadium is an effective method to decouple the two contributions, as previously reported for $Na_3V_2(PO_4)_2F_3$ [26].

In this chapter, factors which limit the three-Na^+ extraction from $Na_3V_2(PO_4)_3$ are experimentally and computationally investigated. $Na_3V_{1.5}Al_{0.5}(PO_4)_3$ was also studied in order to decouple the two contributions to the voltage step. The third-Na^+ extractions were not observed in the electrochemical tests, and the DFT calculations predicted that a high voltage of more than 4.5 V is required to extract Na^+ from the Na1 site. Moreover, Na^+ is locked up in the Na1 site in $NaV_2(PO_4)_3$ due to the significant migration energy. The difference in voltage and alkali-ion diffusivities between $Na_3V_2(PO_4)_3$ and $Li_3V_2(PO_4)_3$ is also discussed.
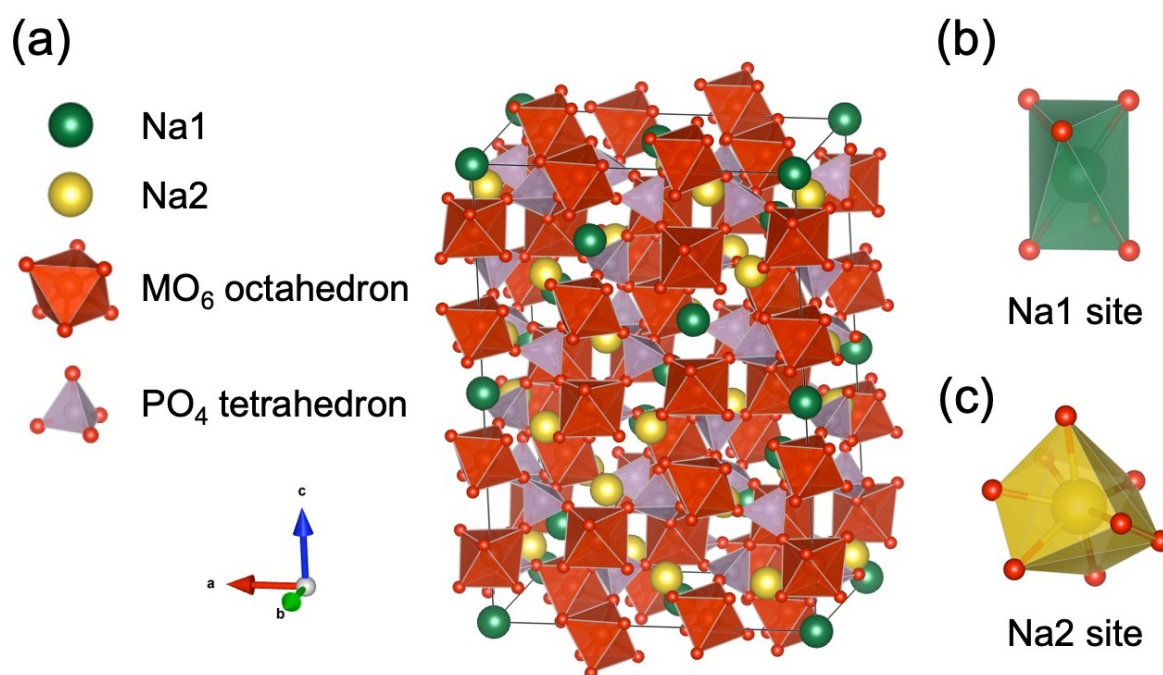
Figure 3-1 (a) Crystal structure of NASICON-type $Na_3V_2(PO_4)_3$ (*C2/c*) and local environments of the **(b)** Na1 site and **(c)** Na2 site. The structure was visualized using VESTA [27].

3.2. Experimental

3.2.1. Materials synthesis and characterization

Carbon-coated $Na_3V_2(PO_4)_3$ and $Na_3V_{1.5}Al_{0.5}(PO_4)_3$ were synthesized by a sol-gel method. Stoichiometric NaH_2PO_4 ($\geq$ 99.0%; Fujifilm Wako Pure Chemical Corporation) and NH_4VO_3 ($\geq$ 99.0%; Fujifilm Wako Pure Chemical Corporation) were added to ultrapure water (18.2 MΩ cm) purified with Direct-Q UV3 (Merck). For $Na_3V_{1.5}Al_{0.5}(PO_4)_3$, stoichiometric $Al(NO_3)_3 \cdot 9H_2O$ ($\geq$ 98.0%; Kanto Chemical Co.) was also added. Then, citric acid ($\geq$ 98.0%; Fujifilm Wako Pure Chemical Corporation) as a carbon source was dissolved into the water. The molar ratio of citric acid to the metal ions (V and Al) was 3:2. The solution was dried at 120 ºC. The dried precursors were ground and pelletized, then heated at 500 ºC under an Ar-H_2 (95:5 vol.%) gas flow for 2 hours. The samples were ground and pelletized again, then heated at 750 ºC under an Ar-H_2 (95:5 vol.%) gas flow for 12 hours. The final products were obtained by grinding the samples after the calcination.

XRD measurements were performed using a MiniFlex X-ray diffractometer (Rigaku) with Cu-Kα radiation. Rietveld refinements were carried out with RIETAN-FP [28]. The thermogravimetric (TG) analysis was performed with a Thermo plus TG8110 system (Rigaku) in order to determine the carbon contents in the samples.

3.2.2. Electrochemical tests

The $Na_3V_2(PO_4)_3$ and $Na_3V_{1.5}Al_{0.5}(PO_4)_3$ electrodes were prepared by coating slurries made of 80 wt.% of the active material, 10 wt.% of AB (Denka Co.) and 10 wt.% of PVDF (Kureha Corporation) in NMP (Fujifilm Wako Pure Chemical Corporation) on Al foils. The slurries on the Al foils were dried in a vacuum at 80 °C. The typical loading mass of the active materials

was 1.3 mg cm^{-2}. 2032 coin-type cells were fabricated in an Ar-filled glove box using the prepared positive electrodes, Na metal (99.9%; Sigma-Aldrich) as a negative electrode, 1 M NaPF$_6$ in EC:DMC (1:1 in vol.%) as an electrolyte, and a GA-55 glass fiber filter (Advantec) as a separator. Electrochemical tests were performed using a BTS-2004H battery testing system (NAGANO).

3.2.3. Computational methods

DFT calculations were performed with the VASP [29, 30]. The PAW method was used [31, 32], and the plane-wave cutoff energy was set to 520 eV. The PBE exchange-correlation functional was adopted [33]. The Hubbard U value for vanadium was set to 5.0 eV [34], which was used for AVPO$_4$F (A = Li, Na, K) in a previous work [35]. For all DFT calculations, the Pymatgen package was used to generate input files and analyze the results [36].

The crystal structures of Na$_x$V$_2$(PO$_4$)$_3$ and Na$_x$V$_{1.5}$Al$_{0.5}$(PO$_4$)$_3$ were constructed from a unit cell ($C2/c$) reported by Chotard $et\ al.$ [37], and a Γ-centered 1 × 2 × 1 k-point mesh was used. All Na-vacancy orderings and V-Al orderings in the unit cells were enumerated by the Supercell program [38]. For each composition, the 30 structures with the lowest electrostatic energies were subject to the DFT calculations, and the most stable configuration was determined.

For Li$_x$V$_2$(PO$_4$)$_3$, the crystal structures were constructed from monoclinic-Li$_3$V$_2$(PO$_4$)$_3$ ($P2_1/n$, ICSD No. 96962), and a gamma-centered 3 × 3 × 2 k-point mesh was used. Li-vacancy orderings were selected following previous reports [39, 40].

The average voltage between two phases was obtained using the following equation [41]:

$$V = -\frac{E\big(A_{x_1}M_2(PO_4)_3\big) - E\big(A_{x_2}M_2(PO_4)_3\big) - (x_1 - x_2)E\big(A\big)}{(x_1 - x_2)F} \tag{3-1}$$

where $E(A_{x1}M_2(PO_4)_3)$, $E(A_{x2}M_2(PO_4)_3)$, and $E(A)$ are DFT energies of $A_{x1}M_2(PO_4)_3$, $A_{x2}M_2(PO_4)_3$ and alkali metal (A = Na or Li), respectively. M in the chemical formula denotes V and Al.

To investigate the migration barriers of alkali ions, NEB calculations were carried out using the VTST tools [42, 43]. The force was converged within 0.05 eV Å^{-1}.

AIMD simulations were also performed in the canonical (NVT) ensemble using VASP. The time step was set to 2.0 fs, and the simulations were run for 40 ps at 1000 K using the Nosé-Hoover thermostat [44, 45]. In order to reduce the computational cost, the plane-wave cutoff energy was set to 400 eV, and a single Γ point was used as a k-point mesh. Moreover, for $Na_xV_2(PO_4)_3$, a smaller unit cell (6 formula units) obtained from the Materials Project [46] (mp-776557) was used instead of the original unit cell (12 formula units) to reduce the computational cost.

3.3. Results and Discussion

3.3.1. Materials characterization

Figure 3-2 shows the results of the Rietveld refinements of as-prepared $Na_3V_2(PO_4)_3$ and $Na_3V_{1.5}Al_{0.5}(PO_4)_3$. The refined crystallographic data are shown in Table 3-1 and Table 3-2. In both $Na_3V_2(PO_4)_3$ and $Na_3V_{1.5}Al_{0.5}(PO_4)_3$, all the diffraction peaks were indexed to a monoclinic lattice ($C2/c$), and no impurity phase was observed. While the structures of $Na_3V_2(PO_4)_3$ have been characterized as rhombohedral ($R\text{-}3c$) in many studies [11, 24, 25], Chotard et al. reported that $Na_3V_2(PO_4)_3$ forms a monoclinic structure ($C2/c$) below room temperature [37]. The Rietveld refinements were performed with both the monoclinic lattice and the rhombohedral lattice, and the former showed a better fitting. In the rhombohedral structure, only a Na1 site and a Na2 site were present. On the other hand, in the monoclinic structure, the Na1 site split into two distinct sites, namely Na1a and Na1b. The Na2 site also split into several sites (Na2a, Na2b, Na2c, Na2d, and Na2e). These changes arose from the lower symmetry of the monoclinic structure. Since these split sites were essentially the same as the original sites, they are referred to as the Na1 site or Na2 site in this study unless otherwise specified.

The lattice constants of $Na_3V_2(PO_4)_3$ were a = 15.1189(4) Å, b = 8.7302(3) Å, c = 21.8378(8) Å, α = γ = 90°, and β = 90.123(3)°, respectively. The lattice constants of $Na_3V_{1.5}Al_{0.5}(PO_4)_3$ were a = 15.0606(4) Å, b = 8.6609(2) Å, c = 21.6551(4) Å, α = γ = 90°, and β = 90.072(6)°, respectively. $Na_3V_{1.5}Al_{0.5}(PO_4)_3$ has smaller lattice constants (a, b and c) compared with $Na_3V_2(PO_4)_3$ because the ionic radius of Al^{3+} (0.535 Å) is smaller than that of V^{3+} (0.64 Å).

In Table 3-2, the occupancy of the Na2d site in $Na_3V_{1.5}Al_{0.5}(PO_4)_3$ significantly decreased compared with $Na_3V_2(PO_4)_3$, while that of the other Na sites slightly increased. This was due to the partial stabilization of the Na ordering by the Al substitution. At -10^oC, $Na_3V_2(PO_4)_3$ has the Na ordering, where the Na2d and Na2e sites are completely vacant, and the other Na sites are fully occupied [37]. While the Na ordering disappears at room temperature for $Na_3V_2(PO_4)_3$, $Na_3V_{1.5}Al_{0.5}(PO_4)_3$ partially retains the Na ordering even at room temperature, as evidenced by the presence of the superstructure peak at 12.5^o in the XRD pattern in Fig. 3-2b [17, 18].

As shown in Fig. 3-3, TG analysis revealed that the carbon contents of $Na_3V_2(PO_4)_3$ and $Na_3V_{1.5}Al_{0.5}(PO_4)_3$ were 7.89% and 6.13%, respectively.
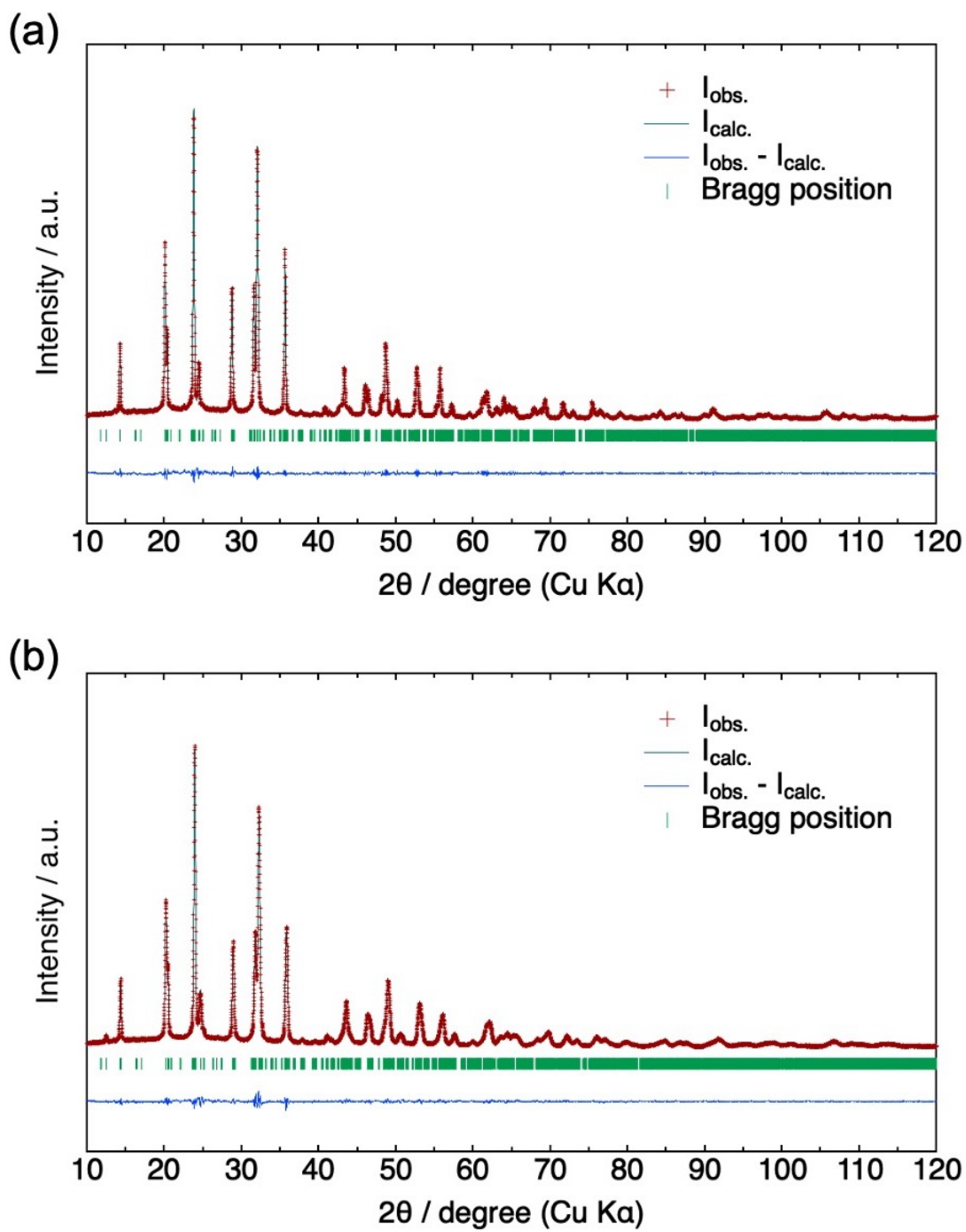
Figure 3-2 Rietveld refinements of XRD patterns of as-prepared **(a)** $Na_3V_2(PO_4)_3$ and **(b)** $Na_3V_{1.5}Al_{0.5}(PO_4)_3$.

Table 3-1 Refined crystallographic data for $Na_3V_2(PO_4)_3$ at room temperature.

Space group	a [Å]	b [Å]	c [Å]	α [°]	β [°]	γ [°]
$C2/c$	15.1189(4)	8.7302(3)	21.8378(8)	90	90.123(3)	90

R_{wp} [%]	R_e [%]	R_{wp}/R_e	R_B [%]	R_F [%]
4.87	4.45	1.09	0.93	0.22

Atom	Wyckoff site	Occupancy	x	y	z
Na1a	4a	0.8986	0	0	0
Na1b	8f	0.9420	0.3365(21)	0.0386(24)	0.1564(15)
Na2a	8f	0.8997	0.1771(9)	0.1959(21)	0.2599(6)
Na2b	8f	0.6861	0.0130(7)	0.3011(21)	0.4229(6)
Na2c	8f	0.6595	0.1577(19)	0.1625(19)	0.5892(16)
Na2d	4e	0.9055	0	0.3763(36)	0.75
Na2e	8f	0.5214	0.8648(11)	0.8165(29)	0.1050(5)
V1	8f	1	0.0011(4)	-0.0005(11)	0.3533(3)
V2	8f	1	0.3304(3)	-0.0042(10)	0.3155(3)
V3	8f	1	0.3317(4)	0.0076(8)	0.0200(4)
P1	8f	1	0.1873(5)	0.1590(17)	0.4181(5)
P2	4e	1	0	0.2835(21)	0.25
P3	8f	1	0.3541(6)	0.3557(15)	0.2516(3)
P4	8f	1	0.5198(7)	0.1473(17)	0.0809(4)
P5	8f	1	0.1690(5)	0.2053(13)	0.0836(6)
O1	8f	1	0.2714(13)	0.4308(29)	0.2448(9)
O2	8f	1	0.2459(14)	0.0962(21)	0.0851(9)
O3	8f	1	0.0887(9)	0.4159(16)	0.2472(7)
O4	8f	1	0.3387(16)	0.1834(20)	0.2622(11)
O5	8f	1	0.4332(15)	0.0503(22)	0.0793(10)
O6	8f	1	0.0853(11)	0.1084(20)	0.0908(7)
O7	8f	1	0.0980(13)	0.0545(16)	0.4055(11)
O8	8f	1	0.5143(8)	0.3097(25)	0.0813(12)
O9	8f	1	0.1749(19)	0.3119(26)	0.4179(14)
O10	8f	1	0.2460(12)	0.1382(28)	0.3604(11)
O11	8f	1	0.5744(9)	0.1286(23)	0.0154(6)
O12	8f	1	0.4041(16)	0.3837(30)	0.2014(7)
O13	8f	1	0.0232(10)	0.2313(25)	0.3037(13)
O14	8f	1	0.1532(11)	0.2917(25)	0.0290(13)
O15	8f	1	0.1863(14)	0.2929(25)	0.1440(14)
O16	8f	1	0.4101(9)	0.4246(17)	0.3068(5)
O17	8f	1	0.2233(11)	0.0675(27)	0.4589(6)
O18	8f	1	0.4355(13)	0.0816(27)	0.3621(11)

Table 3-2 Refined crystallographic data for $Na_3V_{1.5}Al_{0.5}(PO_4)_3$ at room temperature.

Space group	a [Å]	b [Å]	c [Å]	α [°]	β [°]	γ [°]
$C2/c$	15.0606(4)	8.6609(2)	21.6551(4)	90	90.072(6)	90

R_{wp} [%]	R_e [%]	R_{wp}/R_e	R_B [%]	R_F [%]
4.36	4.29	1.02	0.61	0.24

| Atom	Wyckoff site	Occupancy	x	y	z
Na1a	4a	0.953	0	0	0
Na1b	8f	0.9805	0.3694(7)	0.0109(20)	0.1562(6)
Na2a	8f	0.7041	0.1815(13)	0.1915(27)	0.2504(14)
Na2b	8f	0.7367	0.0119(11)	0.3121(19)	0.4158(11)
Na2c	8f	0.8987	0.1642(12)	0.1318(16)	0.5737(6)
Na2d	4e	0.4635	0	0.3479(35)	0.75
Na2e	8f	0.5219	0.8368(16)	0.8030(20)	0.0794(13)
V1	8f	0.75	0.0024(5)	0.0007(8)	0.3528(3)
V2	8f	0.75	0.3279(5)	-0.0061(8)	0.3130(4)
V3	8f	0.75	0.3319(5)	0.0129(9)	0.0213(4)
Al1	8f	0.25	0.0024(5)	0.0007(8)	0.3528(3)
Al2	8f	0.25	0.3279(5)	-0.0061(8)	0.3130(4)
Al3	8f	0.25	0.3319(5)	0.0129(9)	0.0213(4)
P1	8f	1	0.1829(7)	0.1353(14)	0.4200(7)
P2	4e	1	0	0.3154(14)	0.25
P3	8f	1	0.3490(8)	0.3665(10)	0.2493(4)
P4	8f	1	0.5281(5)	0.1460(8)	0.0843(5)
P5	8f	1	0.1646(10)	0.2104(9)	0.0841(5)
O1	8f	1	0.2611(17)	0.4224(24)	0.2497(12)
O2	8f	1	0.2554(15)	0.1083(24)	0.0762(10)
O3	8f	1	0.0908(16)	0.3825(22)	0.2518(10)
O4	8f	1	0.3435(12)	0.1802(16)	0.2504(9)
O5	8f	1	0.4316(12)	0.0702(24)	0.0749(9)
O6	8f	1	0.0848(14)	0.1076(22)	0.0899(11)
O7	8f	1	0.0951(14)	0.0768(27)	0.4099(10)
O8	8f	1	0.4963(15)	0.3274(22)	0.0878(13)
O9	8f	1	0.1780(14)	0.3215(19)	0.4209(13)
O10	8f	1	0.2455(12)	0.1339(16)	0.3614(8)
O11	8f	1	0.5708(11)	0.1485(32)	0.0132(8)
O12	8f	1	0.4071(16)	0.4021(20)	0.1938(13)
O13	8f	1	0.0114(13)	0.1973(23)	0.3122(12)
O14	8f	1	0.1488(18)	0.3193(20)	0.0336(9)
O15	8f	1	0.1852(14)	0.3110(26)	0.1452(15)
O16	8f	1	0.4012(14)	0.4309(28)	0.3049(8)
O17	8f	1	0.2341(13)	0.0797(24)	0.4748(13)
O18	8f	1	0.4193(15)	0.0751(21)	0.3608(12)
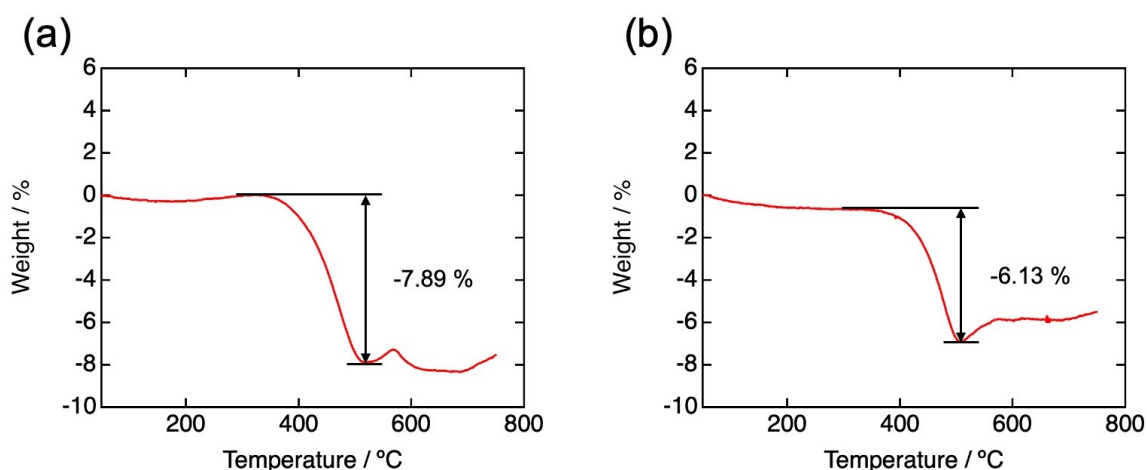
Figure 3-3 TG curves of **(a)** $Na_3V_2(PO_4)_3$ and **(b)** $Na_3V_{1.5}Al_{0.5}(PO_4)_3$ in air.

3.3.2. Voltage profiles of $Na_3V_2(PO_4)_3$ and $Na_3V_{1.5}Al_{0.5}(PO_4)_3$

The voltage profiles of $Na_3V_2(PO_4)_3$ and $Na_3V_{1.5}Al_{0.5}(PO_4)_3$ in the voltage range of 2.5 – 4.2V at 0.1C are shown in Fig. 3-4. At the top of each figure, the redox couples corresponding to the range of x in $Na_{3-x}M_2(PO_4)_3$ (M = V and Al) are shown. The specific capacities were calculated based on only the weight of the active materials. For both $Na_3V_2(PO_4)_3$ and $Na_3V_{1.5}Al_{0.5}(PO_4)_3$, the obtained capacities almost correspond to two-Na^+ extraction/insertion. These results are in good agreement with the previous studies [5, 17, 25].

Figure 3-5 shows the calculated and experimental voltage profiles of $Na_3V_2(PO_4)_3$ and $Na_3V_{1.5}Al_{0.5}(PO_4)_3$. The experimental charge/discharge curves were measured in the voltage range of 2.5 V – 4.7 V at 0.1C. In Fig. 3-5a, the experimental charge curve of $Na_3V_2(PO_4)_3$ exhibits a plateau of V^{3+}/V^{4+} redox at 3.4 V vs. Na^+/Na^0 in the range of $0 \leq x \leq 2$. This plateau corresponds to a two-phase reaction between $Na_3V_2(PO_4)_3$ and $NaV_2(PO_4)_3$ [47]. Although a large charge capacity (218 mAh g^{-1}) was obtained, no voltage slope or plateau of V^{4+}/V^{5+} redox was observed in the discharge curve, except for the plateau at 3.4 V. Therefore, the extended

charge capacity is attributed to an oxidative decomposition of the organic electrolyte at the high voltage, and the third Na^+ was not extracted during charging. Note that the third-Na^+ extraction was not observed even when the cutoff voltage was increased to 4.9 V, as shown in Fig. 3-6a. *Ex situ* XRD measurements during the charging process were also performed, as shown in Fig. 3-7a. The active material exhibited a phase transition from $Na_3V_2(PO_4)_3$ to $NaV_2(PO_4)_3$ during the charging to 3.8 V. However, there was no significant change in the XRD patterns at 3.8 V and 4.9 V, indicating the active material remained $NaV_2(PO_4)_3$ even at 4.9 V.

From the DFT calculations, the voltage in $0 \leq x \leq 2$ is predicted to be 3.38 V, which is in good agreement with the experimental value (Fig. 3-5). In the DFT calculations, the Na^+ is extracted from the Na2 site in $0 \leq x \leq 2$ and all the Na^+ ions occupy the Na1 site at $x = 2$. This result is consistent with the previous literature [24, 25]. A large voltage step from 3.38 V to 4.70 V is observed at $x = 2$. This voltage step is due to two contributions, namely the shift of the redox couples from V^{3+}/V^{4+} to V^{4+}/V^{5+} and the Na^+ extraction from the Na1 site. Other minor voltage steps are also observed at $x = 2.67$ and $x = 2.83$, respectively. They might be attributed to the change of the Na^+ ordering in the NASICON structure. Overall, the voltage for the third-Na^+ extraction from the Na1 site ($2 \leq x \leq 3$) is predicted to be more than 4.70 V, which is above the potential windows of the common organic electrolytes. Therefore, the electrolyte decompositions occur before the third-Na^+ extraction, as observed in the experiments.
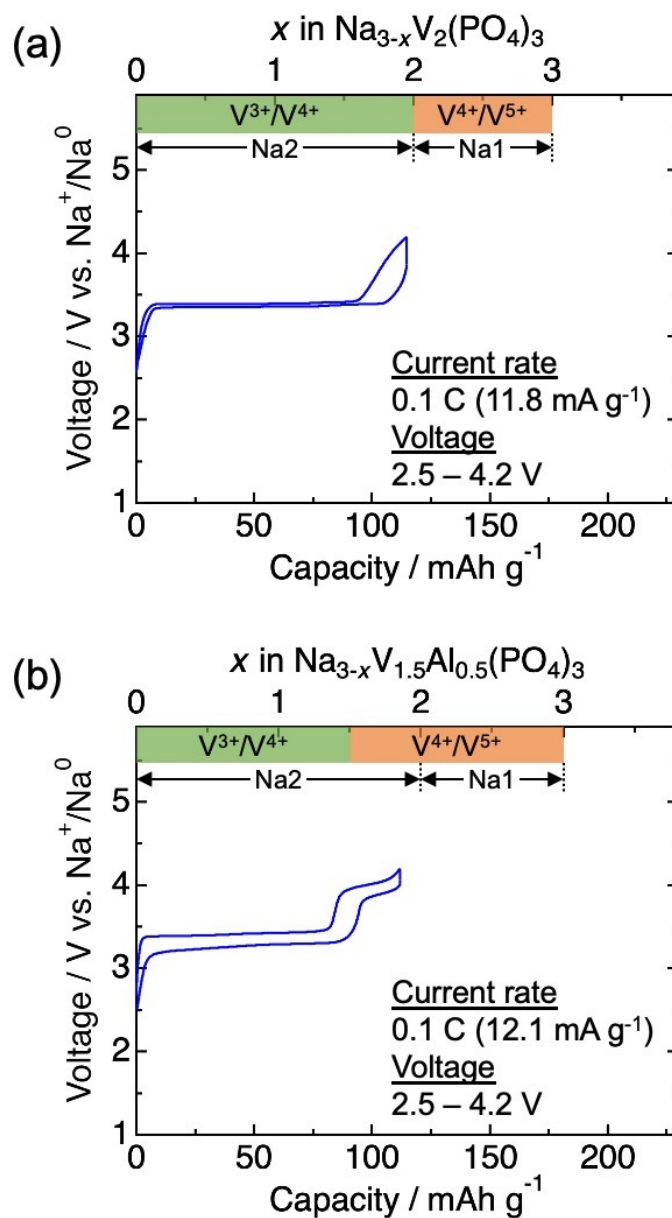
Figure 3-4 Voltage profiles of **(a)** $Na_3V_2(PO_4)_3$ and **(b)** $Na_3V_{1.5}Al_{0.5}(PO_4)_3$ in the voltage range

of 2.5–4.2 V. Redox couples corresponding to the range of x in $Na_{3-x}M_2(PO_4)_3$ (M = V and Al)

and the Na^+ extraction sites are shown at the top of each plot.
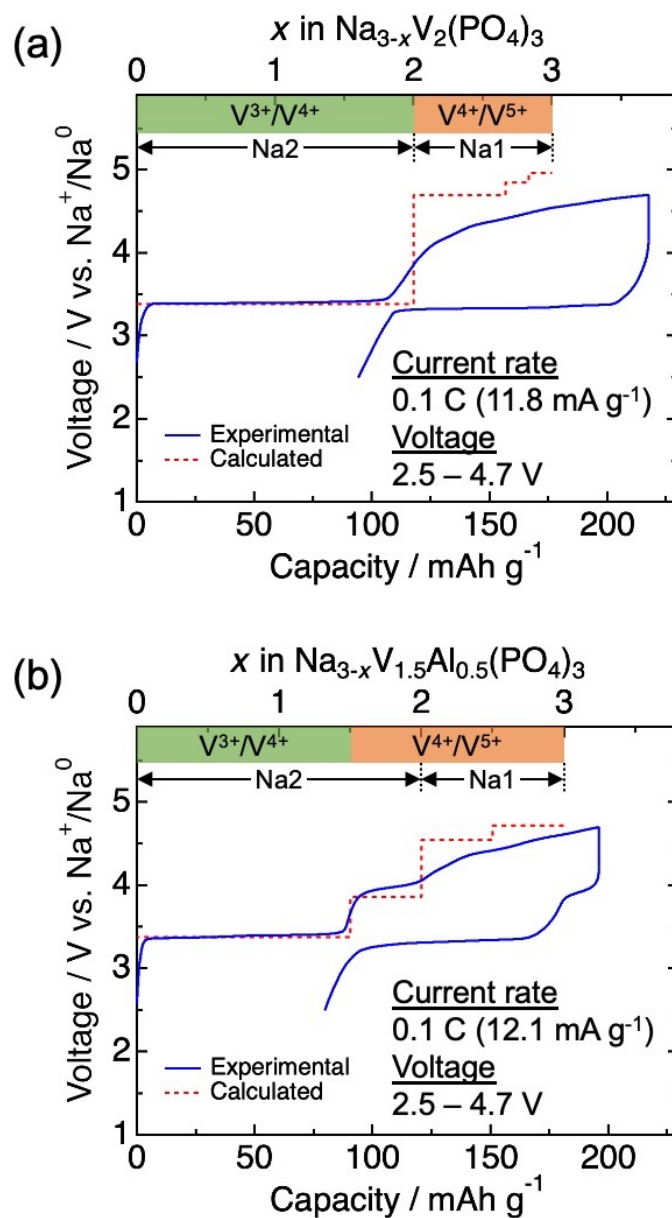
Figure 3-5 Experimental and calculated voltage profiles of **(a)** $Na_3V_2(PO_4)_3$ and **(b)** $Na_3V_{1.5}Al_{0.5}(PO_4)_3$. The voltage range is 2.5–4.7 V. Redox couples corresponding to the range of x in $Na_{3-x}M_2(PO_4)_3$ (M = V and Al) and the Na^+ extraction sites are shown at the top of each plot.

(a)

(b)
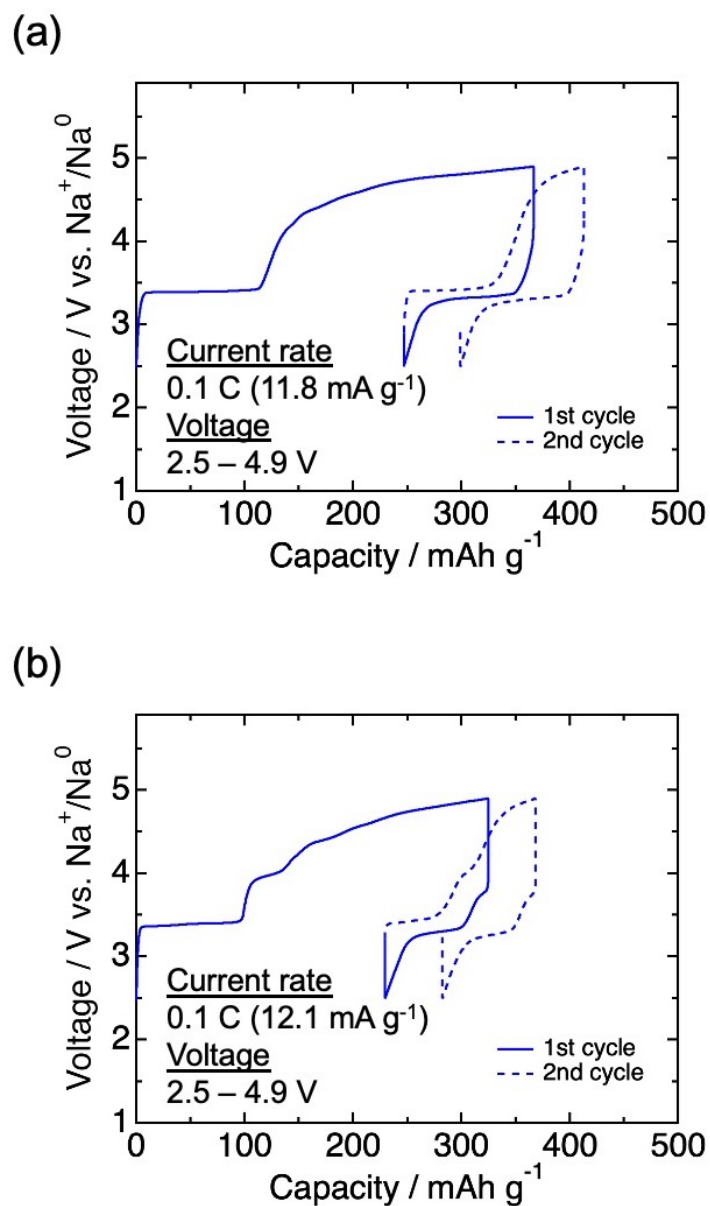
Figure 3-6 Charge/discharge curves of **(a)** $Na_3V_2(PO_4)_3$ and **(b)** $Na_3V_{1.5}Al_{0.5}(PO_4)_3$ in a voltage

range of 2.5–4.9 V at 0.1C.
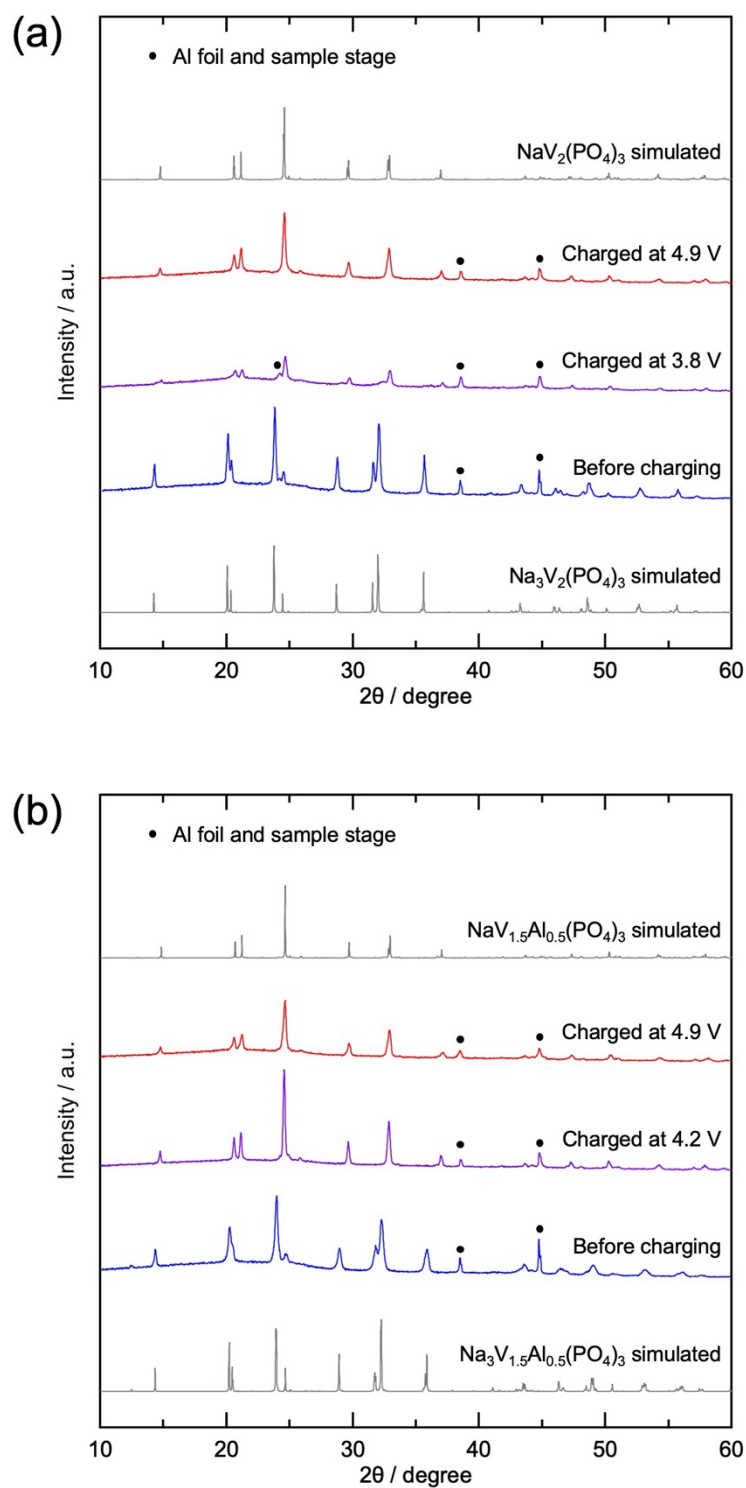
Figure 3-7 *Ex situ* XRD patterns of **(a)** $Na_3V_2(PO_4)_3$ and **(b)** $Na_3V_{1.5}Al_{0.5}(PO_4)_3$ during the charging process at the second cycle. The peak intensity of the $Na_3V_2(PO_4)_3$ electrode at 3.8 V is low due to the poor quality of the electrode surface.

In order to decouple the two contributions to the large voltage step at $x = 2$, the electrochemical property of $Na_3V_{1.5}Al_{0.5}(PO_4)_3$ was also investigated. Figure 3-5b shows the experimental and calculated voltage profiles of $Na_3V_{1.5}Al_{0.5}(PO_4)_3$. In the experimental charge curve, a plateau of V^{3+}/V^{4+} redox was observed at 3.4 V in $0 \leq x \leq 1.5$. Compared to $Na_3V_2(PO_4)_3$, this plateau showed a decreased capacity, because the amount of V was reduced by the partial substitution of Al for V. In addition to the plateau at 3.4 V, a voltage slope was observed at ~ 4.0 V in $1.5 \leq x \leq 2$. The voltage step at $x = 1.5$ is due to the shift of the redox couples from V^{3+}/V^{4+} to V^{4+}/V^{5+}. This result is in good agreement with the previous report [17]. $Na_3V_{1.5}Al_{0.5}(PO_4)_3$ also exhibited a large charge capacity (196 mAh g^{-1}), which is due to the oxidative decomposition of the electrolyte. In the discharge curve, only the voltage slope at ~ 4.0 V and the voltage plateau at 3.4 V were observed, and no additional voltage slope or plateau was observed. In Fig. 3-6b, $Na_3V_{1.5}Al_{0.5}(PO_4)_3$ did not exhibit the third-Na^+ extraction even when it was charged to 4.9 V. *Ex situ* XRD measurements of $Na_3V_{1.5}Al_{0.5}(PO_4)_3$ were also carried out, as shown in Fig. 3-7b. The active material transformed from $Na_3V_{1.5}Al_{0.5}(PO_4)_3$ to $NaV_{1.5}Al_{0.5}(PO_4)_3$ during charging to 4.2 V, and no additional phase transition was observed at the higher voltage. Therefore, as in the case of $Na_3V_2(PO_4)_3$, the third Na^+ was not extracted from $Na_3V_{1.5}Al_{0.5}(PO_4)_3$.

In the DFT calculations, the voltage profile has a plateau at 3.38 V in $0 \leq x \leq 2$ and another plateau at 3.86 V in $1.5 \leq x \leq 2$. Although the predicted voltage of the second plateau (3.86 V) is slightly smaller than the experimental value (~ 4.0 V), the calculated result is roughly consistent with the experimental result. From the DFT calculation, it is found that the Na^+ is extracted from the Na2 site in $0 \leq x \leq 2$, while the shift of the redox couples from V^{3+}/V^{4+} to V^{4+}/V^{5+} occurs at $x = 1.5$. At $x = 2$, another voltage step from 3.86 V to 4.54 V is predicted. This large voltage step is solely attributable to the Na^+ extraction from the Na1 site, because the redox couple remains unchanged at $x = 2$. $Na_3V_{1.5}Al_{0.5}(PO_4)_3$ has another minor voltage

step at $x = 2.5$, which might originate from the change of Na^+ orderings. The voltage of the third-Na^+ extraction in $Na_3V_{1.5}Al_{0.5}(PO_4)_3$ (4.5 V) was lower than that in $Na_3V_2(PO_4)_3$ (4.7 V). This lower voltage is resulted from the stabilization of the desodiated structure by the Al substitution. Further study is needed to elucidate the origin of the structural stabilization induced by the Al substitution. These results revealed that the third-Na^+ extraction is limited due to the high voltage. Such a high voltage is likely to stem from destabilization of the desodiated NASICON structure. However, further studies are needed to elucidate the relationship between the desodiated structure and its stability.

3.3.3. NEB calculations and AIMD simulations of $Na_{3-x}V_2(PO_4)_3$

It is possible that the third-Na^+ extraction is limited due to not only the high voltage but also kinetics. Therefore, NEB calculations were carried out to study the Na^+ diffusivity in $Na_3V_2(PO_4)_3$ and $NaV_2(PO_4)_3$. In the NASICON structures, Na ions hop between the Na1 sites and Na2 sites, resulting in a Na1-Na2-Na1 diffusion path [48, 49]. Thus, in order to extract Na^+ ions at Na1 sites, they must migrate from the Na1 sites to adjacent Na2 sites.

Figure 3-8a illustrates a migration path of Na^+ from a Na1 site to another Na1 site via a Na2 site. Figure 3-8b shows Na^+ migration barriers in $Na_3V_2(PO_4)_3$ and $NaV_2(PO_4)_3$. For $Na_3V_2(PO_4)_3$, the migration energy is 304 meV. This value is in good agreement with previous reports [50]. The energy at the Na2 site (50% of the path distance) is 37 meV. On the other hand, the migration energy in $NaV_2(PO_4)_3$ is 755 meV. This value is much higher than that in $Na_3V_2(PO_4)_3$. Thus, the Na ions at Na1 sites are not likely to migrate to another site. In $NaV_2(PO_4)_3$, the energy at the Na2 site is 655 meV, which is higher than that in $Na_3V_2(PO_4)_3$.

This substantial energy increase is attributed to destabilization of the Na2 site. At the Na2 site, a Na ion is repelled by four neighboring V ions while there are only two V ions near the Na1 site. In $NaV_2(PO_4)_3$, the oxidation state of V is 4+, whereas it is 3+ in $Na_3V_2(PO_4)_3$.

Therefore, the Na2 site in $NaV_2(PO_4)_3$ is destabilized due to the stronger electrostatic repulsions from V^{4+} ions. The shorter Na-V distances at the Na2 site also contribute to the destabilization of the Na2 site. In the DFT calculations, the unit cell volumes of $Na_3V_2(PO_4)_3$ and $NaV_2(PO_4)_3$ are predicted to be 3008 $Å^3$ and 2780 $Å^3$, respectively. Because of this volume contraction after the two-Na^+ extraction, the average Na-V distance at the Na2 site is decreased from 3.73 Å for $Na_3V_2(PO_4)_3$ to 3.51 Å for $NaV_2(PO_4)_3$. This shorter Na-V distance also increases the electrostatic repulsions between Na ions and V ions, resulting in the destabilization of the Na2 site.

For $Na_3V_{1.5}Al_{0.5}(PO_4)_3$, Zhao *et al*. reported that the Al substitution increased the Na-ion migration energy due to the lattice contraction induced by the Al substitution [51]. Therefore, the Al substitution presumably makes the third-Na^+ extraction even more unfavorable, although the NEB calculations for $Na_3V_{1.5}Al_{0.5}(PO_4)_3$ and $NaV_{1.5}Al_{0.5}(PO_4)_3$ were not carried out in this study.

To further investigate the Na^+ diffusivity, the AIMD simulations were also performed for $Na_3V_2(PO_4)_3$ and $NaV_2(PO_4)_3$. Figure 3-9 shows the isosurfaces of Na-ion probability densities for $Na_3V_2(PO_4)_3$ and $NaV_2(PO_4)_3$. Note that Na ions at the initial position are shown in Fig. 3-9ac, and only the isosurfaces are displayed in Fig. 3-9bd. As shown in Fig. 3-9ab, Na ions diffuse via the typical three-dimensional Na1-Na2-Na1 migration paths in the $Na_3V_2(PO_4)_3$ structure [23, 49]. In $NaV_2(PO_4)_3$, on the other hand, Na ions at the Na1 sites remain at their initial positions, as shown in Fig. 3-9cd. This limited Na^+ diffusivity stems from the large migration energy from the Na1 site to the adjacent Na2 site. The results from the NEB calculations and AIMD simulations suggest that the three-Na^+ extraction is hindered due to the large migration energy in $NaV_2(PO_4)_3$, as well as the high voltage.

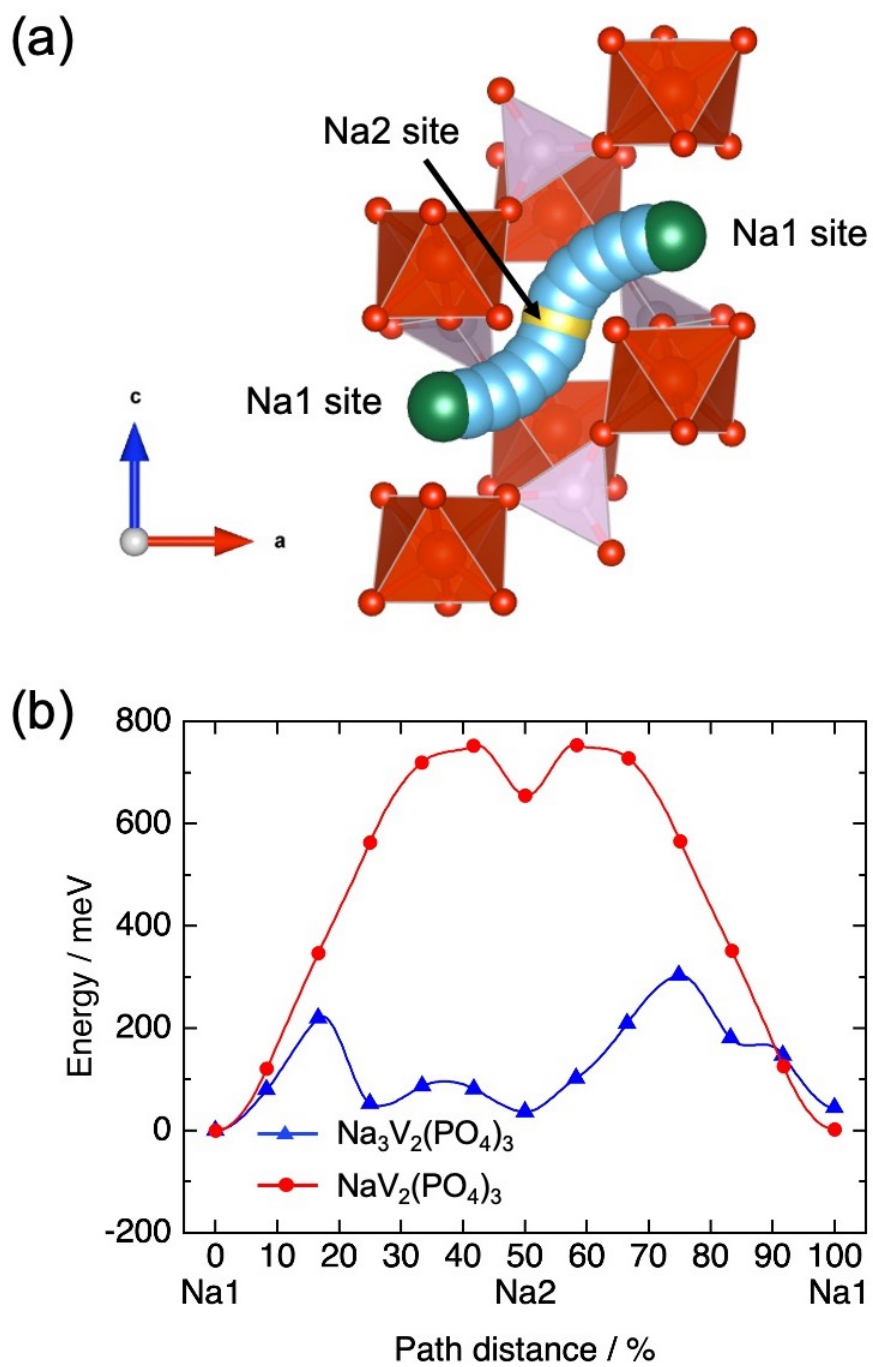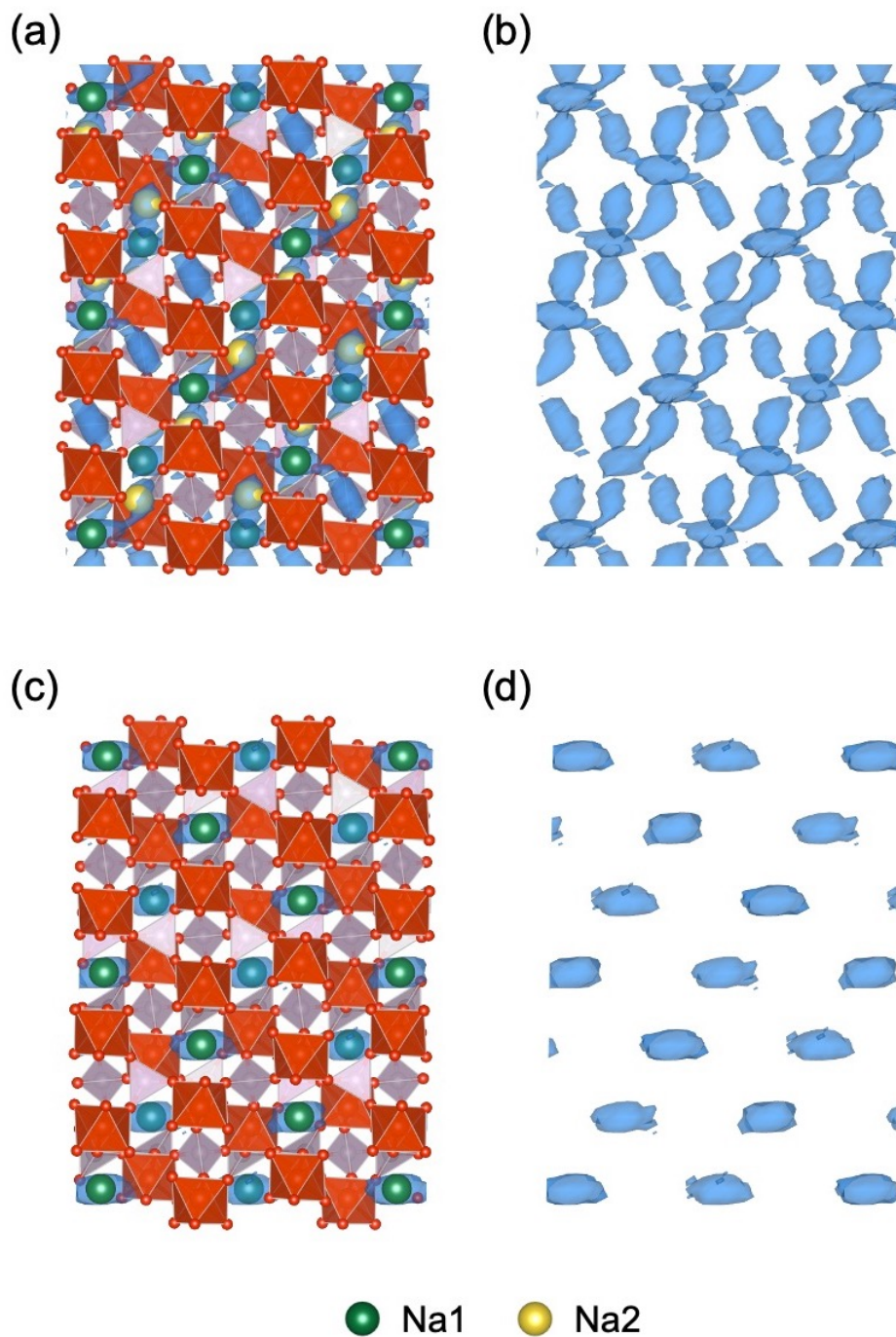**Figure 3-8 (a)** Migration path and **(b)** migration barriers of Na ion in $Na_3V_2(PO_4)_3$ and $NaV_2(PO_4)_3$.

Figure 3-9 Isosurfaces (blue) of Na-ion probability densities obtained from AIMD simulations at 1000 K for **(a)**, **(b)** $Na_3V_2(PO_4)_3$ and **(c)**, **(d)** $NaV_2(PO_4)_3$. Na ions at the initial positions are also shown in (a) and (c). Only the isosurfaces are displayed in (b) and (d).

3.3.4. Voltage profiles and AIMD results of $Li_{3-x}V_2(PO_4)_3$

In contrast to $Na_3V_2(PO_4)_3$, three Li^+ can be extracted from $Li_3V_2(PO_4)_3$ [16]. This discrepancy might originate from the fact that $Li_3V_2(PO_4)_3$ has an anti-NASICON structure whereas $Na_3V_2(PO_4)_3$ has a NASICON structure [52]. Note that there are three Li sites (Li1, Li2, and Li3) in the $Li_3V_2(PO_4)_3$ structure. To compare the two compounds, the property of $Li_3V_2(PO_4)_3$ was investigated by the DFT calculations. Figure 3-10 shows the calculated voltage profile of $Li_3V_2(PO_4)_3$. There are four plateaus, as reported previously [16]. The voltages of the first plateau in $0 \leq x \leq 0.5$ and the second one in $0.5 \leq x \leq 1$ are 3.85 V and 3.92 V, respectively. Note that these voltages are calculated against a Li metal anode. The calculated voltages are higher than the reported ones of 3.6 V and 3.7 V for the first and second plateaus, respectively. The third plateau in $1 \leq x \leq 2$ is 4.12 V. This value is in good agreement with the reported one. These multiple voltage plateaus arise from the Li^+ orderings, and the redox couple remains V^{3+}/V^{4+} in this range ($0 \leq x \leq 2$). At $x = 2$, all Li ions are located in Li2 sites [39, 40], and the redox couples shift from V^{3+}/V^{4+} to V^{4+}/V^{5+}. The voltage of the third-Li^+ extraction from Li2 sites ($2 \leq x \leq 3$) is predicted to be 4.45 V, which is consistent with the experimental results [16]. The voltage is equal to approximately 4.2 V when it is calculated against a Na metal anode. This value is 0.5 V lower than the voltage of the third-Na^+ extraction from $Na_3V_2(PO_4)_3$. The relatively lower voltage enables the third-Li^+ extraction from $LiV_2(PO_4)_3$ without a significant electrolyte decomposition.

AIMD simulations were also performed for $Li_3V_2(PO_4)_3$ and $LiV_2(PO_4)_3$. Figure 3-11 illustrates the isosurfaces of Li-ion probability densities in the two structures. For both compositions, Li ions diffuse three-dimensionally in the $V_2(PO_4)_3$ frameworks. This result suggests that the migration barriers from the Li2 site to another site are small enough, and the third-Li^+ extraction is not kinetically limited. The superior Li^+ diffusivity in $LiV_2(PO_4)_3$ contrasts with the case of $NaV_2(PO_4)_3$, in which the Na^+ is locked up in the Na1 site.

92
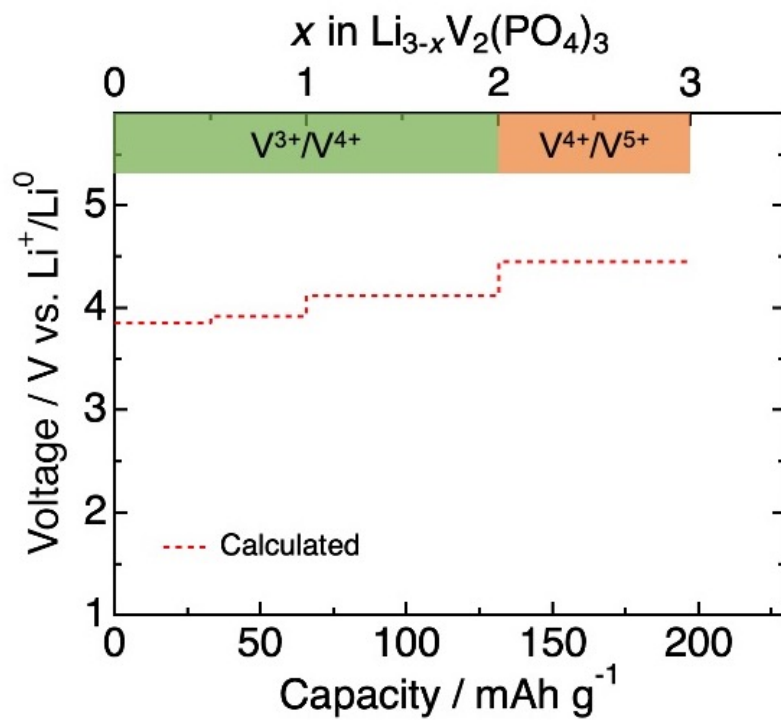
Figure 3-10 Calculated voltage profile of $Li_3V_2(PO4)_3$. Redox couples corresponding to the range of x in $Li_{3-x}V_2(PO_4)_3$ are shown at the top of the plot.

Figure 3-11 Isosurfaces (blue) of Li-ion probability densities obtained from AIMD simulations at 1000 K for **(a), (b)** $Li_3V_2(PO_4)_3$ and **(c), (d)** $LiV_2(PO_4)_3$. Li ions at the initial positions are also shown in (a) and (c). Only the isosurfaces are displayed in (b) and (d).

3.4. Conclusion

In this study, the factors that limit the three-Na^+ extraction from $Na_3V_2(PO_4)_3$ were explored. From the DFT calculations, it is found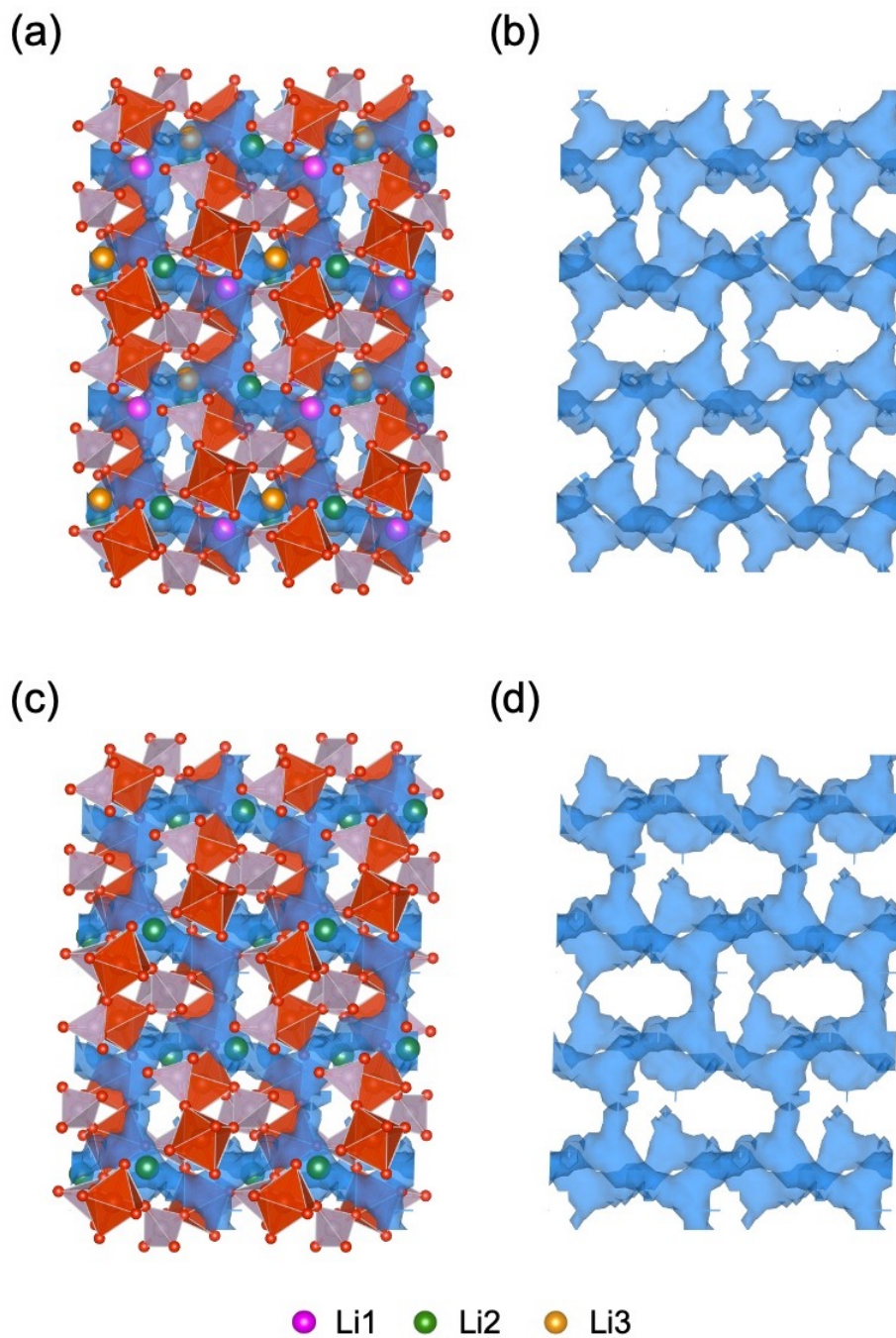 that Na^+ is located in the Na1 sites in both $NaV_2(PO_4)_3$ and $NaV_{1.5}Al_{0.5}(PO_4)_3$. The voltages of the third-Na^+ extractions from $NaV_2(PO_4)_3$ and $NaV_{1.5}Al_{0.5}(PO_4)_3$ are predicted to be more than 4.70 V and 4.54 V, respectively. These voltages are too high for the conventional organic electrolytes. Thus, the oxidative decomposition of the electrolytes occurs before the Na^+ extraction. For $Na_{3-x}V_{1.5}Al_{0.5}(PO_4)_3$, the voltage step was observed at $x = 1.5$ due to the shift of the redox couples from V^{3+}/V^{4+} to V^{4+}/V^{5+}. Moreover, another large voltage step is predicted at $x = 2$ in the DFT calculation. The voltage step at $x = 2$ stems solely from the Na^+ extraction from the Na1 site, since the redox couple remains V^{4+}/V^{5+}. Thus, the three-Na^+ extraction is limited because the high voltage is required to extract Na^+ ions from the Na1 site.

The NEB calculations revealed that the Na^+ migration energy from the Na1 site to Na2 site is 755 meV in $NaV_2(PO_4)_3$, while that in $Na_3V_2(PO_4)_3$ is 304 meV. The AIMD simulations also suggest that the third Na^+ is trapped in the Na1 site in $NaV_2(PO_4)_3$ due to the large migration energy. Therefore, the three-Na^+ extraction is also limited because of the kinetics.

In contrast to $Na_3V_2(PO_4)_3$, $Li_3V_2(PO_4)_3$ exhibits a lower voltage of the third-Li^+ extraction. Moreover, the AIMD simulations suggested that the Li^+ can easily diffuse three-dimensionally in $LiV_2(PO_4)_3$. Accordingly, the three Li^+ ions can be extracted from $Li_3V_2(PO_4)_3$ without a significant electrolyte decomposition or kinetic limitation.

In conclusion, the extraction of three Na ions from $Na_3V_2(PO_4)_3$ has proven challenging due to the high voltage and the substantial migration energy. However, the findings in this work indicate that the three-Na^+ extraction might be achievable by using ionic liquids or solid electrolytes which are stable at high voltage and applying a low rate current. In addition,

elemental substitutions for Na or V may alter the stability of the crystal structure and the Na site energies, and thereby enable the three-Na$^+$ extraction. This study provides important insights toward the design of new NASICON-type cathode materials with higher energy densities.

References

[1]   J.-J. Braconnier, C. Delmas, C. Fouassier, and P. Hagenmuller, *Mater. Res. Bull.*, **15** (1980) 1797–1804.

[2]   A. Kitajou, J. Yamaguchi, S. Hara, and S. Okada, *J. Power Sources*, **247** (2014) 391–395.

[3]   P. Barpanda, G. Oyama, S. Nishimura, S.-C. Chung, and A. Yamada, *Nat. Commun.*, **5** (2014) 4358.

[4]   S. Okada, H. Arai, and J. Yamaki, *Denki Kagaku*, **65** (1997) 802–808.

[5]   Y. Uebou, T. Kiyabu, S. Okada, and J. Yamaki, *The Reports of lnstitute of Advanced Material Study, Kyushu University*, **16** (2002) 1–5.

[6]   Y. Uebou, S. Okada, and J. Yamaki, *Electrochemistry*, **71** (2003) 308–312.

[7]   K. Chihara, A. Kitajou, I. D. Gocheva, S. Okada, and J. Yamaki, *J. Power Sources*, **227** (2013) 80–85.

[8]   R. A. Shakoor, D.-H. Seo, H. Kim, Y.-U. Park, J. Kim, S.-W. Kim, H. Gwon, S. Lee, and K. Kang, *J. Mater. Chem.*, **22** (2012) 20535–20541.

[9]   I. D. Gocheva, M. Nishijima, T. Doi, S. Okada, J. Yamaki, and T. Nishida, *J. Power Sources*, **187** (2009) 247–252.

[10]   K. Chihara, N. Chujo, A. Kitajou, and S. Okada, *Electrochim. Acta*, **110** (2013) 240–246.

[11]   K. Saravanan, C. W. Mason, A. Rudola, K. H. Wong, and P. Balaya, *Adv. Energy Mater.*, **3** (2013) 444–450.

[12]   J. B. Goodenough, H. Y.-P. Hong, and J. A. Kafalas, *Mater. Res. Bull.*, **11** (1976) 203–220.

[13]   Z. Jian, Y. Sun, and X. Ji, *Chem. Commun.*, **51** (2015) 6381–6383.

[14]   J. Gopalakrishnan and K. K. Rangan, *Chem. Mater.*, **4** (1992) 745–747.

[15]   G. Yan, S. Mariyappan, G. Rousse, Q. Jacquet, M. Deschamps, R. David, B. Mirvaux, J. W. Freeland, and J.-M. Tarascon, *Nat. Commun.*, **10** (2019) 585.

[16]   H. Huang, S.-C. Yin, T. Kerr, N. Taylor, and L. F. Nazar, *Adv. Mater.*, **14** (2002) 1525–1528.

[17]   F. Lalère, V. Seznec, M. Courty, R. David, J.-N. Chotard, and C. Masquelier, *J. Mater. Chem. A*, **3** (2015) 16198–16205.

[18]   M. J. Aragón, P. Lavela, R. Alcántara, and J. L. Tirado, *Electrochim. Acta*, **180** (2015) 824–830.

[19]   M. J. Aragón, P. Lavela, G. F. Ortiz, and J. L. Tirado, *ChemElectroChem*, **2** (2015) 995–1002.

[20]   R. Liu, G. Xu, Q. Li, S. Zheng, G. Zheng, Z. Gong, Y. Li, E. Kruskop, R. Fu, Z. Chen, K. Amine, and Y. Yang, *ACS. Appl. Mater. Interfaces*, **9** (2017) 43632–43639.

[21]   A. Inoishi, Y. Yoshioka, L. Zhao, A. Kitajou, and S. Okada, *ChemElectroChem*, **4** (2017) 2755–2759.

[22]   B. M. de Boisse, J. Ming, S.-i. Nishimura, and A. Yamada, *J. Electrochem. Soc.*, **163** (2016) A1469–A1473.

[23]   F. Chen, V. M. Kovrugin, R. David, O. Mentré, F. Fauth, J.-N. Chotard, and C. Masquelier, *Small Methods*, **3** (2018) 1800218.

[24]   Z. Jian, C. Yuan, W. Han, X. Lu, L. Gu, X. Xi, Y.-S. Hu, H. Li, W. Chen, D. Chen, Y. Ikuhara, and L. Chen, *Adv. Funct. Mater.*, **24** (2014) 4265–4272.

[25]   S. Y. Lim, H. Kim, R. A. Shakoor, Y. Jung, and J. W. Choi, *J. Electrochem. Soc.*, **159** (2012) A1393–A1397.

[26]   I. L. Matts, S. Dacek, T. K. Pietrzak, R. Malik, and G. Ceder, *Chem. Mater.*, **27** (2015) 6008–6015.

[27]   K. Momma and F. Izumi, *J. Appl. Crystallogr.*, **44** (2011) 1272–1276.

[28]   F. Izumi and K. Momma, *Solid State Phenom.*, **130** (2007) 15–20.

[29]   G. Kresse and J. Furthmüller, *Comput. Mater. Sci.*, **6** (1996) 15–50.

[30]   G. Kresse and J. Furthmüller, *Phys. Rev. B*, **54** (1996) 11169–11186.

[31]   P. E. Blöchl, *Phys. Rev. B*, **50** (1994) 17953–17979.

[32]   G. Kresse and D. Joubert, *Phys. Rev. B*, **59** (1999) 1758–1775.

[33]   J. P. Perdew, K. Burke, and M. Ernzerhof, *Phys. Rev. Lett.*, **77** (1996) 3865–3868.

[34]   S. L. Dudarev, G. A. Botton, S. Y. Savrasov, C. J. Humphreys, and A. P. Sutton, *Phys. Rev. B*, **57** (1998) 1505–1509.

[35]   H. Kim, Y. Ishado, Y. Tian, and G. Ceder, *Adv. Funct. Mater.*, **29** (2019) 1902392.

[36]   S. P. Ong, W. D. Richards, A. Jain, G. Hautier, M. Kocher, S. Cholia, D. Gunter, V. L. Chevrier, K. A. Persson, and G. Ceder, *Comput. Mater. Sci.*, **68** (2013) 314–319.

[37]   J.-N. Chotard, G. Rousse, R. David, O. Mentré, M. Courty, and C. Masquelier, *Chem. Mater.*, **27** (2015) 5982–5987.

[38]   K. Okhotnikov, T. Charpentier, and S. Cadars, *J. Cheminform.*, **8** (2016) 17.

[39]   S.-C. Yin, H. Grondey, P. Strobel, M. Anne, and L. F. Nazar, *J. Am. Chem. Soc.*, **125** (2003) 10402–10411.

[40]   S.-C. Yin, H. Grondey, P. Strobel, H. Huang, and L. F. Nazar, *J. Am. Chem. Soc.*, **125** (2003) 326–327.

[41]   M. K. Aydinol, A. F. Kohan, G. Ceder, K. Cho, and J. Joannopoulos, *Phys. Rev. B*, **56** (1997) 1354–1365.

[42]   G. Henkelman and H. Jónsson, *J. Chem. Phys.*, **113** (2000) 9978–9985.

[43]   D. Sheppard, P. Xiao, W. Chemelewski, D. D. Johnson, and G. Henkelman, *J. Chem. Phys.*, **136** (2012) 074103.

[44]   S. Nosé, *J. Chem. Phys.*, **81** (1984) 511–519.

[45]   W. G. Hoover, *Phys. Rev. A*, **31** (1985) 1695-1697.

[46]   A. Jain, S. P. Ong, G. Hautier, W. Chen, W. D. Richards, S. Dacek, S. Cholia, D. Gunter, D. Skinner, G. Ceder, and K. A. Persson, *APL Mater.*, **1** (2013) 011002.

[47]   Z. Jian, W. Han, X. Lu, H. Yang, Y.-S. Hu, J. Zhou, Z. Zhou, J. Li, W. Chen, D. Chen, and L. Chen, *Adv. Energy Mater.*, **3** (2013) 156–160.

[48]   H. Kabbour, D. Coillot, M. Colmont, C. Masquelier, and O. Mentré, *J. Am. Chem. Soc.*, **133** (2011) 11900–11903.

[49]   Y. Deng, C. Eames, L. H. B. Nguyen, O. Pecher, K. J. Griffith, M. Courty, B. Fleutot, J.-N. Chotard, C. P. Grey, M. S. Islam, and C. Masquelier, *Chem. Mater.*, **30** (2018) 2618–2630.

[50]   K. M. Bui, V. A. Dinh, S. Okada, and T. Ohno, *Phys. Chem. Chem. Phys.*, **17** (2015) 30433–30439.

[51]   L. Zhao, H. Zhao, Z. Du, N. Chen, X. Chang, Z. Zhang, F. Gao, A. Trenczek-Zajac, and K. Świerczek, *Electrochim. Acta*, **282** (2018) 510–519.

[52]   C. Masquelier and L. Croguennec, *Chem. Rev.*, **113** (2013) 6552–6591.

Chapter 4

Cathode Properties of Perovskite-type NaMF$_3$ (M = Fe, Mn, and Co) Prepared by Mechanical Ball Milling for Na-ion Batteries

4.1. Introduction

NIBs, which have a working mechanism similar to that of LIBs, have drawn much interest as potential energy storages for large-scale grid energy storage because of their low cost and the abundance of sodium resources. Therefore, reports on the electrochemical properties of NIBs have increased recently. In particular, large-scale NIBs are expected to become commercially viable by using earth-abundant transition metals such as Fe and Mn. Minor-metal-free compounds with open structures, such as O3-type NaFeO$_2$ [1], Na$_2$FeP$_2$O$_7$ [2] and Na$_2$FePO$_4$F [3], have attracted much attention for their potential in the development of next-generation NIBs with good cost performance. Recently, Barpanda *et al*. reported that alluaudite-type Na$_2$Fe$_2$(SO$_4$)$_3$ exhibits the highest Fe^{2+}/Fe^{3+} redox potential of 3.8V among iron-based cathode materials [4]. The theoretical capacity of this material is 120 mAh g^{-1}, and its theoretical energy density is 456 Wh kg^{-1}, which is smaller than that of the LiMn$_2$O$_4$ cathode used for LIBs.

On the other hand, 3d-transition metal fluorides such as MF_3 (M = Fe, Mn, Co, V, and Ti) have attracted attention due to their ability to generate high levels of electrochemical energy [5]. In particular, FeF_3 has a large theoretical capacity of 200 mAh g^{-1}, and a discharge capacity of 150 mAh g^{-1} with a voltage of 2.7 V vs. Na^+/Na^0 was reported [5]. However, 3d-transition metal fluorides such as MF_3 are not practical for application in NIBs with a carbonaceous anode, because the initial composition of the cathode has no Na ions.

Alternatively, perovskite-type $NaMF_3$ (M = Fe and Mn), which have the same chemical compositions as the discharged state of the MF_3 cathodes, have been investigated as cathode materials for NIBs due to their unusually high voltage characteristics and large theoretical capacities [6-8]. Perovskite-type $NaFeF_3$ prepared by mechano-chemical synthesis had a discharge capacity of 120 mAh g^{-1} at around 2.7V, which corresponded to 61% of the theoretical capacity (197 mAh g^{-1}) [6]. The reason for this poor efficiency is that mechanochemically synthesized $NaFeF_3$ had relatively lower crystallinity, and Fe^{3+} was partially contained in an amorphous phase. In further investigations, Kitajou *et al*. and Yamada *et al*. reported on the cathode properties of $NaFeF_3$ obtained using the liquid-phase and roll-quench methods [7, 8]. However, these $NaFeF_3$ cathodes had large charge/discharge polarization, and the cycling efficiency after 20 cycles was 79% [6]. Although the perovskite-type $NaMnF_3$ and $NaCoF_3$ can also be prepared by mechanochemical synthesis and the liquid-phase method [9, 10], the properties of these cathode materials and their average voltages have not yet been clarified.

The aims of this work are to improve the cathode properties of $NaFeF_3$ and to evaluate the cathode properties of $NaMnF_3$ and $NaCoF_3$. $NaMF_3$ (M = Fe, Mn, and Co) were prepared using the mechanochemical method, and a two-step carbon-mixing was performed to obtain uniform carbon composites with the obtained $NaMF_3$. The structural change of the obtained cathode materials during the charge/discharge was investigated using XRD measurements to

determine the corresponding reaction mechanism. In addition, the theoretical voltage characteristics of the $NaMF_3$ cathodes were calculated using DFT.

4.2. Experimental

4.2.1. Materials synthesis

The syntheses of $NaMF_3$ (M = Fe, Mn, and Co) were conducted using a mechanical ball-milling method. Mixtures of NaF and MF_2 (M = Fe, Mn, and Co) with a molar ratio of NaF:MF_2 = 1.2:1 were placed in an Ar-filled container with 3 mm-diameter ZrO_2 balls under an Ar atmosphere. The mixture was ball-milled using a planetary mill (Pulverisette 7; Fritsch) with a rotation speed of 600 rpm for 6 h. The obtained products were then subjected to the two-step carbon coating process. Briefly, the obtained 70 wt.% $NaMF_3$ powder was placed in an Ar-filled container with 5 wt.% AB and ball-milled at a rotation speed of 600 rpm for 3 h. A mixture of the resultant $NaMF_3$/AB and 20 wt.% AB was ball-milled again with a rotation speed of 400 rpm for 3 h to produce a composite of carbon and $NaMF_3$, which was denoted $NaMF_3$/C.

4.2.2. Electrochemical tests

Cathode pellets were fabricated by mixing the obtained $NaMF_3$/C with PTFE binder (Polyflon PTFE F-104; Daikin Industry) in a 95:5 weight ratio and then pressing into disks (ca. 20 mg weight and 10 mm diameter). They were fabricated in an Ar-filled glove box and dried at approximately 120 ℃ overnight under a vacuum before assembling the cells. The electrochemical performance of the obtained $NaMF_3$/C was evaluated using a 2032 coin-type cell with 1M $NaPF_6$/PC:FEC (95:5 in vol.%) (Tomiyama Pure Chemical Industries) as an

electrolyte, and a glass separator (GA-55, Advantec) against sodium metal (Aldrich) as the anode material. All cells were assembled in an Ar-filled glove box with a dew point of -80 ºC. Measurements of the cathode properties were performed in galvanostatic mode, and all tests were conducted at 25 ºC.

4.2.3. *Ex situ* measurements

To avoid oxidation of the iron in the air, cathode pellets for *ex situ* XRD (TTRIII, Rigaku; 50 kV and 300 mA, Cu Ka radiation) measurements were carefully removed from the cells in the Ar-filled glove box, washed, and then immersed in DMC overnight to remove the electrolyte. The cathode pellets were then dried and set in Ar-filled sample folders (Rigaku) for XRD measurements. The *in situ* X-ray absorption near edge structure (XANES) spectra of the Fe K-edge were obtained using synchrotron radiation on the BL11 beamline at the Saga Light Source using a Si (1 1 1) double crystal monochromator.

4.2.4. Computational methods

First-principles calculations were based on DFT using the PAW method [11, 12] as implemented in the VASP [13, 14]. The PBE functional [15] with the Hubbard U correction (U_{eff} = 5 eV for M d states, M = Fe, Mn, and Co) [16] was employed. The cutoff energy of 500 eV for the plane-wave expansion of the wave functions was used. k-point meshes of 4 × 4 × 4 with the Monkhorst-Pack scheme [17] were adopted for Brillouin zone integration. All atomic structures were fully relaxed until the atomic forces were less than 0.01 eV Å^{-1}, and the lattice parameters of unit cells were also fully optimized. Ferromagnetic (FM) and the G-type antiferromagnetic (each Fe is surrounded by six neighboring Fe with antiparallel spins, G-type AFM) [18] orderings were assumed for the M atoms (M = Fe, Mn, and Co) in the $Na_{1-x}MF_3$ (0

$\leq x \leq 1$) models, and attention was focused on the lowest-energy magnetic structures of each model.

Formation energy $E_f(x)$ was calculated by using Eq. (4-1):

$$E_f\left(\mathrm{Na}_{1-x}\mathrm{MF}_3\right) = E\left(\mathrm{Na}_{1-x}\mathrm{MF}_3\right) - (1-x)E\left(\mathrm{NaMF}_3\right) - xE\left(\mathrm{MF}_3\right) \qquad (4\text{-}1)$$

where $E(\mathrm{A})$ is the DFT total energy per formula unit of system A.

The voltage is calculated as follows:

$$V\left(x_1, x_2\right) = -\frac{E\left(\mathrm{Na}_{1-x_1}\mathrm{MF}_3\right) - E\left(\mathrm{Na}_{1-x_2}\mathrm{MF}_3\right) - (x_2 - x_1)E\left(\mathrm{Na}\right)}{(x_2 - x_1)F} \qquad (4\text{-}2)$$

where $x_2 > x_1$.

4.3. Results and Discussion

4.3.1. Materials characterization

Characterization of the NaMF$_3$/C composite mixture obtained just after mechanical milling was conducted using XRD (TTRIII, Rigaku; 50 kV and 300 mA, Cu Ka radiation) and the results are shown in Fig. 4-1. The NaMF$_3$ (M = Fe, Mn, and Co) in the composites were indexed as orthorhombic structures with space group *Pnma*. However, there were also some impurity phases of unknown composition. Moreover, the peaks in the XRD profiles were broad, and the background was high, which indicates that the obtained products have lower crystallinity or nano-sized particles. Table 4-1 presents the lattice constants for NaMF$_3$ in ICDD and the obtained products. These calculated lattice constants were in good agreement with those of the ICDD data. The particle size of the obtained NaMF$_3$/C (M = Fe, Mn, and Co) was observed by TEM measurements (Fig. 4-2). The darker areas and lighter areas indicate the active materials and carbon, respectively. The primary particle sizes of the obtained samples were about 20-100 nm in diameter. For NaFeF$_3$/C, large agglomerated particles were observed, indicating the less homogeneous distribution of active materials compared to NaMnF$_3$/C and NaCoF$_3$/C.

Table 4-1 Lattice constants for ICDD and the obtained NaMF$_3$ (M = Fe, Mn, and Co).

	ICDD*			Obtained product		
	a / Å	b / Å	c / Å	a / Å	b / Å	c / Å
NaFeF$_3$	5.66	7.88	5.48	5.66	7.86	5.51
NaMnF$_3$	5.75	8.01	5.55	5.75	8.00	5.56
NaCoF$_3$	5.61	7.79	5.42	5.62	7.83	5.44

*NaFeF$_3$ (ICDD:00-043-0705), NaMnF$_3$ (ICDD:00-018-1224), NaCoF$_3$ (ICDD:01-070-1889).
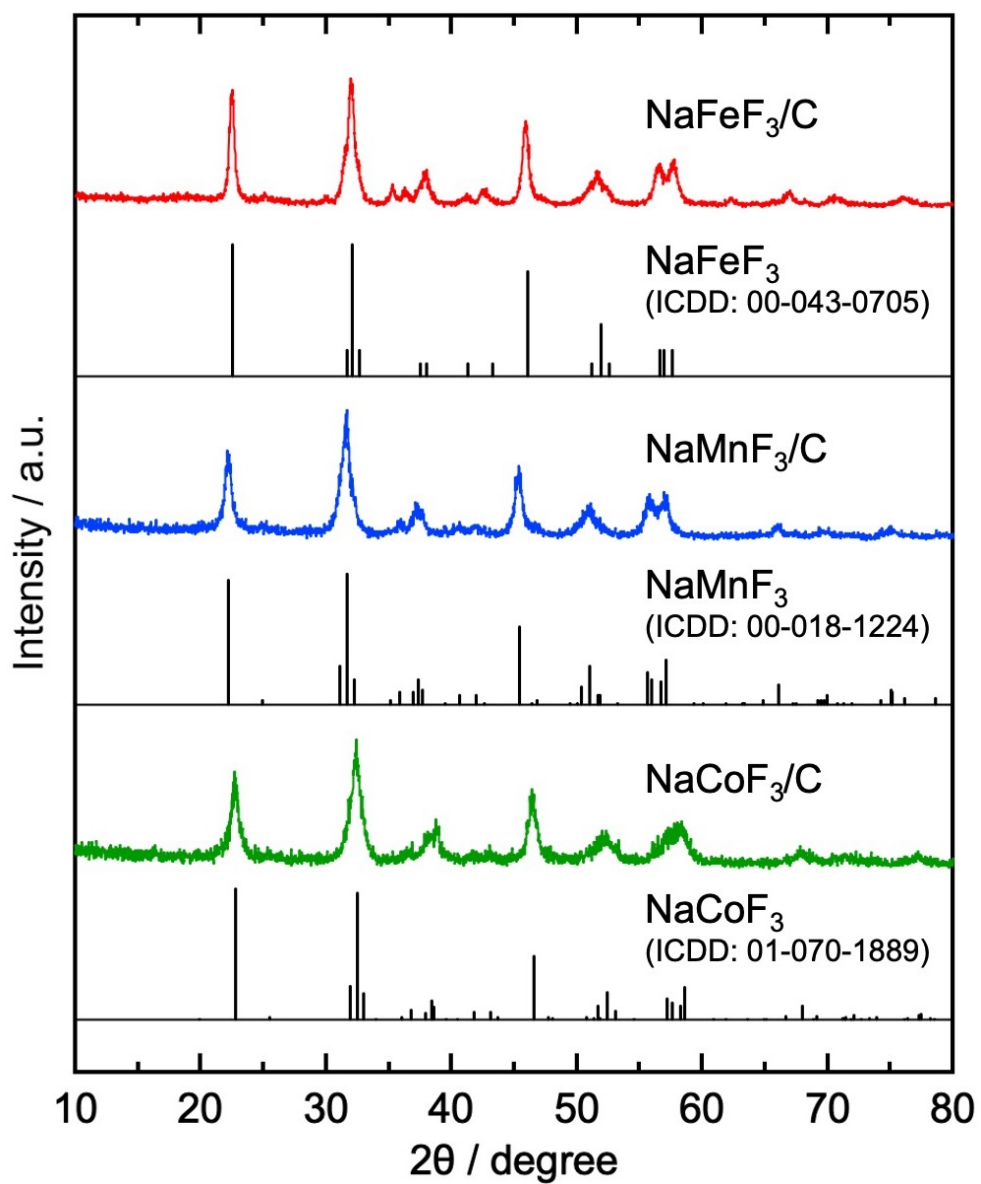
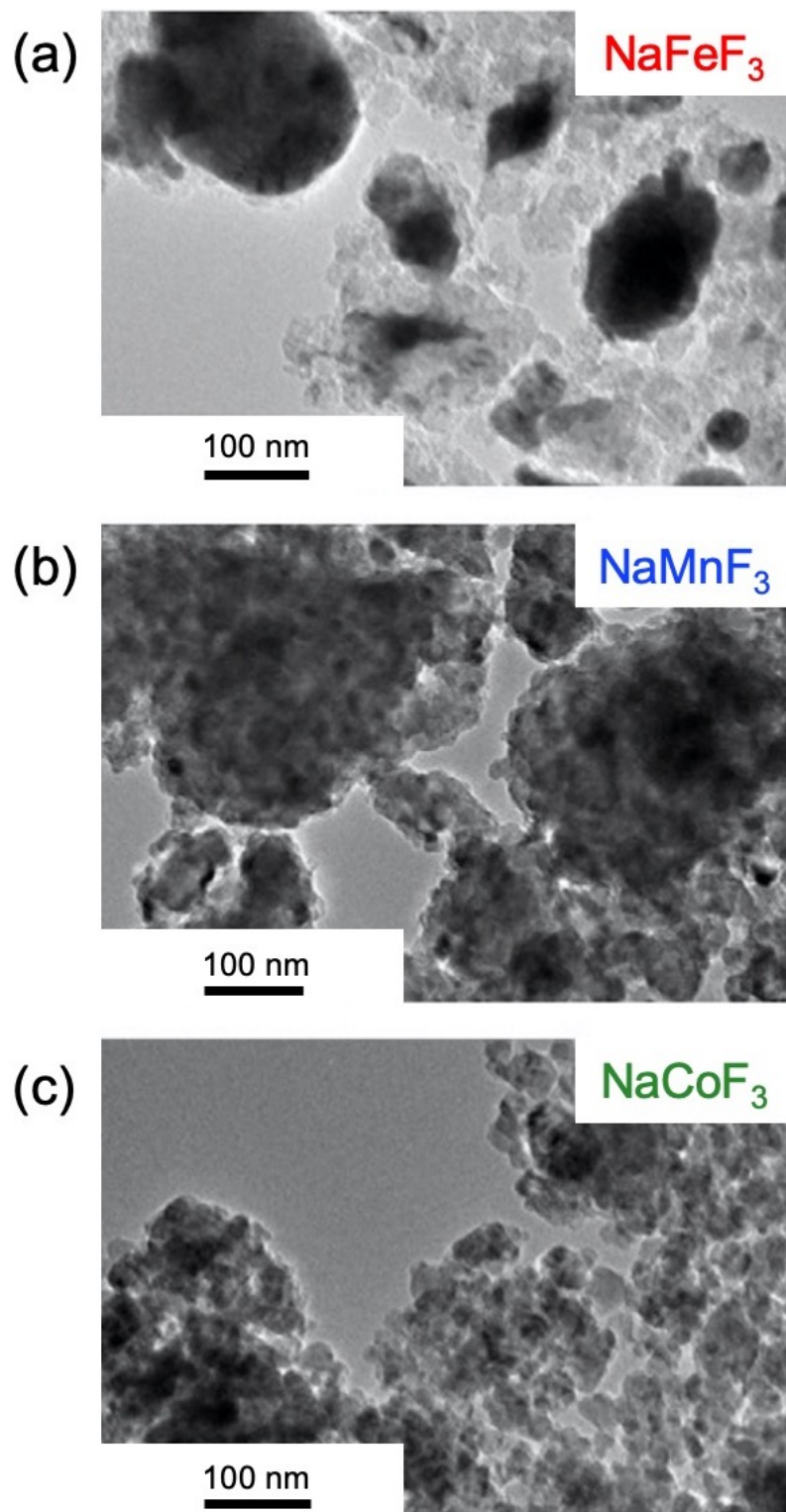**Figure 4-1** XRD patterns of NaMF$_3$/C (M = Fe, Mn, and Co).

Figure 4-2 TEM images of NaMF$_3$/C (M = Fe, Mn, and Co).

4.3.2. Electrochemical properties of NaMF₃

Figure 4-3 shows the initial charge/discharge profiles and cyclabilities for the $NaMF_3$/C (M = Fe, Mn, and Co) cathode composites at a rate of 0.1 mA cm^{-2}. These electrochemical measurements were conducted using potential windows of 2.0–4.3V for $NaFeF_3$ and 2.0–4.6V for $NaMnF_3$ and $NaCoF_3$. For the $NaFeF_3$, the cell voltage gradually increased through inflection points at around 3.1 V and 3.5 V during the initial charge process (Fig. 4-3a). The reversible capacity was 169 mAh g^{-1}, which corresponds to a 0.85 Na$^+$ insertion/extraction reaction. While the reported average discharge voltage of $NaFeF_3$ [6-8] and the voltage calculated by the DFT method [19] were both ca. 2.7 V, the $NaFeF_3$ synthesized in this work showed an average discharge voltage of 2.9 V. The higher average voltage is attributed to the fact that the cutoff voltage for the discharging was set to 2.0 V in this study, whereas it was set to 1.5 V in the previous reports. Below the 2.0 V, the conversion reaction might occur, resulting in the lower average voltage. The $NaFeF_3$ in this work also showed the smaller polarization between the charge and discharge voltage profiles than that of the previous reports [6-8]. The improved electrochemical property is likely to stem from the small particle size and the well-dispersed carbon, which provides electron conduction paths.

As shown in Fig. 4-3b, the $NaMnF_3$ cathode exhibited a reversible capacity of 89 mAh g^{-1}. Nava-Avendaño *et al*. previously reported that the $NaMnF_3$ cathode had a larger reversible capacity of ca. 150 mAh g^{-1} [10]. The authors presumed that the larger capacity partially originated from the electrolyte oxidation facilitated by the strong oxidizing character of the MnF_3 phase. The overpotential in the report was substantial, and no plateau for the Mn^{2+}/Mn^{3+} was confirmed during the charge/discharge reaction. In this study, on the other hand, a voltage slope for the Mn^{2+}/Mn^{3+} was observed at around 3.6 V in the discharge curve. This difference arises from the different particle sizes. The particle size obtained in this study was about 20-100 nm, whereas the $NaMnF_3$ formed large agglomerated particles (ca. 13 μm) in the previous

report [10]. Due to the insulating character of the fluorides, the large particles tend to exhibit a large overpotential.

These results suggest that the cathode properties of $NaFeF_3$ and $NaMnF_3$ are improved by the two-step carbon mixing method, which provides uniform composites of the active material and the carbon. The energy density of the $NaFeF_3$ cathode was over 480 Wh kg^{-1}. The reported energy density of $Na_{2/3}Fe_{0.5}Mn_{0.5}O_2$, a promising iron-based cathode material, was 570 Wh kg^{-1}, and the initial charge and discharge capacities of this material were 120 mAh g^{-1} and 190 mAh g^{-1}, respectively [20]. Since the initial composition of this material is Na^+-deficient, an anode for the $Na_{2/3}Fe_{0.5}Mn_{0.5}O_2$ is required to contain some Na^+ in the initial state to compensate for the deficient Na^+. Therefore, the obtained $NaFeF_3$ can be competitive with $Na_{2/3}Fe_{0.5}Mn_{0.5}O_2$, because the $NaFeF_3$ does not require the Na^+ pre-doped anode.

Figure 4-4 shows the cycle performance of the $NaFeF_3$ and $NaMnF_3$. The $NaFeF_3$ has low cyclability, and the capacity retention was 56% after 20 cycles. The discharge capacity of $NaMnF_3$ was approximately 40 mAh g^{-1} after 20 cycles, and the capacity retention was only 45%. The capacity fading might arise from the electrolyte decomposition, the irreversible structural changes during the charge/discharge cycles, and the elution of the Fe and Mn ions. Moreover, the repeated volume expansion and contraction during the cycles can lead to poor electronic connectivity between the active material and the carbon, resulting in an increase of the resistance. These factors may lead to an increase in the overpotential and reduced active material utilization, resulting in cycle degradation. After a number of cycles, the capacities become constant. This might be due to the decreased amount of electrolyte decomposition with the decrease in the charge capacity, and the capacity reaches a steady state at a certain value. The formation of the SEI might be another factor since the SEI can inhibit the electrolyte decomposition and the dissolution of Fe and Mn.

On the other hand, the NaCoF$_3$ cathode had a low reversible capacity of 38 mAh g^{-1} with a potential window of 2.0–4.6 V. Dimov *et al*. also reported that a rechargeable capacity of NaCoF$_3$ was hardly obtained, and the XRD peak was not shifted during the initial charge reaction [9]. Therefore, the observed capacity originated not from the Co^{2+}/Co^{3+} redox but rather from the side reactions. Nava-Avendaño *et al*. conducted blank experiments with working electrodes containing only carbon, and the charge capacity induced by the electrolyte decomposition was determined as ca. 70 mAh g^{-1} [10]. In addition, it was reported that the PF$_6^{-}$ ions could be inserted in the layers of carbon in the high voltage region [21]. Thus, the side reaction is presumably the electrolyte decomposition and/or the insertion of PF$_6^{-}$ ions into the layers of the carbon.
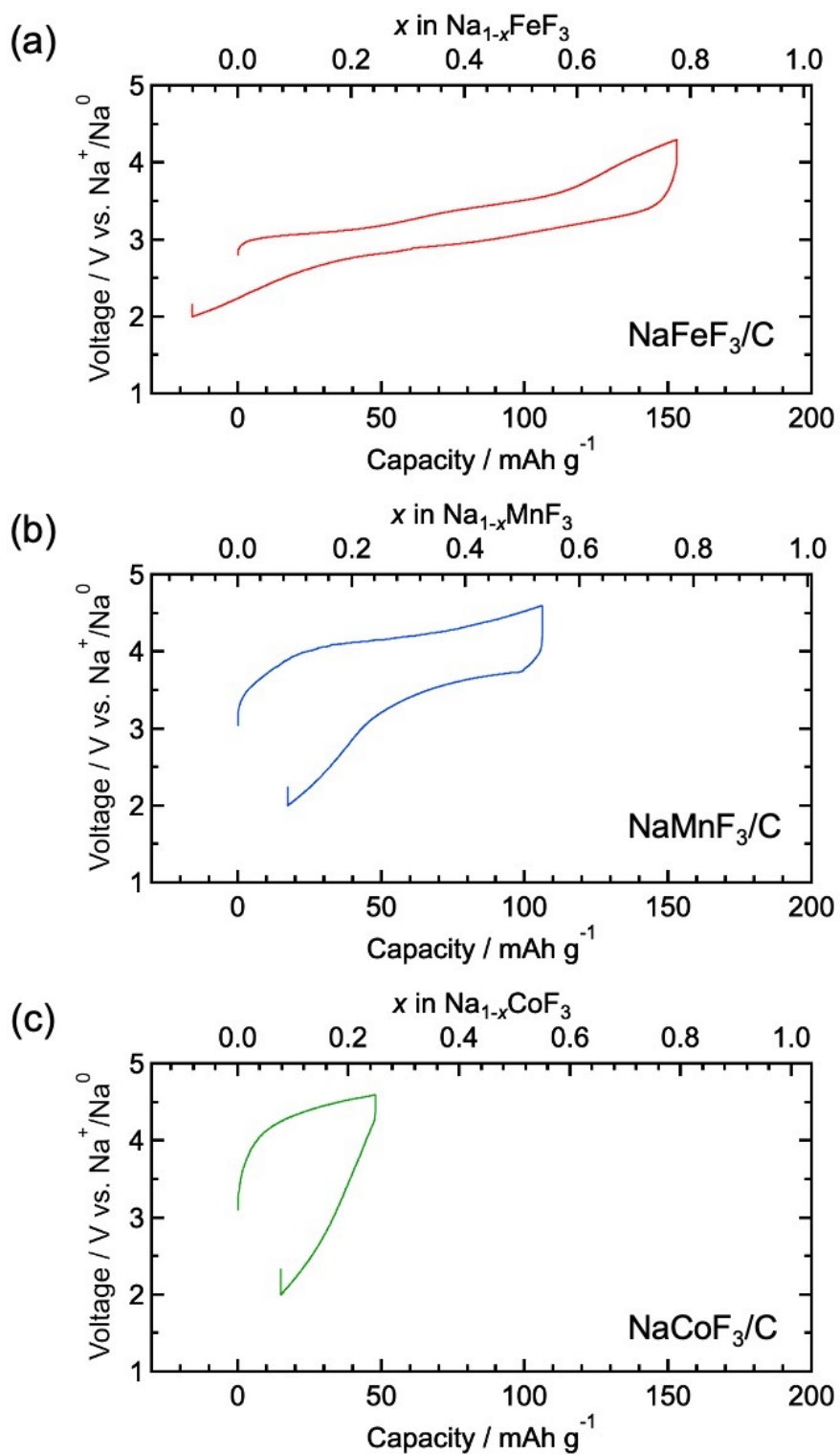
Figure 4-3 Initial charge and discharge curves for the NaMF$_3$/C (M = Fe, Mn and Co) cathodes at a rate of 0.1 mA cm^{-2} between 2.0 and 4.3 V for **(a)** NaFeF$_3$, and between 2.0 and 4.6 V for **(b)** NaMnF$_3$ and **(c)** NaCoF$_3$.
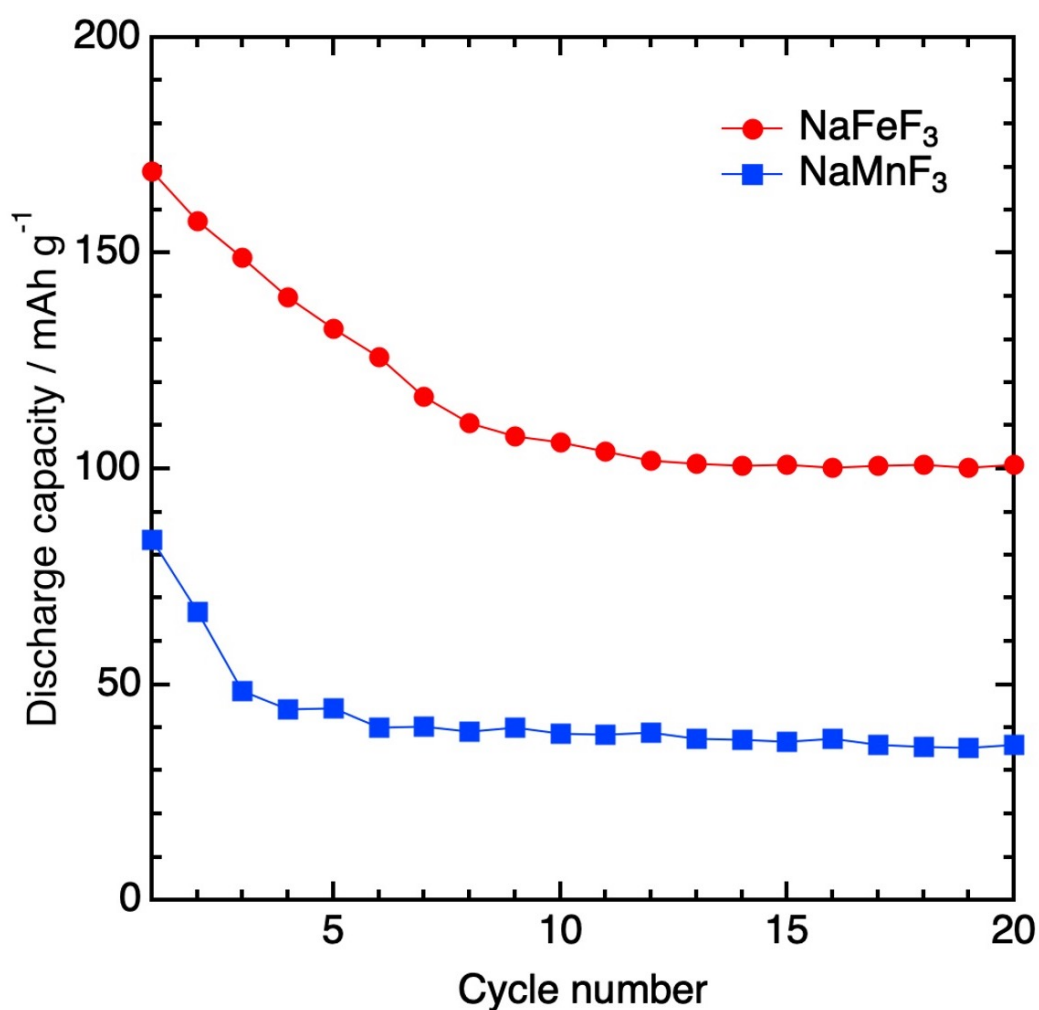
Figure 4-4 Cycle performance of NaFeF$_3$/C and NaMnF$_3$/C.

4.3.3. *Ex situ* XRD and *in situ* XANES

To investigate the charge/discharge mechanism, *ex situ* XRD measurements were carried out. Figure 4-5 shows the *ex situ* XRD patterns for NaFeF$_3$ and NaMnF$_3$. For the NaFeF$_3$ cathode (Fig. 4-5a), all XRD peaks were shifted continuously to higher 2θ angles throughout the charging process up to 4.3 V and were then shifted back to almost the original

position after the first discharge process. This result suggests that the perovskite-type frameworks composed of FeF_6 octahedra are basically maintained during the charge and discharge processes. The change in the unit cell volume of $NaFeF_3$ that accompanies the extraction/insertion of sodium was −7%. For comparison, the previously reported change in the unit cell volume of $NaFeF_3$ was −1.2% [7]—that is, the obtained $NaFeF_3$ exhibited a larger change in unit cell volume during the extraction/insertion of sodium than the $NaFeF_3$ in the previous report.

Moreover, *in situ* XANES Fe K-edge data were acquired for the $NaFeF_3$ as a means of examining the oxidation states after the charge processes. Figure 4-6a shows the charge curves obtained from the electrochemical cell at a rate of 40 mA g^{-1}. The colored dots indicate the points where the XANES spectra were acquired. Figure 4-6b presents the XANES spectra in the Fe K-edge region. The color of each spectrum corresponds to the points in Fig. 4-6a. The XANES spectrum before charging did not match to that of FeF_2 due to the structural difference between the samples and the reference. Throughout the charging process, the spectra continuously shifted to higher energies up to 4.0 V, indicating the oxidation of the Fe ion. During the charging from 4.0 to 4.3 V, there were no further shifts. Therefore, the charge reactions between 4.0 and 4.3 V may have included additional side reactions. It is conjectured that these side reactions, which could include electrolyte decompositions and the large expansion-contraction of the lattice, contributed to the lower cyclability of $NaFeF_3$/C.

For the $NaMnF_3$ cathode (Fig. 4-5b), some peak positions (e.g., 37.2º) were shifted to higher 2θ angles after the charging process up to 4.6 V from the initial peak position and were then returned to the original position after the discharge process down to 2.0 V. Therefore, $NaMF_3$ cathodes can also accommodate the extraction/insertion of sodium by reversible expansion/contraction of the lattice volume, i.e., the $NaMF_3$ cathodes maintain the MF_3 sublattice symmetry during the charge/discharge processes.
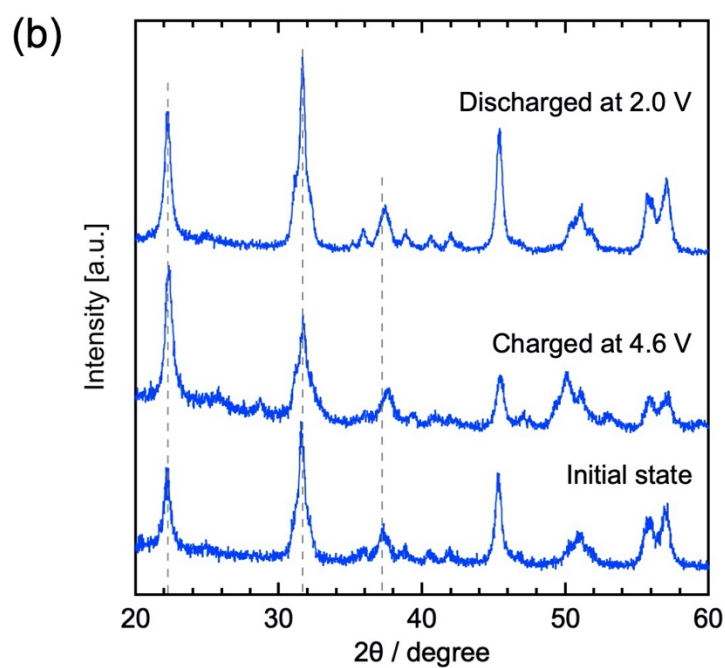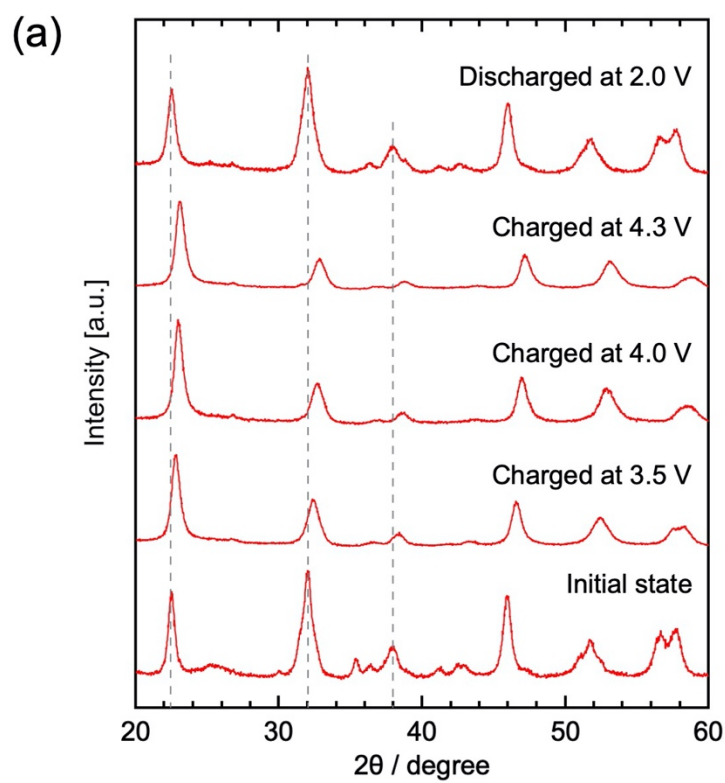
Figure 4-5 *Ex situ* XRD profiles for (a) NaFeF$_3$/C and (b) NaMnF$_3$a/C cathode pellets during the initial charge/discharge cycle.
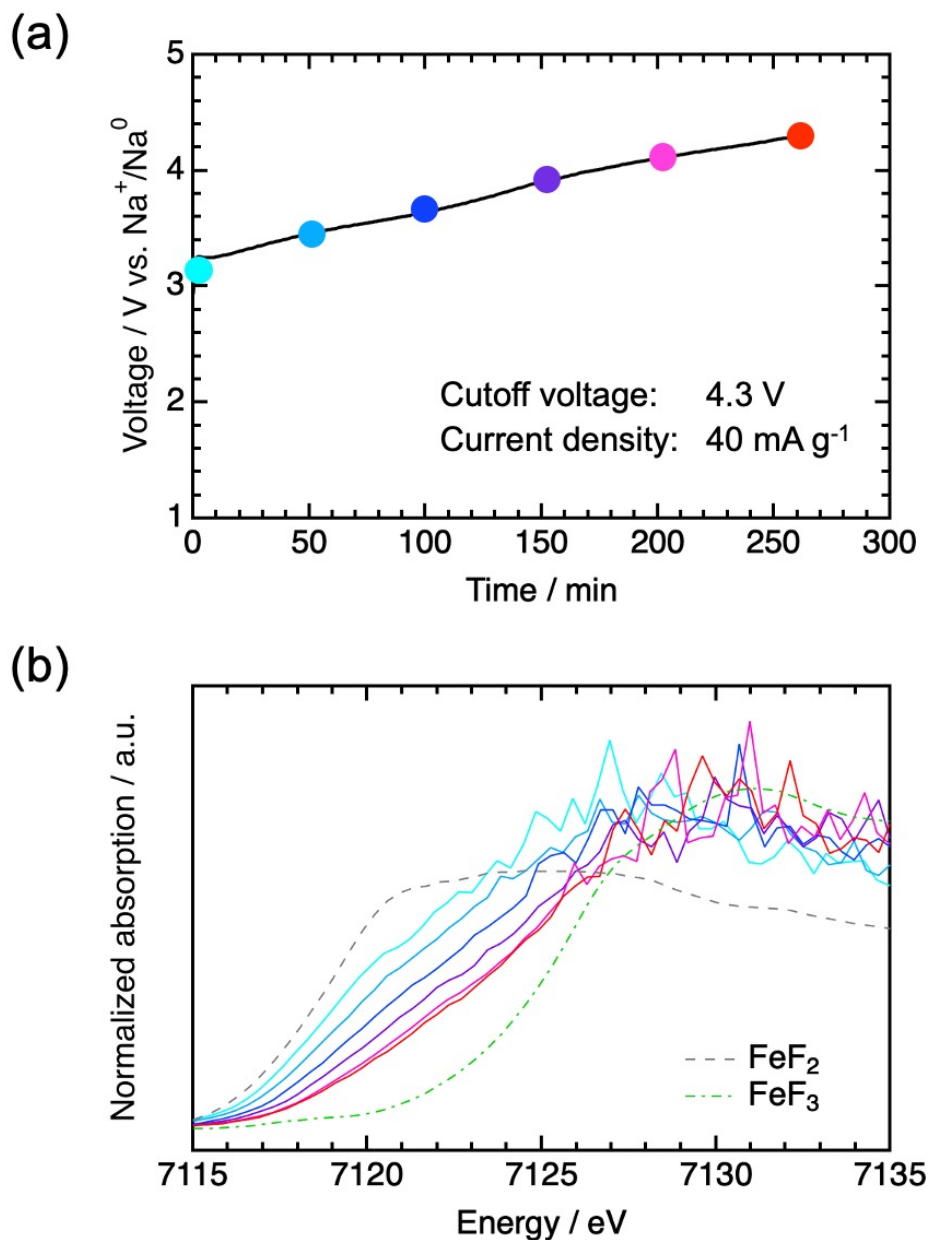
Figure 4-6 (a) The initial charge curve obtained from NaFeF$_3$ using the electrochemical cell applied to *in situ* XANES measurements. The colored dots indicate the points where the XANES spectra were acquired. (b) XANES spectra at the Fe K-edge during the initial charging of NaFeF$_3$. The color of each spectrum corresponds to the points in the initial charge curve. The spectra of FeF$_2$ and FeF$_3$ standard samples are also shown.

4.3.4. DFT calculations

To understand the atomistic reaction mechanisms in these cathodes, the theoretical voltage characteristics of the $Na_{1-x}MF_3$ ($0 \leq x \leq 1$; M = Fe, Mn, and Co) cathode materials were calculated as a function of the Na content x, using the DFT method. Based on the results of *ex situ* XRD measurements (Fig. 4-5), the orthorhombic $NaMF_3$ (M = Fe, Mn, and Co) structure with the space group *Pnma* and the desodiated $Na_{1-x}MF_3$ ($0 \leq x \leq 1$) models were used for DFT calculations. To clarify the structural stability while taking into account the Na contents (x), a supercell containing eight formula units is used. This supercell is twice as large as the *Pnma* primitive cell, as shown in Fig. 4-7. All the possible desodiated structures within the supercell were considered. The lattice parameters and atomic positions were fully optimized, and the models with the lowest-energy Na-configurations were used for the analyses. Note that the calculated energy differences between the structures with FM and AFM ordering were smaller than 0.15 eV per formula unit. Therefore, the effects of the magnetic structures on the theoretical voltages were not significant.
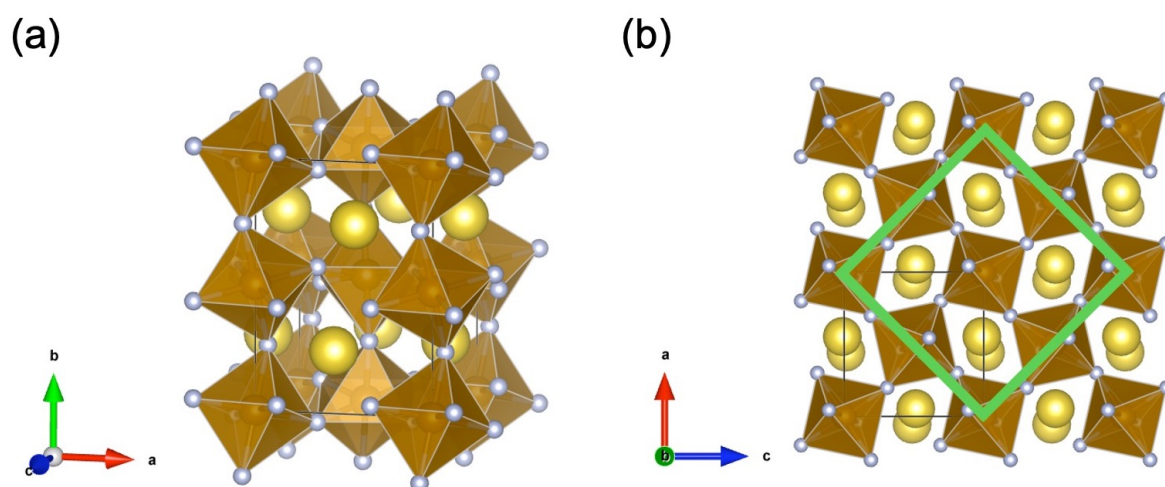

Figure 4-7 Structure of the NaMF3 (M = Fe, Mn, and Co) used for DFT calculations.

The formation energy $E_f(x)$ for $Na_{1-x}MF_3$ was evaluated with respect to the mixed two-phase states consisting of MF_3 and $NaMF_3$. Figure 4-8a shows the calculated formation energies for the $Na_{1-x}MF_3$ (M = Fe, Mn and Co) models with x = 0, 0.25, 0.5, 0.75, and 1, where the models with the lowest formation energies are plotted at each x. As explained in Section 1.4.2., points above the convex hull are thermodynamically unstable, and they are predicted to decompose to stable compositions. The unstable points can be omitted in the calculated voltage profile since they are unlikely to emerge during the charge/discharge reaction.

For $NaFeF_3$, G-type AFM ordering is favorable, regardless of x. $Na_{0.5}FeF_3$ was determined as the most stable intermediate phase in the three cases of $Na_{1-x}FeF_3$ (x = 0.25, 0.5 and 0.75), while $Na_{0.25}FeF_3$ and $Na_{0.75}FeF_3$ are not thermodynamically stable phases. This result suggests that the $NaFeF_3$ cathode has two voltage plateaus, in which the discharge reactions are described as $FeF_3 + Na \rightarrow Na_{0.5}FeF_3 + 0.5Na \rightarrow NaFeF_3$. Figure 4-8b shows theoretical voltage profiles as a function of x for the $Na_{1-x}FeF_3$ cathode with a Na anode. The calculated voltages were 2.95 V vs. Na^+/Na^0 for $0 \leq x \leq 0.5$ and 3.17 V vs. Na^+/Na^0 for $0.5 \leq x \leq 1$; therefore, the calculated average voltage is ca. 3.1 V vs. Na^+/Na^0. This result is in good agreement with the experimental charge/discharge curves shown in Fig. 4-3a.

For $NaMnF_3$, G-type AFM ordering is stable at x = 0, while FM ordering is more stable than AFM at x = 0.25, 0.5, 0.75 and 1. The magnetic ordering in $Na_{1-x}MnF_3$ is complicated and still unclear, because $Na_{1-x}MnF_3$ can contain mixed valence states of not only Mn^{2+} (d^5) but also Mn^{3+} (d^4). Using the Goodenough-Kanamori rules [22], the magnetic ordering of Mn^{3+} in perovskite structures cannot be easily determined. In Fig. 4-8a, $Na_{0.25}MnF_3$ and $Na_{0.5}MnF_3$ were thermodynamically stable as intermediate phases. Notably, the formation energy of $Na_{0.25}MnF_3$ was the lowest among the other composition. This might be due to the complex relationship between the Na ordering and the Jahn-Teller ordering of Mn ions. The results indicated that the $NaMnF_3$ cathode can have three voltage plateaus for the ranges of $0 \leq x \leq$

0.5, $0.5 \leq x \leq 0.75$ and $0.75 \leq x \leq 1$, and the calculated voltages were 3.84 V ($0 \leq x \leq 0.5$), 3.90 V ($0.5 \leq x \leq 0.75$) and 4.55 V ($0.75 \leq x \leq 1$), as shown in Fig. 4-8b. The experimental voltage for $NaMnF_3$ during the charging process was ca. 4.0 V, and the charge capacity was 106 mAh g^{-1}, which corresponds to a 0.5 Na^+ reaction with $NaMnF_3$. The calculated average voltage in the range of $0 \leq x \leq 0.75$ is considered to be in good agreement with the experimental results.

For $NaCoF_3$, G-type AFM ordering is stable, regardless of x. $NaCoF_3$ has two stable intermediate phases of $Na_{0.25}CoF_3$ and $Na_{0.5}CoF_3$ (Fig. 4-8a), and three voltage plateaus of 4.48 V ($0 \leq x \leq 0.5$), 4.57 V ($0.5 \leq x \leq 0.75$) and 4.79 V ($0.75 \leq x \leq 1$), as shown in Fig. 4-8b. However, the experimental voltage of $NaCoF_3$ during the charging process was not clearly observed, because the voltage of the Co^{2+}/Co^{3+} redox in $NaCoF_3$ was higher than the stable potential window of electrolyte.

The calculated x-dependent voltage profiles show stepwise curves with the highest voltages for M = Co and the lowest voltages for M = Fe. Considering the experimental maximum potential window of 4.6 V, it can be speculated from Fig. 4-8b that the experimentally observable x ranges are mainly $x = 0$–1 for Fe, $x = 0$–0.75 for Mn and $x = 0$–0.5 for Co, which are consistent with the experimental capacity differences for the M elements shown in Fig. 4-3.

Since it is possible that the carbon reacted with the active materials during the mechanical ball-milling, the formation energies of the C-substituted $NaMF_3$ were calculated by the DFT. Table 4-2 shows the formation energies with the C atom at Na site, transition metal (TM) site, and F site, respectively. All the structures have positive formation energy. Therefore, it is unlikely that the carbon reacted with the active materials, and the structural models used in this study and their calculated voltages are reasonable.

There is another possibility that the electronic structure and voltages of the active materials are strongly affected by the pore size of the particles. However, porous $LiCoO_2$,

LiFePO$_4$, and Na$_3$V$_2$(PO$_4$)$_3$ have the same voltage as non-porous materials, as previously reported [23-25]. Thus, the pores of the active materials do not strongly affect their lattice energies, suggesting that the DFT calculations with the perfect crystal structure models predicted the properties with high accuracy.
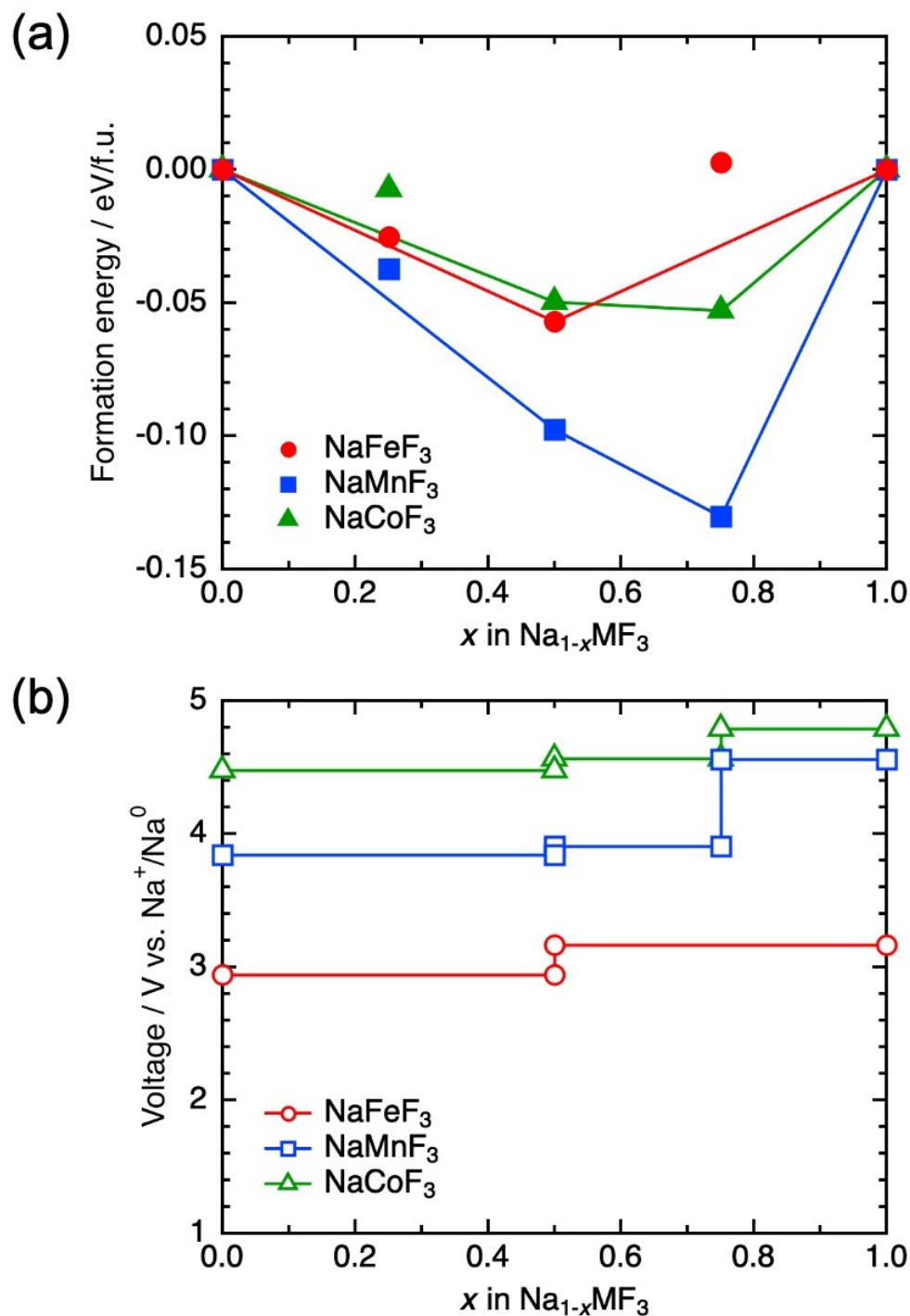
Figure 4-8 (a) Formation energies of $Na_{1-x}MF_3$ (M = Fe, Mn, and Co) calculated for $x = 0$, 0.25, 0.5, 0.75 and 1, with reference to the two-phase mixed states of MF_3 and $NaMF_3$ as references. The lines show convex hulls connecting thermodynamically stable phases.

(b) Calculated voltages as a function of x in $Na_{1-x}MF_3$ (M = Fe, Mn, and Co), assuming that the battery reactions proceed via the thermodynamically stable intermediate phases.

Table 4-2 Formation energies of the C-substituted $NaMF_3$ (M = Fe, Mn, and Co) with the C atom at Na site, TM (transition metal) site, and F site.

	Formation energy / eV f.u.$^{-1}$		
	C at Na site	C at TM site	C at F site
$NaFeF_3$	0.400	0.430	0.486
$NaMnF_3$	0.345	0.308	0.347
$NaCoF_3$	0.575	0.486	0.444

4.4. Conclusion

In this work, $NaMF_3$ (M = Fe, Mn, and Co) were prepared using the dry-ball milling method. $NaFeF_3$ exhibited a large rechargeable capacity of 169 mAh g^{-1} and had a calculated energy density of over 480 Wh kg^{-1}, which is comparable with the reported iron-based cathode materials. This is the first study to report that $NaMnF_3$ has an operating voltage of 3.4 V. In addition, the voltages calculated using the DFT method were in good agreement with the experimental results for $NaFeF_3$ and $NaMnF_3$. Although the experimental voltage for $NaCoF_3$ during the charging process was not confirmed, DFT calculations revealed that the average voltage for $NaCoF_3$ would be 4.6 V. Therefore, $NaCoF_3$ would have potential for application as a high voltage cathode for NIBs, if a novel electrolyte with a wide stability potential window could be developed.

References

[1]   J. Zhao, L. Zhao, N. Dimov, S. Okada, and T. Nishida, *J. Electrochem. Soc.*, **160** (2013) A3077–A3081.

[2]   P. Barpanda, T. Ye, S. Nishimura, S.-C. Chung, Y. Yamada, M. Okubo, H. Zhou, and A. Yamada, *Electrochem. Commun.*, **24** (2012) 116–119.

[3]   Y. Kawabe, N. Yabuuchi, M. Kajiyama, N. Fukuhara, T. Inamasu, R. Okuyama, I. Nakai, and S. Komaba, *Electrochemistry*, **80** (2012) 80–84.

[4]   P. Barpanda, G. Oyama, S. Nishimura, S.-C. Chung, and A. Yamada, *Nat. Commun.*, **5** (2014) 4358.

[5]   M. Nishijima, I. D. Gocheva, S. Okada, T. Doi, J. Yamaki, and T. Nishida, *J. Power Sources*, **190** (2009) 558–562.

[6]   I. D. Gocheva, M. Nishijima, T. Doi, S. Okada, J. Yamaki, and T. Nishida, *J. Power Sources*, **187** (2009) 247–252.

[7]   A. Kitajou, H. Komatsu, K. Chihara, I. D. Gocheva, S. Okada, and J. Yamaki, *J. Power Sources*, **198** (2012) 389–392.

[8]   Y. Yamada, T. Doi, I. Tanaka, S. Okada, and J. Yamaki, *J. Power Sources*, **196** (2011) 4837–4841.

[9]   N. Dimov, A. Nishimura, K. Chihara, A. Kitajou, I. D. Gocheva, and S. Okada, *Electrochim. Acta*, **110** (2013) 214–220.

[10]   J. Nava-Avendaño, M. E. Arroyo-de Dompablo, C. Frontera, J. A. Ayllón, and M. R. Palacín, *Solid State Ionics*, **278** (2015) 106–113.

[11]   P. E. Blöchl, *Phys. Rev. B*, **50** (1994) 17953–17979.

[12]   G. Kresse and D. Joubert, *Phys. Rev. B*, **59** (1999) 1758–1775.

[13]   G. Kresse and J. Furthmüller, *Phys. Rev. B*, **54** (1996) 11169–11186.

[14]   G. Kresse and J. Furthmüller, *Comput. Mater. Sci.*, **6** (1996) 15–50.

[15]   J. P. Perdew, K. Burke, and M. Ernzerhof, *Phys. Rev. Lett.*, **77** (1996) 3865–3868.

[16]   S. L. Dudarev, G. A. Botton, S. Y. Savrasov, C. J. Humphreys, and A. P. Sutton, *Phys. Rev. B*, **57** (1998) 1505–1509.

[17]   H. J. Monkhorst and J. D. Pack, *Phys. Rev. B*, **13** (1976) 5188–5192.

[18]   F. L. Bernal, K. V. Yusenko, J. Sottmann, C. Drathen, J. Guignard, O. M. Løvvik, W. A. Crichton, and S. Margadonna, *lnorg. Chem.*, **53** (2014) 12205–12214.

[19]   S. Yu, P. Zhang, S. Q. Wu, A. Y. Li, Z. Z. Zhu, and Y. Yang, *J. Solid State Electrochem.*, **18** (2014) 2071–2075.

[20]   N. Yabuuchi, M. Kajiyama, J. Iwatate, H. Nishikawa, S. Hitomi, R. Okuyama, R. Usui, Y. Yamada, and S. Komaba, *Nature Materials*, **11** (2012) 512–517.

[21]   S. Miyoshi, T. Akbay, T. Kurihara, T. Fukuda, A. T. Staykov, S. Ida, and T. Ishihara, **120** (2016) 22887–22894.

[22]   J. Kanamori, *J. Phys. Chem. Solids*, **10** (1959) 87–98.

[23]   L. Xue, S. V. Savilov, V. V. Lunin, and H. Xia, *Adv. Funct. Mater.*, **28** (2018) 1705836.

[24]   J. Yang, J. Wang, D. Wang, X. Li, D. Geng, G. Liang, M. Gauthier, R. Li, and X. Sun, *J. Power Sources*, **208** (2012) 340-344.

[25]   M. Guo, W. Zhao, H. Dou, G. Gao, X. Zhao, and X. Yang, *ACS. Appl. Mater. Interfaces*, **11** (2019) 27024-27032.

Chapter 5

Conclusion

The growing demand for secondary batteries raises concerns about future depletion of the natural resources of lithium. NIBs are promising alternatives to conventional LIBs due to the abundance and low cost of sodium resources. However, for the widespread adoption of NIBs, further development of cathode materials is vital. In this thesis, three classes of promising cathode materials were experimentally and computationally investigated.

In Chapter 2, the Ca-substitution effect on P3-type Na_xCoO_2 was studied. Layered oxides generally have poor cycle performance due to the irreversible phase transition accompanied by slab glides. The Ca substitution to the Na site was performed to prevent the irreversible phase transition. The Ca^{2+} ions were incorporated in the Na layers, as evidenced by the Rietveld refinement and SEM-EDX observation. The Ca substitution improved the cycle performance due to the suppressed phase transition.

The DFT calculation predicted that the Ca substitution would have little effect on the thermodynamic phase stabilities. On the other hand, the Ca^{2+} ions in the Na layers were found to kinetically hinder the irreversible phase transition at high voltage. NEB calculations were performed in order to compare the Na^+ diffusivities in the layered oxides. Although the presence of Ca^{2+} ions in the Na layers seemed to impede the Na^+ diffusion, the migration energy of Na^+ ions was decreased by the Ca substitution because the Ca^{2+} ions expanded the bottleneck

125

of the Na layers. This result is consistent with the experimental result that the overpotential of the Ca-substituted Na_xCoO_2 was not higher than that of non-substituted Na_xCoO_2. Therefore, the Ca-substitution for Na ions proved to be a reasonable modification to the family of layered oxides.

In Chapter 3, the reasons for the limitation of the three-Na^+ extraction from $Na_3V_2(PO_4)_3$ were elucidated. While $Li_3V_2(PO_4)_3$ shows the electrochemical three-Li^+ extraction, the electrochemical three-Na^+ extraction from $Na_3V_2(PO_4)_3$ has not been reported yet, to the best of our knowledge. While electrochemical tests were performed to determine whether the extraction of three Na^+ ions occurs, the three-Na^+ extraction was not observed. The DFT calculation suggested that a high voltage of more than 4.5 V vs. Na^+/Na^0 is needed to extract the third Na^+ from the Na1 site. Moreover, the Na^+ extraction from the Na1 site requires high activation energy at the charged state ($NaV_2(PO_4)_3$). The significant activation energy is attributable to the increased electrostatic repulsion between the Na^+ ions and V^{4+} ions at the transition state. Additionally, cell contraction also increases the activation energy. The AIMD simulation revealed that the Na^+ ions are locked up in the Na1 sites at the charged state ($NaV_2(PO_4)_3$), whereas they can diffuse three-dimensionally at the discharged state ($Na_3V_2(PO_4)_3$).

On the other hand, the calculated voltage of the third-Li^+ extraction from $Li_3V_2(PO_4)_3$ was 4.45 V vs. Li^+/Li^0 (ca. 4.2 V vs. Na^+/Na^0). The AIMD simulations suggested that the Li^+ ions diffuse three-dimensionally in the polyanion framework in both $Li_3V_2(PO_4)_3$ and $LiV_2(PO_4)_3$. These results demonstrate that the third Li^+ ions can be extracted without significant electrolyte decomposition and large activation energy. This study has proven that the third-Na^+ extraction is challenging. However, the use of ionic liquids or solid electrolytes with a low current rate might enable the third-Na^+ extraction. In addition, partial substitution may be a practical approach.

In Chapter 4, the electrochemical properties of $NaMF_3$ (M = Fe, Mn, and Co) were studied. $NaFeF_3$ showed a capacity of 169 mAh g^{-1}, and the energy density was 480 Wh kg^{-1}. Among the iron-based cathode materials, this energy density was relatively high. $NaMnF_3$ exhibited a discharge slope at around 3.6 V, which was not observed in a previous report. The improved electrochemical properties were primarily due to the particle pulverization and the well-dispersed conductive carbon induced by the two-step carbon mixing. The $NaCoF_3$ was electrochemically inactive.

The DFT calculations were performed to investigate the voltage and phase stabilities during the charge/discharge process. The calculated voltages of $NaFeF_3$ and $NaMnF_3$ were in good agreement with the experimental results. The voltage of $NaCoF_3$ was predicted to be 4.6 V. Therefore, $NaCoF_3$ cannot be used with the conventional organic electrolytes. This material might exhibit excellent electrochemical performance if a novel electrolyte with a wide potential window could be developed.

This thesis provides new insights into charge/discharge mechanisms and material design strategies for the layered oxides, NASICON-type compounds, and perovskite-type fluorides. These strategies span a wide range of approaches, from elemental substitutions to synthesis procedures and we have identified opportunities for future optimization. For instance, the cycle performance of $Na_xCa_yCoO_2$ can be further improved by optimizing the Ca-doping amount. The combination of Ca substitution for the Na site and another elemental substitution for the transition metal site might also be effective. The use of an ionic liquid or a solid electrolyte with a wide potential window may enable three-Na^+ extraction from $Na_3V_2(PO_4)_3$. For perovskite-type fluorides, nanoparticle synthesis, combined with carbon coating, would result in significantly improved electrochemical properties, such as small overpotential and excellent cycle performance. In LIBs, several types of cathode materials, such as $LiCoO_2$, $LiMn_2O_4$, and $LiFePO_4$, are used depending on the applications, and it is desirable to have

similar options for NIBs. All three materials studied in this thesis have the potential to be utilized as cathodes, but further developments of the active materials are required to facilitate their practical application.; therefore, the findings of this study can provide useful guidance.

This work also demonstrates that the complementary combination of experiments and computations is indispensable for research on energy storage materials. Computational methods provide useful information about thermodynamic stabilities and atomic-level phenomena, which are often difficult to measure experimentally. For example, the DFT calculations enabled the assessment of the thermodynamic phase stabilities of Na_xCoO_2 and Na_xMF_3. The NEB calculations also enabled us to relate the Na-ion diffusivities to the local environments around the hopping ions in $Na_xCa_yCoO_2$ and $Na_xV_2(PO_4)_3$. Moreover, computational methods can also be used for the screening of promising battery materials. Recently, $Na_2V_2O_7$ and $Na_4MnCr(PO_4)_3$, which are cathode materials for NIBs, were discovered by high-throughput DFT calculation; these cathode active materials exhibited excellent properties, as elucidated from electrochemical tests [1, 2]. In addition, the utilization of machine learning in materials science, called "materials informatics", has attracted interest because of its potential to significantly reduce the material development period [3, 4]. Future, research on battery materials will be further accelerated with the aid of these computational methods.

References

[1]   N. Tanibata, Y. Kondo, S. Yamada, M. Maeda, H. Takeda, M. Nakayama, T. Asaka, A. Kitajou, and S. Okada, *Sci. Rep.*, **8** (2018) 17199.

[2]   J. Wang, Y. Wang, D. H. Seo, T. Shi, S. Chen, Y. Tian, H. Kim, and G. Ceder, *Adv. Energy Mater.*, **10** (2020) 1903968.

[3]   R. Jalem, K. Kanamori, I. Takeuchi, M. Nakayama, H. Yamasaki, and T. Saito, *Sci. Rep.*, **8** (2018) 5845.

[4]   V. Tshitoyan, J. Dagdelen, L. Weston, A. Dunn, Z. Rong, O. Kononova, K. A. Persson, G. Ceder, and A. Jain, *Nature*, **571** (2019) 95–98.

Acknowledgment

I thank my parents, my brother, and my sister, without whom I could not have gotten to where I am today.

Most of all, I express my deepest gratitude to my wife for her understanding, patience, and support; I could not have completed my Ph.D. program without her presence in my life.

Yuji Ishado

August 2020